Towards Efficient Cooling Strategies for Gears in High-Speed High-Load Applications

Experimental Study and Model Development for Heat Transfer in Jet Impingement Cooling

Zur Erlangung des akademischen Grades eines

Doktors der Ingenieurwissenschaften (Dr.-Ing.)

von der KIT-Fakultät für Maschinenbau des
Karlsruher Instituts für Technologie (KIT)

angenommene

Dissertation

von

Emre Ayan, M. Sc.
aus Istanbul

Tag der mündlichen Prüfung: 10.03.2025
Hauptreferent: Prof. Dr.-Ing. Hans-Jörg Bauer
Korreferent: Prof. Dr.-Ing. Matthias Stripf

Towards Efficient Cooling Strategies for Gears in High-Speed High-Load Applications

Experimental Study and Model Development for Heat Transfer in Jet Impingement Cooling

by

Emre Ayan

Berlin 2025

Vorwort des Herausgebers

Der schnelle technische Fortschritt im Turbomaschinenbau, der durch extreme technische Forderungen und starken internationalen Wettbewerb geprägt ist, verlangt einen effizienten Austausch und die Diskussion von Fachwissen und Erfahrung zwischen Universitäten und industriellen Partnern. Mit der vorliegenden Reihe haben wir versucht, ein Forum zu schaffen, das neben unseren Publikationen in Fachzeitschriften die aktuellen Forschungsergebnisse des Instituts für Thermische Strömungsmaschinen des Karlsruher Instituts für Technologie (KIT) einem möglichst großen Kreis von Fachkollegen aus der Wissenschaft und vor allem auch der Praxis zugänglich macht und den Wissenstransfer intensiviert und beschleunigt.

Flugtriebwerke, stationäre Gasturbinen, Turbolader und Verdichter sind im Verbund mit den zugehörigen Anlagen faszinierende Anwendungsbereiche. Es ist nur natürlich, dass die methodischen Lösungsansätze, die neuen Meßtechniken, die Laboranlagen auch zur Lösung von Problemstellungen in anderen Gebieten - hier denke ich an Otto- und Dieselmotoren, elektrische Antriebe und zahlreiche weitere Anwendungen - genutzt werden. Die effiziente, umweltfreundliche und zuverlässige Umsetzung von Energie führt zu Fragen der ein- und mehrphasigen Strömung, der Verbrennung und der Schadstoffbildung, des Wärmeübergangs sowie des Verhaltens metallischer und keramischer Materialien und Verbundwerkstoffe. Sie stehen im Mittelpunkt ausgedehnter theoretischer und experimenteller Arbeiten, die im Rahmen nationaler und internationaler Forschungsprogramme in Kooperation mit Partnern aus Industrie, Universitäten und anderen Forschungseinrichtungen durchgeführt werden.

Es sollte nicht unerwähnt bleiben, dass alle Arbeiten durch enge Kooperation innerhalb des Instituts geprägt sind. Nicht ohne Grund ist der Beitrag der Werkstätten, der Technik-, der Rechner- und Verwaltungsabteilungen besonders hervorzuheben. Diplomanden und Hilfsassistenten tragen mit ihren Ideen Wesentliches bei, und natürlich ist es der stets freundschaftlich fordernde wissenschaftliche Austausch zwischen den Forschergruppen des Instituts, der zur gleichbleibend hohen Qualität der Arbeiten entscheidend beiträgt. Dabei sind wir für die Unterstützung unserer Förderer außerordentlich dankbar.

Die in jüngster Zeit in ersten Turbofantriebwerken vollzogene Änderung der Triebwerksarchitektur, die Integration eines Planetengetriebes zwischen dem Gebläse (Fan) des Triebwerks und der Niederdruckwelle, führt zu einer drastischen Reduktion des Brennstoffverbrauchs in der Größenordnung von 10 - 15% im Vergleich zur vorigen Triebwerksgeneration. Eine wesentliche Herausforderung bei der Auslegung des Untersetzungsgetriebes von Triebwerken für Großraum-Langstreckenflugzeuge besteht in der Beherrschung seines Thermalhaushalts. Aufgrund der immensen übertragenen Leistung führen selbst geringe relative mechanische Verluste des Getriebes zur Dissipation einer Leistung von mehreren hundert Kilowatt. Die dissipierte Leistung ist durch eine effektive und effiziente Kühlung der Zahnräder aus dem Getriebe abzuleiten. Dabei steht die Kühlung, die durch Besprühen der Zahnflanken mit Ölstrahlen erfolgt, vor der Herausforderung, eine ausreichende Temperaturabsenkung der Zahnräder sicherzustellen und gleichzeitig aber die eingesetzte Ölmenge zu begrenzen, um keine zusätzlichen Planschverluste zu generieren. Um dieses Ziel erreichen zu können, ist die genaue Kenntnis des Wärmeübergangs zwischen Ölstrahl und Zahnflanke unbedingte Voraussetzung.

Aufbauend auf einer früheren Arbeit am Institut für Thermische Strömungsmaschinen des KIT befasst sich der Autor im vorliegenden Band der Schriftenreihe mit der experimentellen Untersuchung des Wärmeübergangs zwischen Ölstrahlen und den Flanken eines repräsentativen generischen Zahnrads. Mit Hilfe numerischen Analysen wurden betriebspunktabhängige Strukturen des Ölstrahls auf den Einfluss von Kavitation im Düseninnern bis hin zur Superkavitation zurückgeführt. Die Ergebnisse der ortsaufgelösten Messungen des Wärmeübergangs ermöglichen, die Wirkzusammenhänge zwischen den Randbedingungen Ölvolumenstrom, Drehzahl, Düsenwinkel, Strahleindringtiefe und Aufprallwinkel und dem mittleren Wärmeübergang zu identifizieren und physikalisch verständlich zu erklären. Mit Hilfe der experimentellen Daten konnte eine auf Basis numerischer Strömungsberechnungen aufgestellte Hypothese bestätigen werden, dass die durch den Ölfilm benetzte Oberfläche der entscheidende Parameter für den Wärmeübergang auf den Zahnflanken darstellt. Die hohe Qualität der aus den Messungen abgeleiteten Korrelation für den mittleren Wärmeübergang ermöglicht nun eine erheblich sicherere wärmetechnische Auslegung von Hochleistungsgetrieben für zukünftige Flugtriebwerke mit gesteigerten Nebenstromverhältnissen und höchsten Vortriebswirkungsgraden. Die Korrelation ist grundsätzlich auch auf andere als die untersuchte Geometrie geradverzahnter Stirnräder anwendbar.

Karlsruhe, April 2025 Prof. Dr.-Ing. Hans-Jörg Bauer

Acknowledgements

Parts of the results presented in this work originated from the OLIAS and VOLAT projects, which were funded through the research program Luftfahrtforschungsprogramm (LuFo) of the Bundesministerium für Wirtschaft und Klimaschutz (BMWK) and carried out in close collaboration with the industrial partner Rolls-Royce Deutschland Ltd & Co KG.

Kurzfassung

Hochlast- und Hochgeschwindigkeitsgetriebe sind ein wesentlicher Bestandteil der modernen Triebwerke. Ein kritischer, aber noch nicht ausreichend erforschter Aspekt ist die Kühlung von Zahnrädern, bei der die derzeitigen Konstruktionen aufgrund begrenzter Daten zur Wärmeübertragung stark auf die Erfahrung von Experten und iterative Verbesserungen angewiesen sind. Die vorliegende Arbeit schließt diese Lücke, indem sie die wichtigsten Parameter, die die Wärmeübertragung beeinflussen, experimentell charakterisiert und ihren Einfluss quantifiziert.

Der bestehende Versuchsaufbau und die Methodik werden verbessert und validiert. Ein neuartiges Kalibrierungsverfahren wird eingeführt, um die Genauigkeit der Temperaturmessungen erheblich zu erhöhen. Die Düsenströmung wird experimentell und numerisch untersucht, wodurch die Ursache für die beobachtete Strömungsablösung in dem sogenannten „hydraulic flip“ gefunden wird. Thermische Messungen über eine Reihe von Betriebsparametern wie Ölvolumenstrom, Zahnraddrehzahl, Strahlwinkel, Düsenanzahl und -durchmesser werden zur Charakterisierung der so genannten signifikanten Parameter verwendet. Der Einfluss dieser signifikanten Parameter auf den flächengemittelten Wärmeübergangskoeffizienten sowie dessen räumliche Verteilung auf der Zahnradoberfläche wird anhand einer optimierten Testmatrix untersucht. Basierend auf den Ergebnissen wird ein neuartiges empirisches Wärmeübergangsmodell entwickelt. Die Vorhersagen des Modells werden mit numerisch bestimmten benetzten Zahnradflächen aus der Literatur verglichen. Verschiedene Optimierungsszenarien werden diskutiert, um die Fähigkeiten des Modells zu demonstrieren. Die Ergebnisse stellen einen wichtigen Beitrag zum Stand der Forschung für die Charakterisierung von Getriebekühlsystemen in Hochlast- und Hochgeschwindigkeitsanwendungen dar und zeigen das Potenzial für eine verbesserte Kühlleistung durch gezielte konstruktive Anpassungen auf.

Abstract

High-speed high-load gearboxes are an essential component of modern jet engines. A critical yet under-researched aspect is the cooling of gears, where current designs rely heavily on expert experience and iterative improvements due to limited heat transfer data. This study addresses this gap by experimentally characterising the key parameters that influence heat transfer and quantifying their impact.

The existing test setup and methodology are improved and validated. A novel calibration method is introduced to significantly increase the accuracy of temperature measurements. The nozzle flow is investigated experimentally and numerically, identifying the cause of the observed flow separation in the so-called hydraulic flip. Thermal measurements across a range of operating parameters, such as oil volume flow rate, gear rotational speed, jet angle, nozzle number and nozzle diameter, are used to characterise the so-called significant parameters. The influence of these significant parameters on the surface-averaged heat transfer coefficient and its spatial distribution on the gear surface is investigated using an optimised test matrix. Based on the results, a novel empirical heat transfer model is developed. The predictions of the model are compared with numerically determined wetted areas from the literature. Various optimisation scenarios are discussed to demonstrate the capabilities of the model. The results make a significant contribution to the state of research on gearbox cooling system characterisation in high-speed high-load applications, highlighting the potential for improved cooling performance through targeted design modifications.

Contents

Symbols

Symbol	Unit	Description
Latin symbols		
a		Gain of the telemetry calibration curve
$A_{\mathrm{F,max}}$	m^2	Maximum wetted area
A_{Fl}	m^2	Quarter of a tooth flank area
$A^*_{\mathrm{F,max}}$		Normalised maximum wetted area
b		Offset of the telemetry calibration curve
$C_{1,2,3,\mathrm{m,o,Re,V},\sigma,\nu}$		Model parameters
C_{c}		Contraction coefficient
C_{d}		Discharge coefficient
d_{ij}	m	Distance between thermocouples i and j
d_{jet}	m	Jet diameter
d_{n}	m	Nozzle diameter
d^*		Normalised jet diameter
D_{out}		Digital output of the telemetry unit
E	m	Nozzle outlet eccentricity
h	$\mathrm{W/(m^2K)}$	Heat transfer coefficient
$\overline{h}$	$\mathrm{W/(m^2K)}$	Surface-averaged heat transfer coefficient
$\mathbf{h}$	$\mathrm{W/(m^2K)}$	Vector of heat transfer coefficients at thermocouple positions
$\overline{\mathbf{h}}$	$\mathrm{W/(m^2K)}$	Mean of $\mathbf{h}$
h^*		Normalised and volume flow rate scaled heat transfer coefficient (initial test matrix)
h^+		Normalised and volume flow rate scaled heat transfer coefficient (optimal test matrix)
h_{local}		Local heat transfer coefficient
$\mathbf{J}$	$\mathrm{m^2K^2/W}$	Jacobian matrix
l_{i}	m	Distance between thermocouple i and the inner surface
l_{im}	m	Impingement length
l_{max}	m	Maximum possible impingement length
l_{n}	m	Nozzle length
l^*		Normalised impingement length
L	m	Circumferential length per tooth
m	m	Tooth module
n_{n}	m	Nozzle number

N	RPM	Rotational speed in rounds per minute
p	Pa	Pressure
$\dot{q}$	$\mathrm{W/m^2}$	Area specific heat flux
r_b	m	Base radius
r_im	m	Impingement radius
r_p	m	Pitch radius
r_r	m	Root (bottomland) radius
r_spraybar	m	Spraybar axis offset
r_t	m	Tip (topland) radius
R^2		Coefficient of determination
r	m	Radius
s	m	Circumferential coordinate
s^+		Dimensionless circumferential coordinate
S	$\mathrm{K^2}$	Square error of temperature prediction
t	s	Time
$\mathbf{T}$	°C, K	Vector of temperature values at thermocouple locations
$\overline{\mathbf{T}}$	°C, K	Mean of $\mathbf{T}$
T_in	°C, K	Inner temperature
T_oil	°C, K	Oil temperature
T_tooth	°C, K	Tooth surface temperature
u_gear	m/s	Circumferential gear speed at pitch radius
u_jet	m/s	Jet velocity
$u_\mathrm{jet,r}$	m/s	Radial jet speed
$u_\mathrm{jet,t}$	m/s	Tangential jet speed
u_rel	m/s	Relative jet velocity
u_tip	m/s	Radial jet tip velocity
U	V	Thermocouple voltage
$\dot{V}_\mathrm{nozzle}$	$\mathrm{m^3/s}$	Oil volume flow rate per nozzle
$\dot{V}_\mathrm{oil}$	$\mathrm{m^3/s}$	Total oil volume flow rate
W	m	Gear width
$x_\mathrm{c}, y_\mathrm{c}$	m	Cartesian coordinates
x	m	Profile shift
y	m	Axial coordinate
y^+		Dimensionless axial coordinate
Z		Number of teeth

Greek symbols

α_{eff}	°	Effective jet inclination angle
α_{n}	°	Nozzle inclination angle
β	°	Impingement angle
γ	°	Pressure angle
γ_{p}	°	Pressure angle at pitch radius
ζ	rad	Angular position of the jet tip
κ		Variable of log-normal distribution
λ	W/(mK)	Thermal conductivity
μ		Damping factor
ν	m^2/s	Dynamic viscosity
σ		Cavitation number
$\sigma_{\log}$, $\nu_{\log}$		Parameters of log-normal distribution
σ_{res}		Standard deviation of residuals
Σ_{rel}		Relative velocity ratio
τ	rad	Tangential angle
Ψ		Normalised volume flow rate
ω	rad/s	Angular velocity
ω_{tip}	rad/s	Angular jet tip velocity
$\mathbf{\Omega}$	$\mathrm{m}^4\mathrm{K}^4/\mathrm{W}^2$	Diagonal matrix

Similarity parameters

Nu	Nusselt number
$\overline{\mathrm{Nu}}^*$	Surface-averaged normalised Nusselt number
Re	Reynolds number
$\mathrm{Re}_{\mathrm{nozzle}}$	Nozzle Reynolds number
Re_{ω}	Gear Reynolds number

Indices

cal	Calculated
crit	Critical
exit	Exit
exp	Experimental
i, j	Thermocouples *i* and *j*
ideal	Ideal
im	Impingement

jet	Jet
max	Maximum
mes	Measured
min	Minimum
(n)	Belonging to iteration n
n, nozzle	Nozzle
org	Original
prd	Predicted
real	Real
ref	Reference
rej	Rejected iteration
req	Required
sim	Simulated
up	Upstream
v	Vapour

Abbreviations

AF	Active flank
BL	Bottomland
CFD	Computational fluid dynamics
CJ	Cold junction
FEA	Finite element analysis
FP	Flight operating point
HTC	Heat transfer coefficient
LMM	Levenberg-Marquardt Method
OP	Operating point
PF	Passive flank
SB	Spraybar
SPH	Smoothed Particle Hydrodynamics
TC	Thermocouple
TIA	Temperature interpolation approach
TL	Topland
VOF	Volume-of-fluid
VPM	Von Plehwe Method

Figures

Tables

1 Introduction

Improving the efficiency of machines and processes has always been one of the main objectives of engineering endeavours. The primary motivation behind this aim has long been economic. However, the undeniable impact of human-made climate change on the environment has led to increasing awareness, resulting in new moral and political imperatives for pursuing higher efficiency.

Aviation, often labelled as an environmentally unfriendly means of transportation, has also been deeply impacted by this relatively recent narrative change. Despite ambitious goals to transform aviation into a carbon net-zero industry by 2050 (IATA, 2021), a complete transition to entirely electric or hydrogen-powered aviation within the planned period is not possible (Air Transport Action Group, 2021). Even if the battery technology matures to rival the energy density of jet fuel or challenges related to hydrogen production and storage are resolved, the share of these new technologies in carbon emission reduction is projected to be 22% in 2050 (Air Transport Action Group, 2021). Thermal turbomachinery powered by sustainable aviation fuels (SAF) will be necessary until a complete transition becomes technologically and economically viable. Air Transport Action Group (2021) does not consider the possibility of electric or hydrogen aviation for long-haul flights and sees hydrogen only as a potential addition to SAF for medium-haul flights. These categories account for around 73% of today's carbon emissions in the aviation sector. With the projected threefold increase in revenue passenger kilometres between 2019 and 2050 (Air Transport Action Group, 2021), the amount of required SAF will be immense. The Royal Society (2023) discusses the scalability of SAF production in the example of the United Kingdom. It claims that producing SAF from biofuels would require at least half of the agricultural land. If the so-called synthetic electro-fuels are considered, the energy required to replace 2019's jet fuel consumption would be at least 1.5 times the total annual electricity generation of the United Kingdom. Technological advancements are needed to drastically reduce the fuel consumption of traditional jet engines to make these figures economically and technologically feasible.

The total efficiency of a jet engine can be increased by optimising the thermodynamic cycle or improving the propulsive efficiency. The former can be achieved by increasing the pressure ratio or the turbine inlet temperature, e.g. by utilising novel cooling solutions for turbine components. Extensive research in this field has provided continuous, albeit relatively slow, evolutionary improvements over the years. Propulsive efficiency has more potential for dramatic improvement due to conceptual changes in the jet engine architecture. One established architectural improvement is the installation of a gearbox between the fan and the turbomachinery components on the low-pressure shaft, i.e., the low-pressure turbine and, for two shaft engines, the low-pressure compressor. This configuration allows each component to operate within its optimal rotational speed range. These so-called geared turbofans enable the fan to rotate at lower rotational speeds. By doing so, the diameter of the fan blades can be increased without incurring excessive losses. Thanks to the larger fan diameter, the geared turbofans mark significantly higher bypass ratios and, therefore, improved propulsive efficiencies compared to conventional turbofans. Furthermore, the low-pressure turbine can operate at a higher rotational speed, leading to increased stage work. The reduced number of required turbine stages could compensate for the additional

weight of the gearbox and the necessary lubrication and cooling components. For instance, Pratt & Whitney (2021) claims that their PW1100G-JM engine, developed for the Airbus A320neo family and in operation since 2016, reduces fuel consumption by 16% compared to conventional turbofans.

One major challenge in integrating a gearbox into a jet engine is ensuring its efficiency and reliability. Rolls Royce (2022) plans to transmit more than 50 MW over the gearbox in their UltraFan engine. Assuming a very high transmission efficiency of 99%, 500 kW of power would still be dissipated as heat. This heat load on the gearbox is equivalent to burning approximately one litre of jet fuel per minute. Adequate cooling solutions are essential for the reliable and efficient operation of the gearbox and, consequently, the jet engine. Although the gearbox is projected to become a vital component of the next-generation jet engines, whether geared turbofan or open rotor, the utilised oil jet impingement cooling is not thoroughly understood after nearly 60 years of research. The remarks of Radzimovsky from 1966, discussing the paper of McCain and Alsandor (1966), still remain relevant:

> "What should be the best average jet velocity and the optimal flow rate for best results? How many jets should be used and what should be their orientation? What is the relation between these various factors and the speed of the drive that will yield the best results? [...] Most of these questions remain unanswered at the present time and the entire problem still requires extensive investigation."

This work aims to develop an empirical heat transfer model to characterise the cooling of spur gears via oil jet impingement and to answer the questions raised nearly 60 years ago. First, the current state of the art in cooling high-speed gears will be presented. Then, the experimental methodology used to acquire the heat transfer data will be described. Next, the oil jet flow will be investigated experimentally and numerically. Finally, the empirical heat transfer model will be developed, discussed, and evaluated. It will be demonstrated that the model provides an adequate tool to address the questions mentioned above for a wide range of operating parameters.

2 Literature Review and Research Objective

Historically, cooling has been regarded as an additional function of the gear lubrication system (Beuerlein, 1954). However, in high-load, high-speed gearboxes, such as those required in geared turbofans, cooling becomes the primary function of the lubricant (Niemann and Winter, 2003). Cooling has been recognised as a problem without a clear solution (Radzevich, 2012). It has been documented that dip lubrication cannot fulfil the cooling function for high-speed gears, and oil jet injection lubrication, hereafter also called impingement lubrication, should be utilised. Beuerlein (1954) defined the upper limit of dip lubrication for gears with a low surface roughness ($R_Z = 5\ \mu$m) via

$$\omega^2 r_p = 600\ \frac{m}{s^2} \tag{2.1}$$

with the angular velocity ω and the pitch radius r_p. For the gear utilised in this work (r_p = 130 mm), the limiting angular and circumferential velocities would be 67.94 rad/s and 8.83 m/s, respectively. Niemann and Winter (2003) marked 25 m/s as the usual limit for dip lubrication, noting that impingement lubrication is necessary for large gearboxes transmitting over 400 kW. These limiting velocities are substantially exceeded in geared turbofans.

Several oil jet impingement lubrication and cooling methods are proposed in the literature. Schober (1983) presented four methods of impingement with

A: oil jet directed tangentially at the pitch circle,

B: oil jet directed at one of the gears,

C: oil jet in axial direction,

D: oil jet radially ejected through holes into the tooth gaps,

as depicted in Figure 2.1. Method C does not contribute to the lubrication of the gears and restricts cooling only to the axial surfaces impinged by the oil jets, which is particularly problematic for gears with relatively high width-to-diameter ratios. Method D requires a hollowing out of the gears and drilling of oil passages to enable the axially impinging oil to reach the gear teeth. Both modifications introduce stress concentrations close to the gear teeth and significantly reduce the mechanical loading capacity of the gear. Therefore, Methods A and B are the most commonly utilised methods in gearbox applications. Method A can be subdivided into two possible methods: into-mesh (A1 in Figure 2.1) and out-of-mesh impingement (A2 in Figure 2.1), with oil jets impinging on the engaging and disengaging sides of meshing, respectively. In Method B, the oil jet can either be directed radially or with an inclination onto one of the gears. From now on, this method will be referred to as targeted impingement. The position of the impingement can, analogously, be on both the engaging and disengaging sides of meshing.

To the author's knowledge, McCain and Alsandor (1966) wrote the first work focused on the interaction of oil jets with gears, laying the foundation for research that focuses on the cooling aspect of impinging oil. The configurations that they analytically investigated included out-of-mesh and targeted impingement. They defined the impingement depth as the maximum depth at which the impingement started on the gear flank and derived formulations using trigonometric relationships. Figure 2.2 shows the terms used in their derivation. The impingement depth, L, was defined as the difference between the topland radius and the radius of the first point of

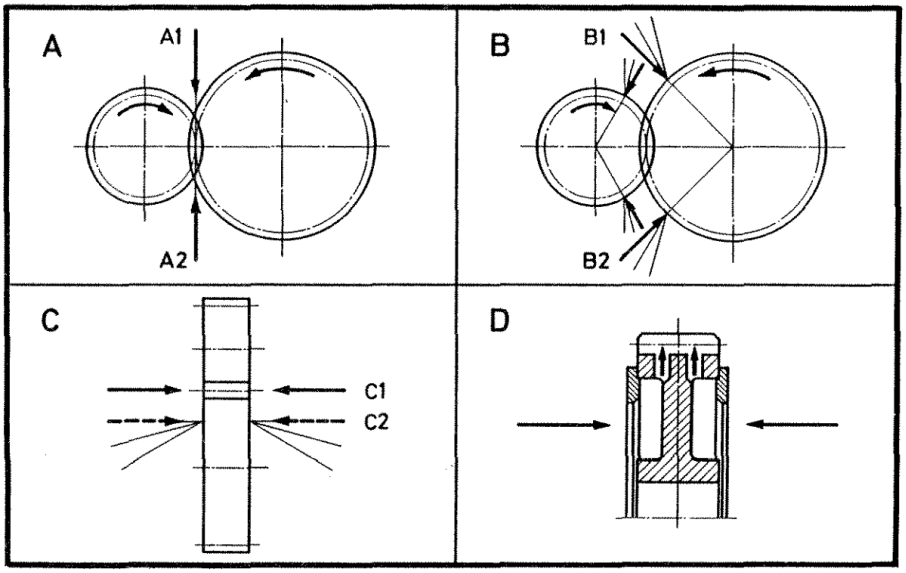

Figure 2.1: Jet impingement cooling methods as presented by Schober (1983).

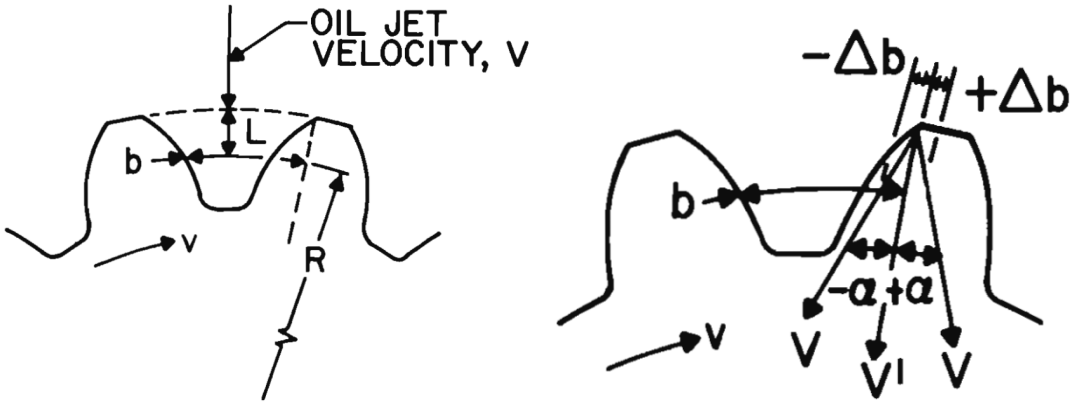

(a) (b)

Figure 2.2: The definition of impingement depth L for radially targeted impingement in (a) and how b is affected by jet inclination (b) (McCain and Alsandor, 1966).

impingement, R. b was the length of an arc with radius R spanning between the first point of impingement and a radial line through the leading tooth tip. An additional term, $\Delta b = L \tan\alpha$, was utilised to account for the effect of jet inclination, α, which changed the amount of rotation required for the jet to impinge on the gear. The impingement depth was given by

$$L = (b + \Delta b)\frac{V\cos\alpha}{v} = \frac{bV\cos\alpha}{v + V\sin\alpha} \tag{2.2}$$

using the jet velocity V, and the circumferential velocity of gear v, at R.

McCain and Alsandor (1966) defined the positive angle of jet inclination so that the circumferential component of the jet velocity is directed in the same direction as the circumferential velocity of the gear. Using Equation 2.2, the authors claimed that the deepest impingement was

achieved with radial impingement when $\alpha = 0°$. Limiting angles of jet inclination were defined to distinguish between inclinations that end up in lubrication or cooling of only certain areas of the gear tooth. Penetration was mentioned interchangeably with the impingement depth, not to be confused with the penetration depth, which accounts for the spreading of the oil film after the initial impingement as defined in later studies.

NASA Lewis Research Center revisited the topic in the 1970s and 1980s. Akin et al. (1975) presented a new vectorial model to determine the impingement depth of a radial jet with or without the effect of gear windage. They investigated the oil jet gear kinematics in two different frames of reference. The first one incorporated a rotating gear and a stationary nozzle, as was the case in their experimental setup (Figure 2.3a). The oil jet was depicted as a string of droplets. The droplets moved in the negative radial direction after exiting the nozzle. After reaching the gear windage boundary layer, the airflow diverted the droplets. The point at which a droplet impinged on the gear flank was denoted with x_w at depth H_w and angle β. Alternatively, the kinematics was also presented in a frame of reference with a stationary gear and moving nozzle. The trajectory of a droplet that goes past the tooth tip (point a) at $t = 0$ is depicted in Figure 2.3b. The windage effect led to the trajectory curvature for $t > 0$. It should be noted that the gear was modelled as a linear rack geometry.

Figure 2.4 shows the vectorial impingement depth model depicted in the second frame of reference. The windage effects were not considered in this model. Therefore, a droplet at the tooth tip at $t = 0$ would approach the next tooth flank at an angle of θ with the relative velocity $v = \sqrt{(v_\mathrm{j}^2 + v_\mathrm{g}^2)}$, where v_j is the jet velocity and v_g is the circumferential velocity of the gear. This droplet would impinge on the flank at the so-called vectorial depth H_v. The region between the first point of impingement and the next tooth tip was projected onto the horizontal coordinate and was denoted with

$$\overline{A} = H_\mathrm{v} \tan \Phi, \tag{2.3}$$

where Φ is the pressure angle. The horizontal width between the first point of impingement and the leading tooth tip was denoted with

$$\overline{B} = H_\mathrm{v} \cot \theta. \tag{2.4}$$

Furthermore, the summation of $\overline{A}$ and $\overline{B}$ should be equal to the horizontal space between two tooth tips, calculated with

$$\overline{A} + \overline{B} = \frac{1}{P_\mathrm{d}} \left(\frac{\pi}{2} + 2 \tan \Phi + \frac{B}{2} \right) = H_\mathrm{v} \left(\tan \Phi + \frac{v_\mathrm{g}}{v_\mathrm{j}} \right), \tag{2.5}$$

which gives

$$H_\mathrm{v} = \frac{\frac{\pi}{2} + 2 \tan \Phi + \frac{B}{2}}{P_\mathrm{d} \left(\tan \Phi + \frac{v_\mathrm{g}}{v_\mathrm{j}} \right)}, \tag{2.6}$$

with the diametral pitch P_d and the backlash of the gear set B. One limitation of this model was the assumption of a radially directed jet. Keller (2022) modified the equation for a jet inclined

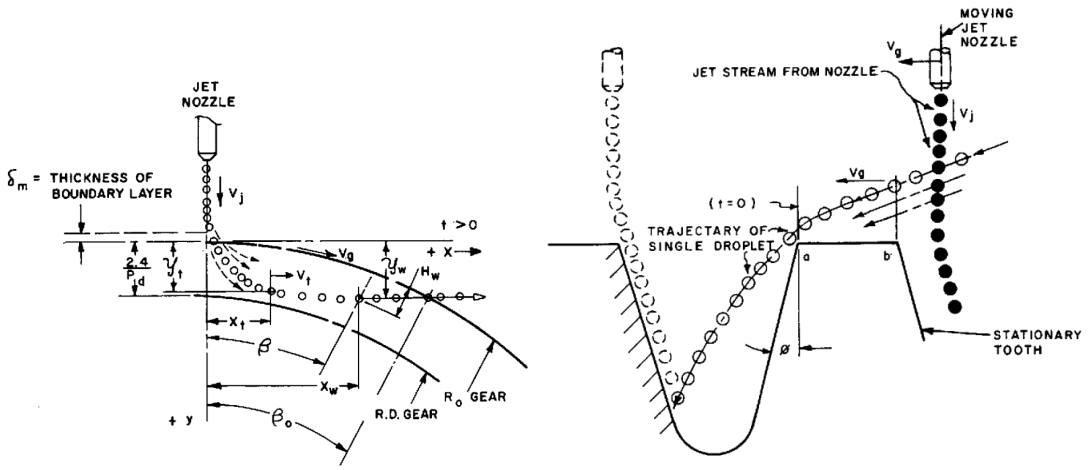

(a) (b)

Figure 2.3: Vectorial model of Akin et al. (1975) in the frame of reference with stationary nozzle (a) and with stationary gear (b).

by α relative to the radial orientation:

$$H_{\mathrm{v}} = \frac{\frac{\pi}{2} + 2\tan\Phi + \frac{B}{2}}{P_{\mathrm{d}}\left(\tan\Phi + \frac{v_{\mathrm{g}} - v_{\mathrm{j}}\sin\alpha}{v_{\mathrm{j}}\cos\alpha}\right)}. \tag{2.7}$$

Akin et al. (1975) presented a formulation to account for the windage effect. The forces acting upon the droplet were considered to calculate the flight time of a droplet from the leading tooth tip to the impingement point. Subsequently, the coordinates of the impingement point and the so-called windage depth H_{W} were calculated. Comparisons of H_{W} and H_{v} have shown that the windage effect can be neglected for droplets with a diameter larger than 0.076 mm.

Akin et al. (1975) also conducted experiments with high-speed photography to capture the interaction of the oil jet with the gear. The vectorial model was in good agreement with the experimentally determined impingement depths at high oil pressures. The authors stated the viscous losses in the nozzle as the reason for high deviations at low pressures. A significant portion of the oil initially penetrating below the impingement depth was observed to leave the tooth space without further contacting the tooth. In a related publication, Akin and Mross (1975) proposed that an impingement depth not greater than three-quarters of the overall tooth depth should be sufficient for effective cooling because of the additional penetration.

The same research group published follow-up works on different jet impingement configurations. Townsend and Akin (1978) derived formulations for impingement depths in an out-of-mesh configuration for both the driving and driven gears. They stated that the resulting oil spray after the impingement is usually adequate for lubrication but not for cooling. Akin and Townsend (1983a,b) investigated the impingement depths in into-mesh configurations with jet velocities less than, equal to and greater than circumferential velocities of gear at pitch radius. The authors concluded that optimal cooling is provided if the jet velocity is equal to the circumferential

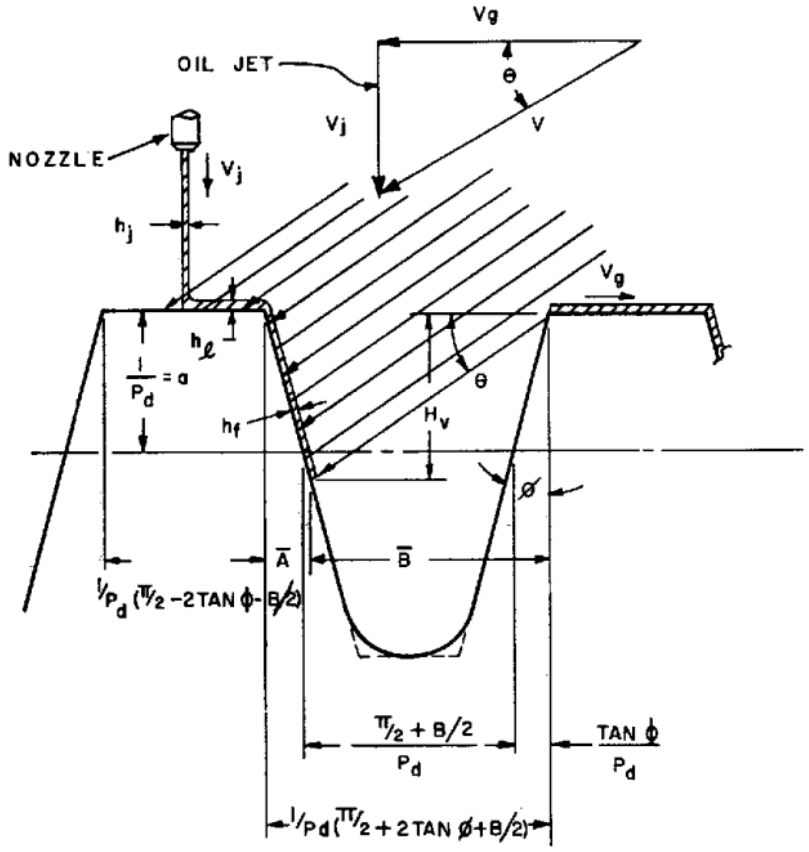

Figure 2.4: Vectorial impingement depth model of Akin et al. (1975) in the frame of reference with stationary gear.

velocity, and favouring either driving or driven gear is possible by slightly reducing or increasing the jet velocity. Akin and Townsend (1985) improved the formulations for out-of-mesh configurations by including modified centre distances and modified addendums in the analysis. The maximum impingement depth possible was generally less than ten per cent of the overall tooth depth. Modifications to the standard out-of-mesh configuration were proposed to ensure the pinion is not deprived of oil jet impingement. Townsend (1985) discussed and summarised the results obtained in previous works by stating that radially targeted impingement leads to greater oil penetration into the tooth space and, therefore, is a better method than into-mesh and out-of-mesh impingement methods for cooling high-speed gears.

Akin and Townsend (1989) presented the so-called virtual kinematic model, which improved upon the initial vectorial model by generalising it to include realistic gear geometries instead of the linear rack-like assumption in the vectorial model. The kinematic model for a radial jet is depicted in Figure 2.5. The definition of $t = 0$ was similar to the vectorial model with the jet tip positioned at point 1. It then followed the path between points 1 and i and impinged on the trailing tooth at a radius of $R_\mathrm{i} = R_\mathrm{o} - v_\mathrm{j} t_\mathrm{f}$, with the outer radius R_o, the jet velocity v_j and the flight time t_f at impingement point i. The gear had to complete a rotation of θ_w for the tip of the oil jet to reach point i. θ_w was subdivided into three components: θ_o, θ_i and θ_r. The first two were calculated by using the involutes of pressure angles ϕ_o and ϕ_i at R_o and R_i by substituting

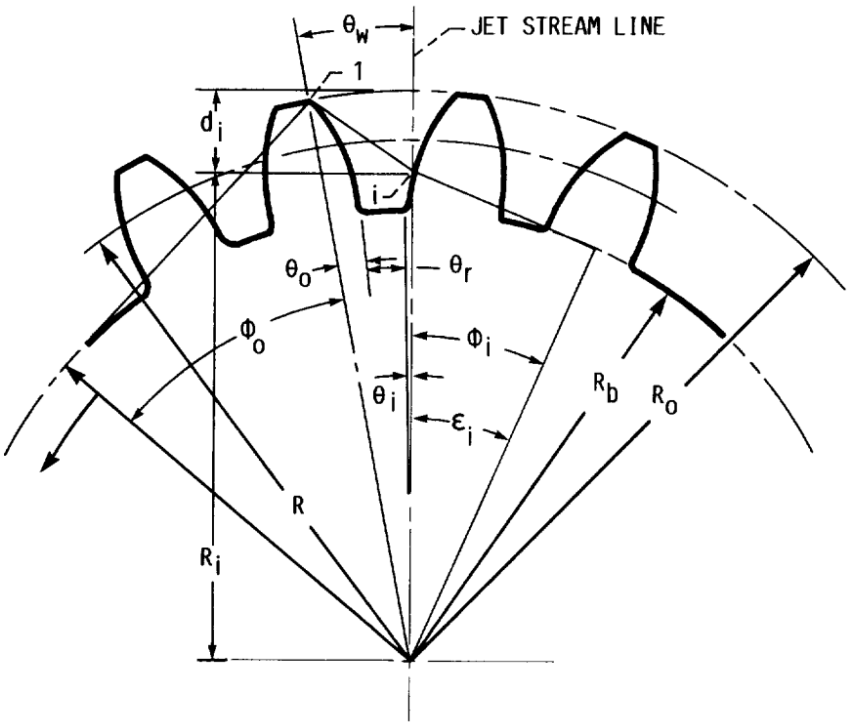

Figure 2.5: Virtual kinematic model of Akin and Townsend (1989) for radially targeted impingement.

R_a in

$$\phi = \arccos \frac{R_b}{R_a}, \tag{2.8}$$

and

$$\theta = \text{inv } \phi = \tan \phi - \phi, \tag{2.9}$$

for an arbitrary radius $R_a > R_b$. The angle θ_r was calculated with

$$\theta_r = \frac{\pi}{N} - 2\text{inv } \phi, \tag{2.10}$$

where N was the number of teeth, and ϕ was the pressure angle at pitch radius R. Since the time of flight and rotation must be equal, the equation

$$d_i = \frac{v_j \theta_w}{\omega_g} \tag{2.11}$$

could be solved iteratively for the impingement depth $d_i = R_o - R_i$ if the jet velocity v_j and the gear angular velocity ω_g were given.

The virtual kinematic model also included an arbitrary jet inclination angle relative to the radial direction (Figure 2.6). A so-called virtual base circle was required for the model. The centre of the circle was located at the gear centre. The virtual base radius R_{bv} was selected so that the jet stream line, which went through the impingement point i and was inclined at an angle of α

relative to the radial direction at the outer radius R_o, was tangential to the virtual base circle:

$$R_{bv} = R_o \sin \alpha. \tag{2.12}$$

The virtual base circle rotated with ω_j so that

$$v_j = \omega_j R_{bv}. \tag{2.13}$$

In Figure 2.6, the jet tip is located at the topland radius R_o at $t = 0$ and moves along the jet stream line with v_j for a time of t_f until impinging on the trailing tooth at point i. The distance the jet tip covers equals $v_j t_f$. If two involutes were drawn from the virtual base circle ending at R_o and R_i, they would originate at points 2 and 4, respectively. The virtual roll angle between these involutes would be

$$\epsilon_{o-i} = \omega_j t_f, \tag{2.14}$$

and the arc length

$$\omega_j R_{bv} t_f = v_j t_f, \tag{2.15}$$

fulfilling Equation 2.13. The derivation of formulation to calculate d_i is not discussed here. The resulting equation was similar to Equation 2.11:

$$d_i = \frac{v_j \theta_w \cos \alpha}{\omega_g}, \tag{2.16}$$

where θ_w included an additional term, θ_a. Keller (2022) stated that Equation 2.16 is an approximation only valid for small jet inclinations and large gears. Therefore, it was substituted by

$$d_i = R_o - \frac{\theta_w v_j \sin \alpha}{\omega_g \sin \theta_a}. \tag{2.17}$$

The base radius of the gear used by Keller (2022) was smaller than its foot radius. Therefore, a correction angle of θ_k was implemented in the definition of angles $\theta_{i,r,o}$.

Akin and Townsend (1989) conducted a parametric study with the virtual kinematic model. They showed that the jet inclination could be optimised for a given set of operational parameters if the impingement depth was to be maximised. They described the inclined targeted impingement as the most energy-efficient cooling method and stated that it is more adjustable than into-mesh and out-of-mesh impingement methods.

Another pioneering study on the subject was conducted by Schober (1983). The author used a modified version of the vectorial model to calculate the impingement depth, which considered the jet inclination and the involute shape of the tooth profile. The formulation of the model was not published. It was shown that the impingement depth could be improved for a given set of operating parameters if the oil jet was inclined. These findings were supported by the high-quality shadowgraphy images of the oil jet gear interaction (Figure 2.7). Schober (1983) could capture the deformation of the oil jet tip by the leading tooth and partially the spreading of oil film after the impingement. The change in impingement depth by varying the upstream

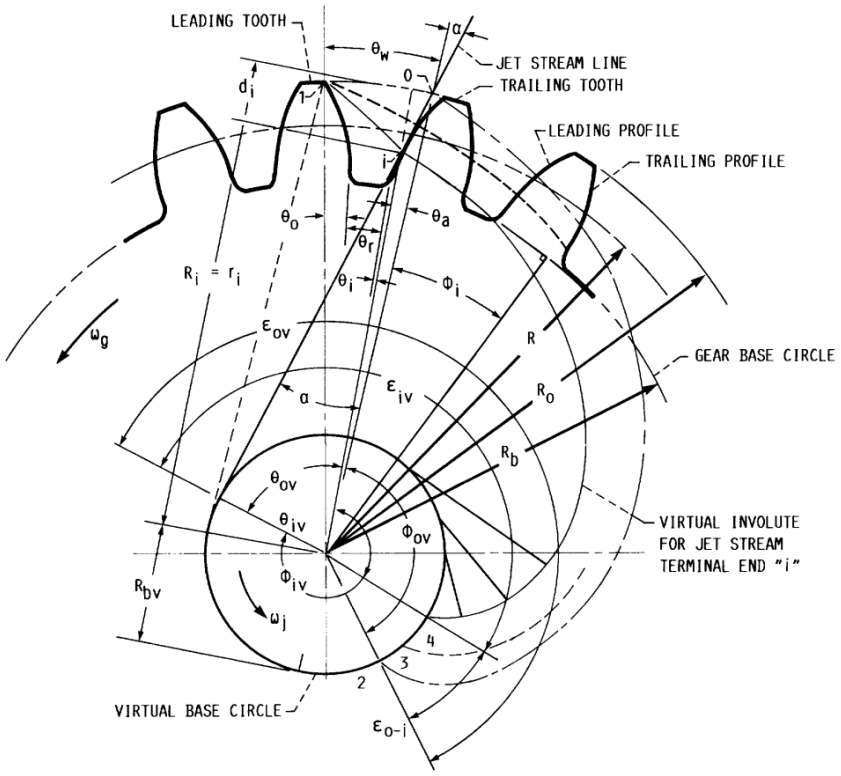

Figure 2.6: Virtual kinematic model of Akin and Townsend (1989) for inclined targeted impingement.

pressure or the jet inclination was also visually demonstrated. The cylindrical jets were not deflected by the gear windage.

Von Plehwe (2022) introduced the impingement angle β as another key figure to describe the oil jet gear kinematics (Figure 2.8a). The model was an extension of the vectorial model of Akin et al. (1975) to account for inclined jets, similar to the aforementioned modification by Keller (2022) (Equation 2.7). The impingement angle was calculated by

$$\beta = \arctan\left(\frac{u_\mathrm{z} - u_\mathrm{s}\sin\alpha}{u_\mathrm{s}\sin\alpha}\right), \tag{2.18}$$

with the circumferential gear velocity u_z at the topland radius, the jet velocity u_s and the jet inclination α. Limiting impingement angles were defined to differentiate between operating points regarding which part of the tooth the impingement started on (Figure 2.8b). According to the model, the oil jet could impinge on the passive flank for $\beta < 28.7°$ and the bottomland for $\beta < 33.8°$. At $\beta = 60.3°$, the position of the jet tip, in other words, the relative velocity u_r, was orthogonal to the gear flank. For $\beta \geq 60.3°$, the jet would not have a tangential velocity component on the gear flank in the direction of the bottomland. Von Plehwe (2022) claimed that further oil penetration was not expected for this case.

Fondelli et al. (2015) utilised computational fluid dynamics (CFD) to numerically investigate the oil jet gear kinematics. The study was focused on the losses induced by the impinging oil jet. A mesh sensitivity analysis was undertaken to generate the reference numerical setup, with

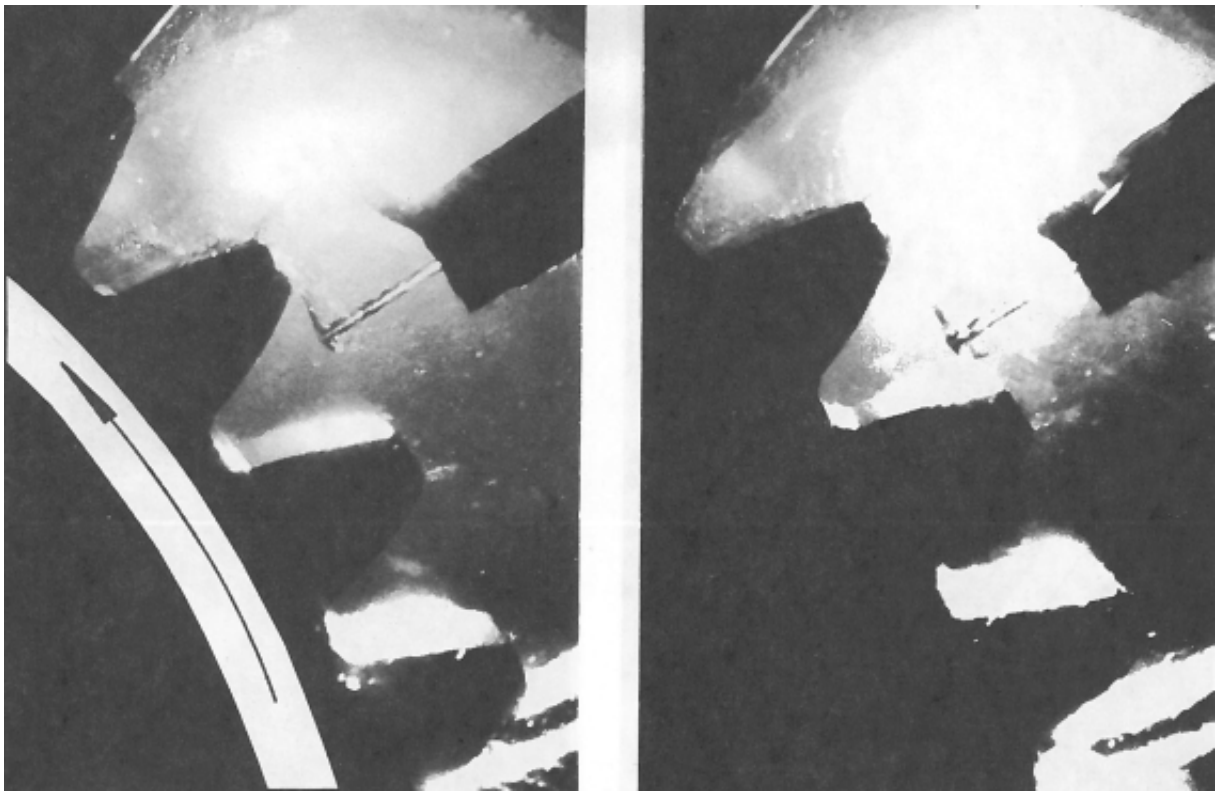

Figure 2.7: Shadowgraphy images of oil jet gear interaction (Schober (1983)).

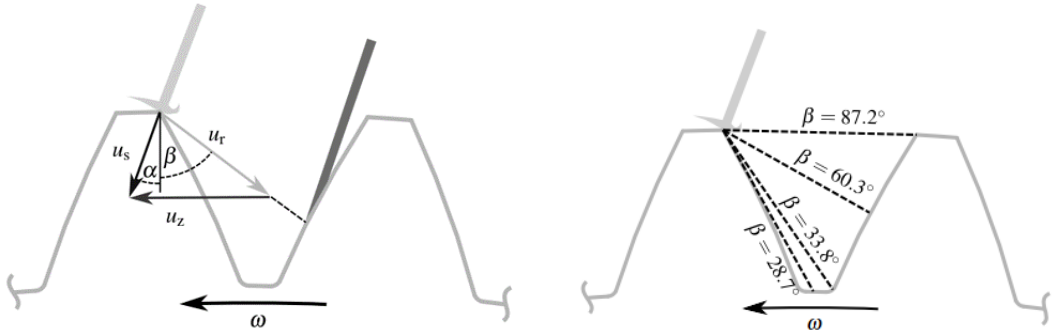

(a) (b)

Figure 2.8: Extended vectorial model of von Plehwe (2022).

which the volume-of-fluid (VOF) simulations were conducted. The authors have shown that the oil jet forms an oil film suspended over the topland (Figure 2.9).

Keller et al. (2019) observed the same phenomenon in their three-dimensional single-phase simulations with Smoothed Particle Hydrodynamics (SPH). The simulations were conducted to study the oil flow during and after the impingement. Three setups with varying jet inclinations were simulated. The flow phenomena for the radial jet are depicted in Figure 2.10. Figure 2.10a is a snapshot taken at the start of impingement at the third tooth. The deformation of the jet tip due to the impingement on the leading tooth was visible. The jet tip was still connected to the leading tooth by oil ligaments with a deformed jet tip, similar to the experimental observation of

(a) (b) (c) (d)

Figure 2.9: The deformation of oil jet tip observed in the numerical simulations of Fondelli et al. (2015).

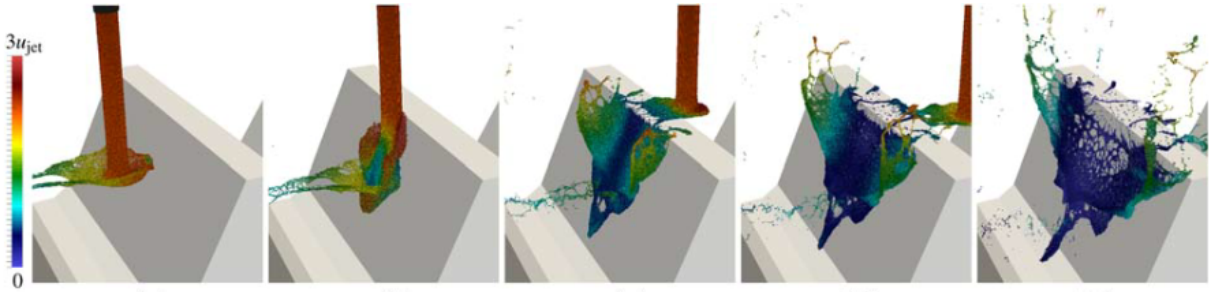

Figure 2.10: The oil jet gear interaction in SPH simulations of Keller et al. (2019).

Schober (1983). After the initiation of the impingement, the impingement point moved upwards, and an oil film started to form (Figure 2.10b). The oil film quickly spread in the axial direction of the gear and detached from the gear flank (Figure 2.10c). Meanwhile, a portion of the oil film continued penetrating towards the bottomland. The dry-out effect in Figure 2.10e was explained by the resolution of the simulations not being high enough to capture the thin oil film accurately. Increasing the jet inclination changed the spreading of the oil film. The detachment in the axial direction and, therefore, the amount of oil splashing away in the form of ligaments and droplets were decreased.

Keller et al. (2020) studied the oil jet gear interaction and the oil flow utilising VOF. 21 cases with varying jet velocities, jet inclinations, jet diameters and rotational speeds were investigated. Snapshots from the so-called baseline case are shown in Figure 2.11. Keller et al. (2020) divided the oil flow phenomenology into three phases. In the first phase, the oil jet penetrated into the tooth gap. The jet was neither deflected nor broken up by the gear windage. In the second phase, the oil jet impinged on the gear flank. The third phase consisted of oil film spreading and splashing away from the gear. The authors gathered the impingement depths D_i for the simulated cases, which were then compared to the analytical solutions calculated with the virtual kinematic model of Akin and Townsend (1989). The numerical and analytical results showed good agreement. However, the numerical impingement depths were smaller than the analytical predictions. As mentioned before, Akin and Townsend (1989) had explained the difference between their experimental and analytical results for a given upstream pressure by the viscous losses in the nozzle. However, this explanation would not be valid for the numerical case since the jet velocity was set as a boundary condition. Keller et al. (2020) proposed that the deflection and the deformation of the jet tip by the leading tooth might have reduced the impingement depth. The authors also provided quantitative data on the penetration depth D_p for the first time, which was approximately twice the impingement depth for the simulated cases. Both impingement and

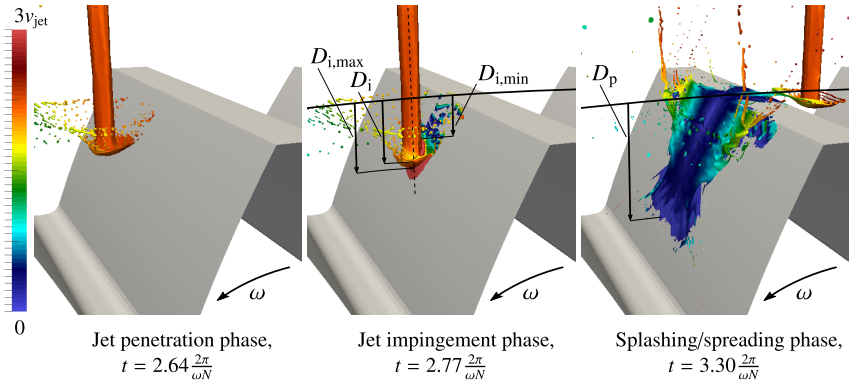

Figure 2.11: The oil jet gear interaction in VOF simulations of Keller et al. (2020).

penetration depths were higher at moderate jet inclinations and reduced significantly at extreme inclinations (Figure 2.12a). Furthermore, the temporal variation of the wetted area A_w and the oil film volume V_w were presented (Figure 2.13). Both increased rapidly after the impingement. The wetted area increased over time, and no de-wetting was observed. The oil film volume started decreasing after the impingement. Only 20% of the oil volume was contained within the film at the end of the simulation. The initial sudden decrease in the oil flow volume was attributed to the splashing observed in Figure 2.11. The slighter decrease afterwards was credited to the centrifugal fling-off. The wetted area, which the authors considered an important indicator for the cooling and lubrication performance, behaved similarly to the impingement and penetration depths with varying jet inclination (Figure 2.12b). An increase in the velocity ratio

$$\Sigma = \frac{v_{jet}}{v_p}, \tag{2.19}$$

with the jet speed v_{jet} and the circumferential gear speed at the pitch radius v_p, led to an increase in the wetted area for the investigated radially targeted impingement cases. A comparison of cases III and V, which had the same velocity ratios but different jet and gear velocities, showed that the size of wetted areas was similar even though the velocities differed greatly. Therefore, inertial forces, not centrifugal forces, were suspected of dominating the initial oil film spreading. If the volume flow rate was constant, smaller jet diameters resulted in greater wetted areas. However, larger jets led to better wetting when the velocity ratio was kept constant. Keller (2022) discussed the simulated case of Keller et al. (2020) in more detail with snapshots of simulations and wetting maps and derived empirical correlations for the penetration depth and the wetted area.

The first study modelling the cooling capabilities of oil jet impingement was published by DeWinter and Blok (1974). They developed an analytical model, the so-called fling-off cooling model, which assumed that the quadratic tooth space was initially filled with the coolant after the jet impingement. The coolant then withdrew heat from the tooth surface and got flung off during gear rotation. The fling-off model was used by van Heijningen and Blok (1974) to compare hypothetical continuous cooling against intermittent cooling via oil jet impingement. They also implemented a variable viscosity in their evaluation. Terauchi et al. (1989) and El-Bayoumy et al. (1989) modified the fling-off model to account for a limited initial film height

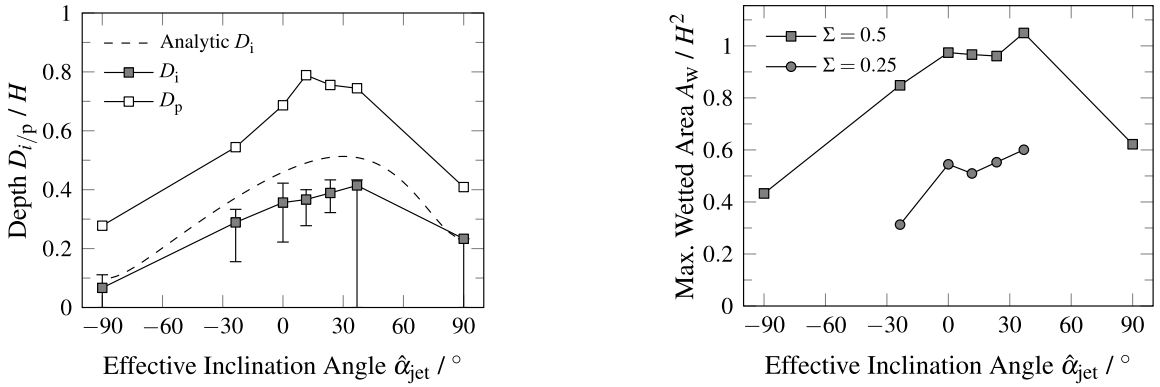

Figure 2.12: Variation of impingement depth, penetration depth and wetted area with the effective inclination angle of the oil jet (Keller et al., 2020).

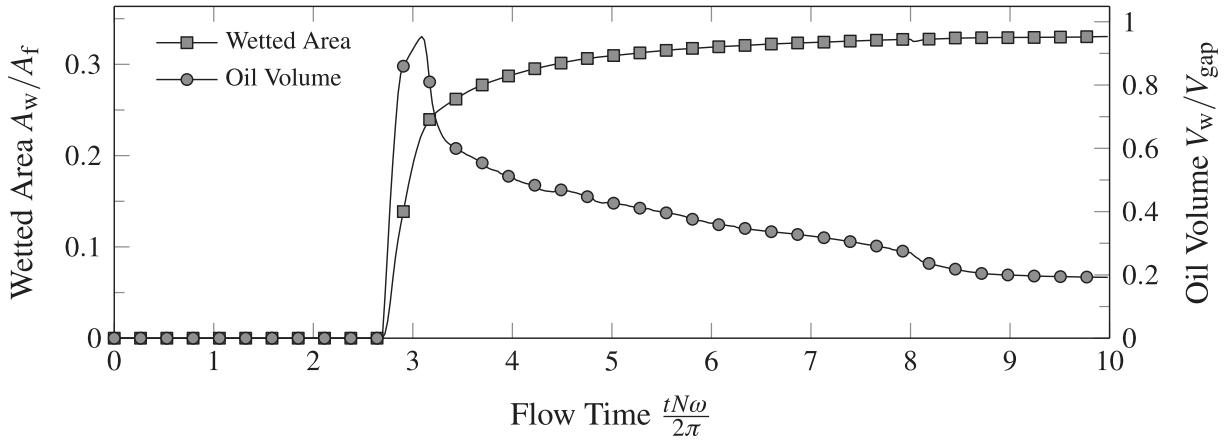

Figure 2.13: Variation of wetted area and oil volume in the tooth space with time (Keller et al., 2020).

and a limited oil penetration, respectively. Kromer et al. (2020) have limited the wetted area in the fling-off model and compared the results to experimental data. They found that the heat transfer coefficient strongly correlated with the oil flow rate and correlated negatively with the rotational speed.

The fling-off model has been used in numerous publications to estimate the heat transfer coefficient for thermal modelling. Patir and Cheng (1979) presented a heat transfer model based on finite element analysis (FEA). The modelled tooth geometry is depicted in Figure 2.14a. The surfaces q and p were modelled as periodic surfaces. The hub-facing surface s was modelled as a rotating disk. The tooth surfaces t and meshing surface m were subjected to a heat transfer coefficient, calculated via the modified fling-off model of van Heijningen and Blok (1974). An additional frictional heat input was applied on the meshing surface. The authors indicated that the heat transfer coefficient on the tooth and meshing surfaces was one of the most uncertain quantities. Townsend and Akin (1981) utilised a similar approach (Figure 2.14b). The tooth surfaces were divided into those impinged by the oil jet j and those not impinged t. The active flank was divided along the impingement depth, calculated with the virtual kinematic model. It

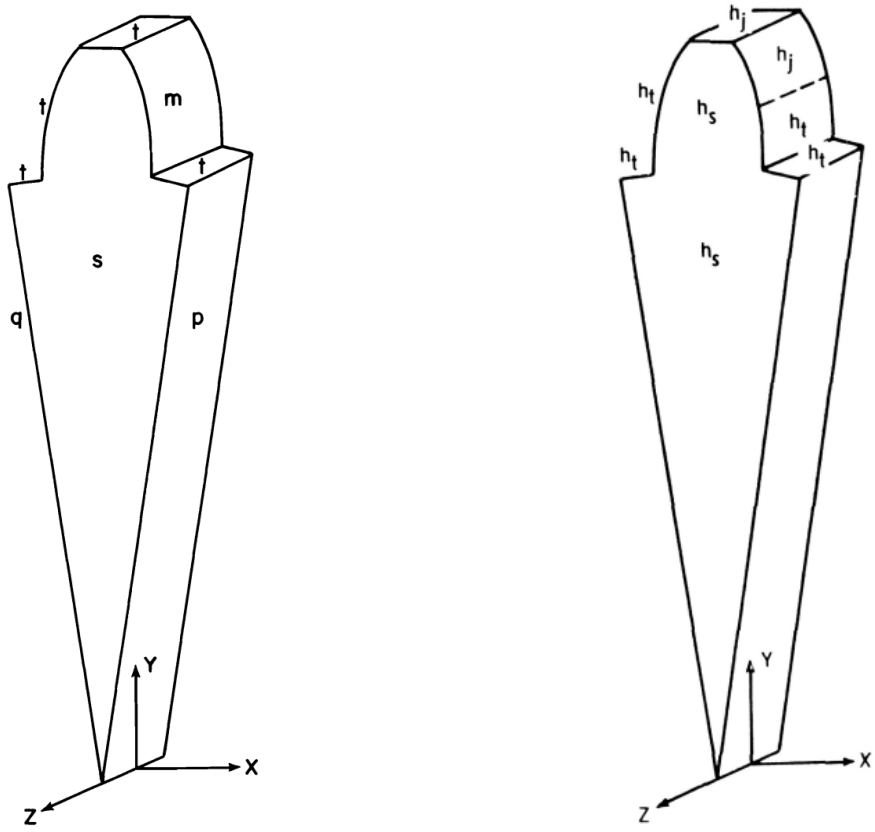

(a) (b)

Figure 2.14: FEA models of tooth geometry by Patir and Cheng (1979) (a) and Townsend and Akin (1981) (b).

should be noted that the formulation differed from the kinematic model published later by Akin and Townsend (1989). The heat transfer coefficient h_j was initially calculated via the modified fling-off model of van Heijningen and Blok (1974). The simulated temperatures were much higher than expected. h_j was adjusted to produce results more in line with the experiments. On the contrary, Long et al. (2003) reported a very good agreement between experimental results and FEA predictions, where the oil jet heat transfer was modelled with the fling-off model. Nevertheless, their sensitivity analysis showed that the heat transfer coefficient on the gear flank had a subordinate effect in their setup. A change of 10% in heat transfer coefficient led to only around ±1% change in surface temperatures. Handschuh (1995) used finite element analysis with assumed heat transfer coefficients on the gear surface and compared the results to the experimental data. The assumed heat transfer coefficients were used because of a lack of available data on heat transfer. This absence of reliable data also led other more recent publications (Fernandes et al., 2018; Gan et al., 2019; Hu et al., 2021; Li and Tian, 2017; Wang et al., 2017; Zhang et al., 2017) on different gear geometries to use similar assumptions to model the heat transfer coefficient on the gear surface.

Experimental research on the thermal aspect of impingement cooling of gears has also been limited in the past. Townsend and Akin (1981) conducted experiments to measure the gear tooth

temperatures at varying operational parameters. The oil jet impinged radially on the passive flank of one of the gears on the disengaging side of the meshing. The temperature measurement was conducted via an infrared microscope. Raising the rotational speed and the load resulted in increased gear surface temperatures, whereas an increase in the oil jet pressure decreased it. Schober (1983) measured oil temperatures at the nozzle inlet and the drain of the casing, as well as the bulk temperature of the pinion. The latter was not accomplished during rotation but only after the gears completely stopped. The author determined the heat flow rate transferred from the gears to the oil, utilising the nozzle and drain temperatures. The dependency of the heat flow rate on varied operational parameters was limited to an out-of-mesh impingement configuration, where the heat flow rate grew with the oil flow rate. Leoni (1991) determined the heat transfer coefficient on loaded gears. The total oil flow rate was divided into a lubricant flow with into-mesh impingement and a coolant flow with axial impingement on the inner part of the gear. An increase in lubricant flow improved the heat transfer coefficient, whereas an increase in oil jet velocity did not increase the heat transfer coefficient. The author noted that the oil temperature in the proximity of the gear and more information on losses were required to improve the accuracy of the heat transfer coefficient determination. Handschuh (1992) measured stationary temperatures on a spiral bevel pinion with oil jet impingement lubrication. Additionally, an infrared microscope was utilised to collect transient data. The position of the oil jet, the transmitted load and the oil flow rate were varied. Increasing the oil flow rate decreased the measured temperatures, whereas increasing the transmitted load had the opposite outcome. Into-mesh and out-of-mesh impingement resulted in the lowest temperatures with no significant difference between both options. These publications helped understand the dependencies and tendencies qualitatively, but none of them quantified the heat transfer between the oil jet and the gear for generalised use.

Von Plehwe et al. (2021) addressed this shortcoming by developing a new methodology to investigate the heat transfer between impinging oil jets and single spur gear. The experimental method was based on stationary and spatially resolved temperature measurements on the gear surface. An iterative FEA was conducted to determine the heat transfer coefficients. They showed that heat transfer depended on the rotational speed in a complex manner. Figure 2.15 shows the change of surface-averaged Nusselt number $\overline{\mathrm{Nu}}$ over the rotational Reynolds number Re_ω for different jet Reynolds numbers Re_d at a constant jet inclination of $\alpha = 20°$. The authors defined three effects that influence $\overline{\mathrm{Nu}}$:

A: An increase in the impingement depth enhanced the area on the gear tooth with high local heat transfer coefficient values. $\overline{\mathrm{Nu}}$ increased accordingly.

B: The heat transfer on the passive flank declined above a Re_ω threshold, which could be explained by a decreased amount of oil on this surface.

C: At higher impact velocities, the boundary layers on the gear tooth are thinner. Therefore, increasing the relative impingement impulse also increased $\overline{\mathrm{Nu}}$.

In the so-called low-speed zone "L", the oil jet reached the bottomland of the tooth regardless of the rotational speed. Therefore, an increase in the rotational Reynolds number did not decrease effect A but increased the relative impingement impulse and effect C. This led to an increase

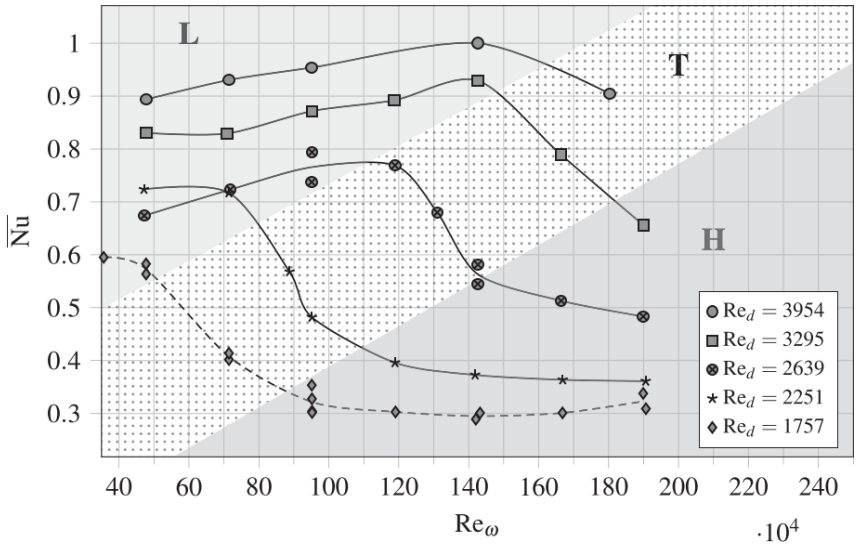

Figure 2.15: Change of surface-averaged Nusselt number with jet and gear Reynolds numbers (von Plehwe et al., 2021).

in $\overline{\text{Nu}}$. In the transition zone "T", the gear started to rotate too fast for the oil jet to reach the bottomland. Therefore, the impingement depth was reduced when the rotational speed was increased. The heat transfer on the passive flank also decreased. Declines in effects A and B reduced $\overline{\text{Nu}}$. $\overline{\text{Nu}}$ stagnated in the high-speed zone "H" since the decreases in effects A and B were cancelled out by the increase in the relative impingement impulse (effect C). Similar to the findings of previous publications, an increase in the oil jet velocity (Re_d) and, therefore, oil volume flow rate led to higher values of $\overline{\text{Nu}}$.

Von Plehwe et al. (2021) further investigated the influence of varying jet inclination from $\alpha = 20°$ to $\alpha = 0°$ on $\overline{\text{Nu}}$ behaviours at three Re_d over the Re_ω range (Figure 2.16). The change of $\overline{\text{Nu}}$ with Re_ω was almost identical at the lowest Re_d. However, higher $\overline{\text{Nu}}$ values were observed for the operating points within the low-speed zone at higher Re_d. The transition also occurred at a lower Re_ω. These observations were attributed to the increased relative velocity of the oil jet. The differences decreased in the transition and high-speed zones.

Von Plehwe (2022) has complemented the results with a more detailed analysis of each operational parameter's effect on heat transfer. Similar results as von Plehwe et al. (2021) were reported for the effects of Re_ω and Re_d. The first part of the jet inclination investigation was conducted over the Re_ω range with $\alpha = 20°$ and $\alpha = 45°$. In contrast to the previous results, $\overline{\text{Nu}}$ experienced a continuous decline over increasing Re_ω at $\alpha = 45°$. In the second part, the jet inclination was varied for a selected pair of values for Re_d and Re_ω (Figure 2.17). $\overline{\text{Nu}}$ varied only within $0.54 \leq \overline{\text{Nu}^*} \leq 0.62$ for the measurements with jet inclination varying between $-30°$ and $20°$. An increase above $20°$ resulted in a decrease of $\overline{\text{Nu}^*}$ to 0.475 at $45°$. This reduction was explained by a decline in the heat transfer on the passive flank. The author reported that the jet inclination influenced the surface-averaged heat transfer less than the rotational speed and the oil volume flow rate.

Von Plehwe (2022) also derived an empirical correlation to predict the surface averaged heat

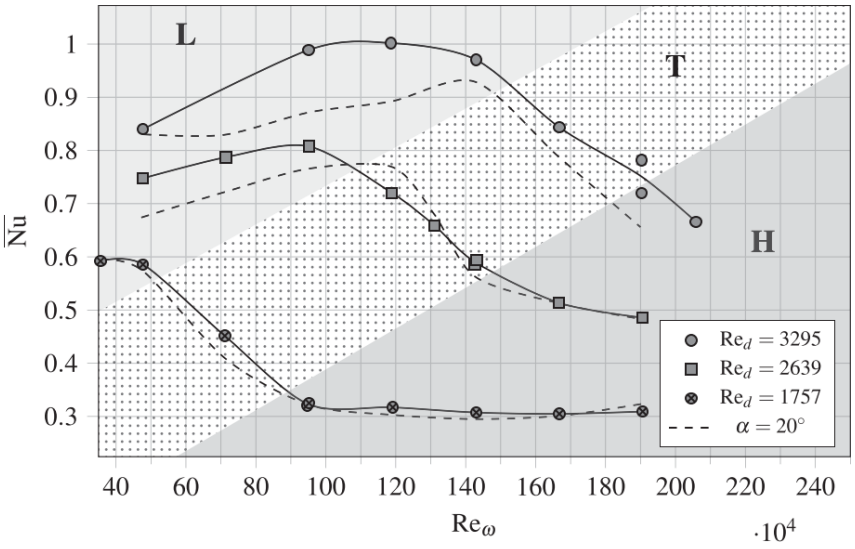

Figure 2.16: Effect of jet inclination on surface-averaged Nusselt number at various jet and gear Reynolds numbers (von Plehwe et al., 2021).

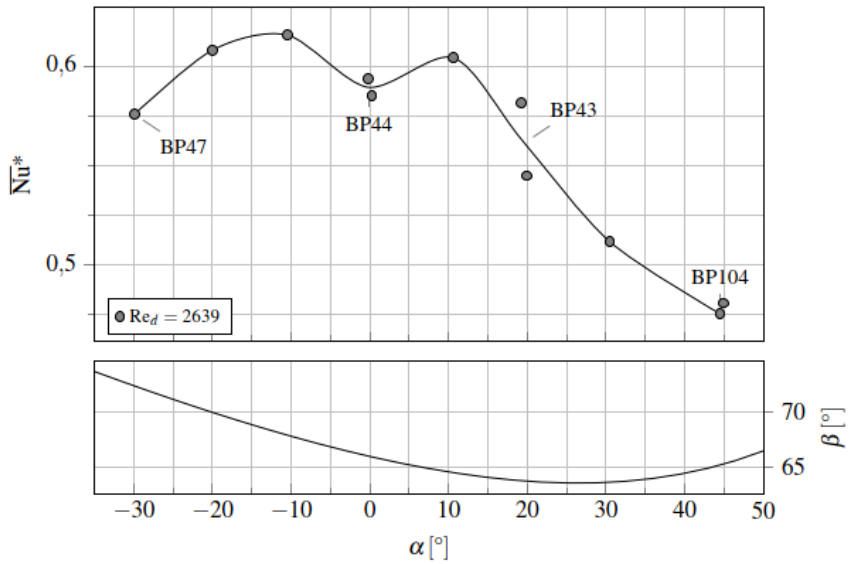

Figure 2.17: Effect of jet inclination on surface-averaged Nusselt number at constant jet and gear Reynolds numbers (von Plehwe, 2022).

transfer coefficient with the impingement angle β and the relative jet velocity u_r. The author observed flow separation in the nozzle above a specific oil volume flow rate. However, the change in the oil jet flow and the velocity due to the flow separation was not investigated. Since both β and u_r depended on the oil jet velocity, two different correlations were required for the attached and separated jets. Each correlation consisted of two polynomial equations valid for different β ranges.

Ayan et al. (2022a) installed a second gear in the experimental setup to investigate the effects meshing had on the heat transfer. The second gear was geometrically identical to the gear used by von Plehwe et al. (2021), albeit not instrumented. The temperature measurements and heat

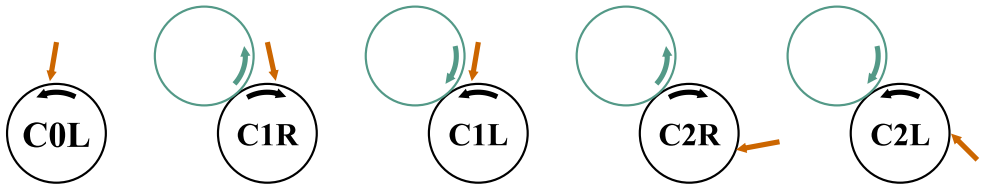

Figure 2.18: Schematic representation of the jet impingement configurations investigated by Ayan et al. (2022a).

transfer coefficient determination were carried out for the instrumented gear. The configurations investigated are depicted in Figure 2.18. The black circle is the instrumented gear rotating in the direction of the black arrow. The green circle is the non-instrumented gear in meshing configurations with the rotational direction denoted by the green arrow. The orange arrows symbolise impinging oil jets. C0L was the base configuration, consisting only of the single gear as in the setup of von Plehwe et al. (2021). Configuration C1R and C1L were the extreme cases, with the shortest and longest times a tooth needed to reach the meshing zone after being impinged by the oil jet, respectively. These configurations were comparable to Methods B2 and B1 in Figure 2.1. C2R and C2L were cases between both extremes utilised to investigate the influence of the distance between impingement and meshing zones. This distance was expressed as a percentage of completed rotation between the jet position and the pitch point. The distances were 91.4%, 8.6%, 63.1% and 36.9% of one rotation for C1R, C1L, C2R and C2L, respectively.

Ayan et al. (2022a) found that the emerging losses influenced the measured temperatures significantly, even if the gears were not loaded. A further investigation of these losses showed that the trapping losses correlated very well with the increase in the determined heat transfer coefficients. Nevertheless, they were able to deduct qualitative conclusions about the influence of meshing on inclined impingement using the measurements with 2000 RPM, where the trapping losses were relatively low. No significant difference was observed between the single gear (C0L) and meshing gear measurements regarding the surface-averaged heat transfer coefficient. Nonetheless, the spatial distribution of the heat transfer coefficient on the active flank was more uniform if the impingement took place 8.6 % away from the engaging side of meshing (C1L). The uniformity diminished when this distance was increased. In a later publication, Ayan et al. (2024) developed a loss correction model to evaluate measurements with higher rotational speeds. This model assumed that the measurements with the maximum distance between impingement and meshing (C1R) should result in identical heat transfer coefficient distributions as the measurements without meshing. These measurements were repeated with the opposite directional rotation (C0R in Figure 2.19) to eliminate possible errors arising from rotational direction dissimilarities. The heat transfer coefficient of C0R measurements was applied as a boundary condition in the FEA simulation. The evaluation method was modified to calculate an effective oil temperature resulting in the measured temperatures of C1R. The required heat flow rate $\dot{Q}_{\mathrm{oil,trapping}}$ for the oil volume flow to reach the calculated effective temperature was determined. A comparison with the experimentally determined total trapping losses P_{trapping} showed a good correlation with $\dot{Q}_{\mathrm{oil,trapping}}$. Since P_{trapping} did not differ significantly for each

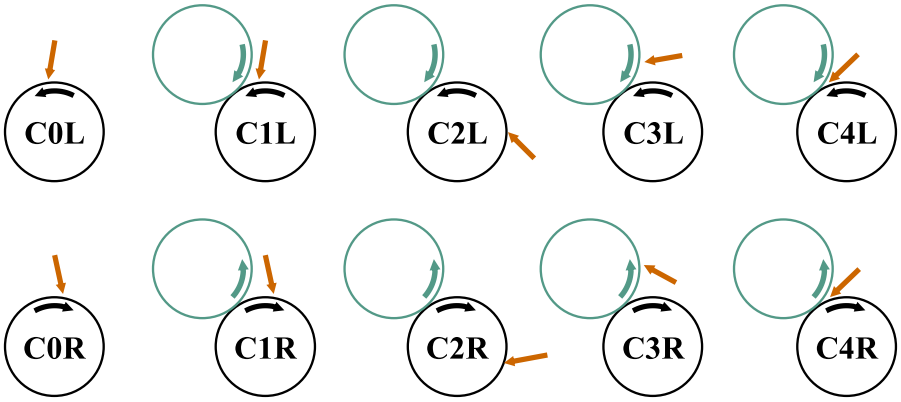

Figure 2.19: Schematic representation of the jet impingement configurations investigated by Ayan et al. (2024).

configuration, the fitting function derived for $\dot{Q}_{\text{oil,trapping}}$ was used in each measurement. The results obtained with the loss correction were consistent with the previous publication. No clear correlation was observed between the average heat transfer coefficient and the impingement-meshing distance over the rotational speed range. The local distribution on the active flank got more uniform with decreasing distance.

Furthermore, the authors compared the heat transfer coefficients of targeted, into-mesh (C4L) and out-of-mesh (C4R) impingement methods. Out-of-mesh impingement resulted in the lowest surface-averaged heat transfer coefficient for almost all operating points. Additionally, its spatial distribution was limited to the passive flank. Out-of-mesh impingement would not be able to cool down the thermally highly loaded part of the tooth since the friction heat and temperature increase are expected on the active flank in a loaded application. Into-mesh impingement led to a more practical heat transfer coefficient distribution, with high heat transfer areas on the active flank. It was shown that the heat transfer could be limited to the active flank or expanded onto the passive flank depending on the oil jet and circumferential velocities. The surface-averaged heat transfer coefficient was less than what was achievable with the targeted impingement. The authors showed that the heat transfer with the targeted impingement is not limited to the directly impinged gear. The secondary gear also experienced high levels of heat transfer if the impingement took place on the engaging side of the gears (C3L). It was also noted that the heat transfer with targeted impingement could be optimised by modifying the jet inclination depending on the operating parameters, such as the rotational speed and the oil volume flow rate. A comparable level of control would not be achieved with into-mesh and out-of-mesh impingement methods.

As presented in this chapter, the oil jet impingement cooling of a gear depends on numerous operational parameters, such as the rotational speed of the gear, oil volume flow rate, oil jet inclination, as well as geometrical parameters of both the gear and the oil jet. For gearbox developers, constructing an experimental setup to investigate numerous combinations of these parameters is costly and often unfeasible. A preliminary parameter study can be conducted with

simplified analytical or numerical models to limit the number of parameters and their variation before undertaking such an extensive experimental study. However, such models must first be validated by utilising reliable experimental data. The experimental setup and methodology of von Plehwe et al. (2021) enabled the acquisition of the necessary data for single spur gears. The present work builds upon the foundation they laid. The first objective of this work is to increase the measurement accuracy of their experimental setup by developing and implementing a new calibration process for the telemetry system and validating the evaluation methodology to ensure the reliability of the collected experimental data (Chapter 3).

Ayan et al. (2024) demonstrated that the so-called targeted impingement (Method B in Figure 2.1) bears the highest cooling potential among the previously described oil jet impingement configurations. This potential can be fully exploited by optimising the operational and geometrical parameters for enhanced heat transfer. Such optimisation can only be achieved if the significant parameters influencing heat transfer are well understood and characterised. Research prior to von Plehwe (2022) has only provided fundamental qualitative conclusions such as "a higher oil flow rate results in lower gear temperatures" or "a deeper impingement leads to better cooling performance". Von Plehwe (2022) was the first to correlate the surface-averaged heat transfer coefficient with the relative jet velocity and impingement angle. He postulated that his correlations for the attached and separated jets might collapse into one if the change in oil jet diameter is accounted for. However, this postulation is incorrect, as demonstrated in Chapter 4, where the oil jet flow regimes are investigated experimentally and numerically to understand how the flow separation affects the oil jet's diameter and velocity. This outcome reinforces the purpose of the second and main objective of the present work: characterising and deriving the so-called significant parameters from a wide range of operational and geometrical parameters and describing their quantitative influence on heat transfer. To this end, the test matrix of von Plehwe (2022) is extended by including new measurements with a different nozzle diameter and variation in the number of nozzles. The significant parameters are determined by analysing the results from this extended test matrix. A so-called optimal test matrix is generated to investigate the significant parameters. The measurements within this optimal test matrix are analysed regarding the influence of the significant parameters on the surface-averaged heat transfer coefficient and its spatial distribution. A novel empirical model is developed to predict the surface-averaged heat transfer coefficient. The model is used to predict the heat transfer coefficient of cases simulated by Keller (2022), demonstrating how well the predicted heat transfer coefficient correlates with the numerically determined wetted area. Exemplary optimisation scenarios are presented to discuss the potential of the empirical heat transfer model. The characterisation of the significant parameters, the development of the empirical model and the results obtained with it are discussed in Chapter 5.

3 Experimental Methodology of Heat Transfer Coefficient Measurements

The experimental setup employed for this work was initially developed by von Plehwe (2022). It is designed to allow an investigation of heat transfer between impinging oil jets and a single spur gear based on discrete temperature measurements. The test rig, the instrumentation, the evaluation methodology and the novel calibration scheme are described in the following.

3.1 Test Rig

The test rig employed for the experiments can be divided into three main systems: one system for the oil supply, one system for the rotating components and one system for the air supply. The layout of the test rig is depicted in Figure 3.1 with a colour coding for each system.

The orange components in Figure 3.1 constitute the oil supply system. The operation with a constant oil temperature is ensured by separating the oil supply cycle for the experiments from the oil heating cycle. The heating cycle consists of a circulating pump and a heater with temperature regulation, keeping the oil in the tank at a constant temperature. The supply cycle consists of the feed pump, the flow meter, the spraybar and the return pump. The feed pump can deliver an oil flow of up to 19.2 l/min and 15 bar. The flow meter determines the volume flow rate using the Coriolis principle to measure the mass flow rate and the fluid density. A pressure sensor is installed downstream of the flow meter to monitor the oil pressure. The oil then flows through the so-called spraybar with nozzles drilled into it. These nozzles generate the oil jets that impinge on the rotating gear. The oil flung off by the rotating gear is collected on the bottom of the casing, depicted in grey in Figure 3.1. The return pump functions as a scavenge pump to prevent overfilling of the casing and to feed the oil back into the tank.

The rotor system, black in Figure 3.1, consists of the electrical motor, the torque and rotational speed sensor unit, the instrumented hollow gear and the telemetry unit. The instrumentation of the gear will be described in detail in the next section.

The third system, depicted in blue in Figure 3.1, is required for the air supply. The measurement principle of the experimental setup presupposes a temperature gradient, preferably in the radial direction, to enable a reliable determination of the heat transfer coefficient. This gradient is generated by ejecting cooling air onto the inner surface of the hollow gear. The cooling air is supplied by a side-channel blower sucking air from the environment. The compression by the blower results in an increased air temperature. The airflow is cooled down with water cooling in a heat exchanger. The cooling air settles in the plenum chamber, from which it further flows into the so-called cooling cylinder. The cooling cylinder has holes drilled into it, from which the cooling air jets get ejected.

Contrary to typical gearbox applications, the oil used in the experiments is at a higher temperature than the gear and heats the gear up instead of cooling it down. Therefore, the temperature and viscosity of the oil decrease after the oil jet impinges on the gear. This might lead to wetting dynamics that differ from the real-world application, where the viscosity increases after the

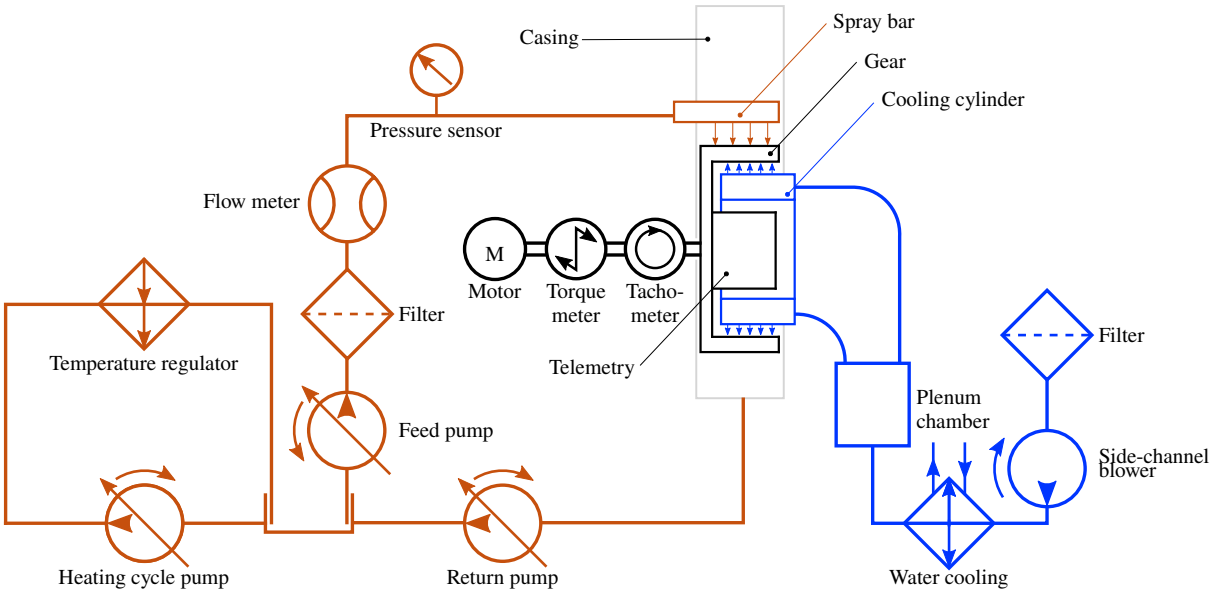

Figure 3.1: Schematics of the experimental setup (Ayan et al., 2024).

impingement. Nevertheless, this heat transfer inversion is necessary to conduct experiments with oil temperature and viscosity that resemble real-world applications. A significantly higher gear temperature would be required if the oil at $T_{\mathrm{oil}} = 80$ °C was used as a heat sink. However, the rated maximum operating temperature of the telemetry unit is 80 °C and faulty behaviour was observed when the telemetry temperature exceeded 60 °C. Alternatively, the oil could be kept at a much lower temperature. Nevertheless, this would severely deteriorate investigations' transferability due to the viscosity increasing exponentially for decreasing temperatures, as noted by Glahn (1995).

Figure 3.2 reveals the schematics of the experimental setup from a frontal view, with the spraybar, the gear and the cooling cylinder. The gear and spraybar's constant geometrical parameters are listed in Table 3.1. The variable parameters are of vital importance for the investigation of heat transfer. The only variable gear parameter is its rotational speed, which can be varied within 1000 RPM $\leq N \leq$ 6000 RPM. However, speeds higher than 4000 RPM have caused irreparable damage to some thermocouples and are therefore omitted. On the oil supply side of the experimental setup, the spraybar can be changed to realise different nozzle diameters d_{n} and nozzle numbers n_{n}. Three different spraybars are used for this work, called J100, J101 and J102. Spraybar J100, also used by von Plehwe (2022), has four nozzles of the so-called type N115, with a diameter of $d_{\mathrm{n}} = 1.15$ mm and a length of $l_{\mathrm{n}} = 6.9$ mm. Spraybar J101 also has four nozzles, albeit of type N082, with a smaller diameter of $d_{\mathrm{n}} = 0.82$ mm and a smaller length of $l_{\mathrm{n}} = 4.8$ mm. Spraybar J102 consists of eight nozzles of type N082. The spraybar properties are listed in Table 3.2.

The total oil volume flow rate $\dot{V}_{\mathrm{oil}}$ (up to 19.2 l/min) and the oil temperature T_{oil} (up to 120 °C) are also variable operational parameters. The inclination of the oil jets can be varied in a range of $-45° \leq \alpha_{\mathrm{n}} \leq 45°$. A positive inclination is defined as the oil jet being directed in the same direction as the circumferential velocity of the gear at the impingement point. For example,

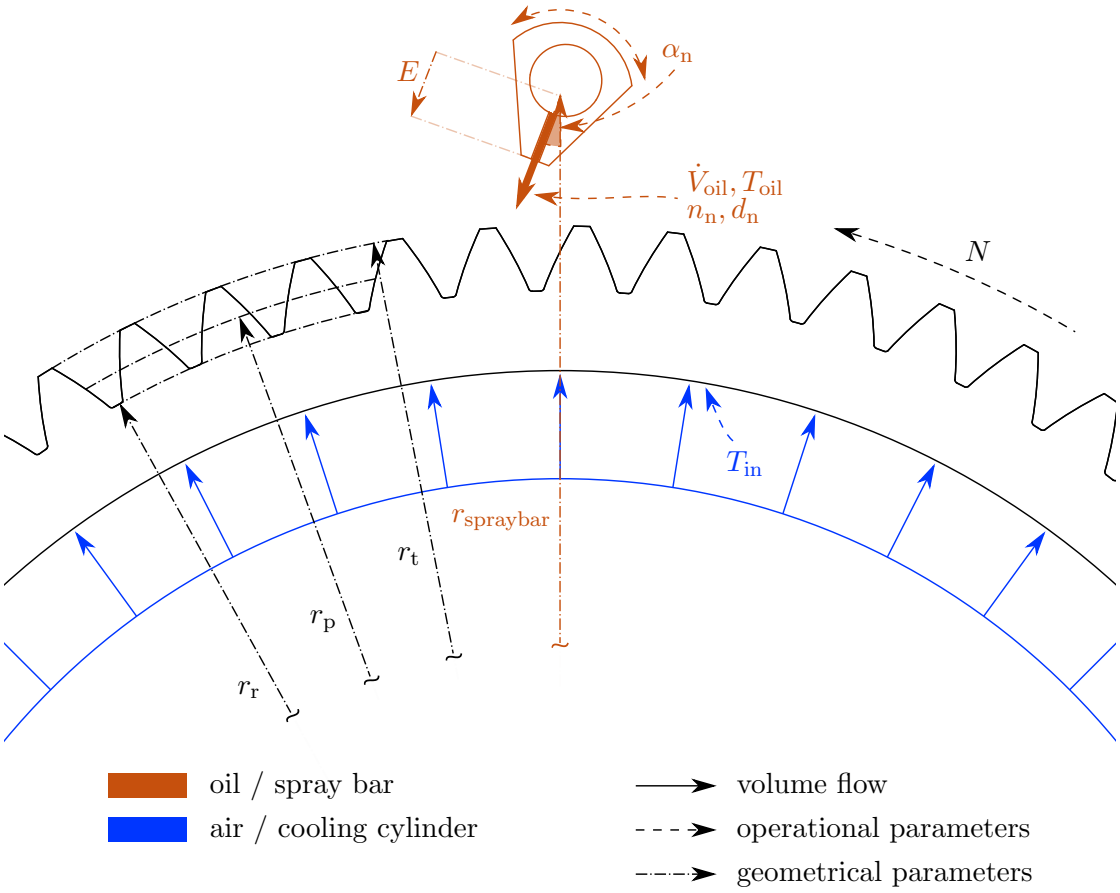

Figure 3.2: The experimental setup with the spraybar (orange), the gear (black), and the cooling cylinder (blue).

Table 3.1: Geometrical parameters of the experimental setup.

Parameter	Symbol	Value
Number of teeth	Z	65
Tooth module	m	4 mm
Pressure angle	γ	25°
Profile shift	x	+1 mm
Gear width	W	90 mm
Root radius	r_r	126 mm
Tip radius	r_t	135 mm
Pitch radius	r_p	130 mm
Spraybar axis offset	$r_{spraybar}$	153 mm
Nozzle outlet eccentricity	E	9.8 mm

in Figure 3.2, where the gear rotates counter-clockwise, the inclination angle is positive if the spraybar is rotated clockwise.

Table 3.2: Geometrical parameters of the spraybars.

Spraybar	Nozzle type	d_n [mm]	l_n [mm]	$\frac{l_\mathrm{n}}{d_\mathrm{n}}$ [mm]	n_n
J100	N115	1.15	6.9	6	4
J101	N082	0.82	4.8	5.85	4
J102	N082	0.82	4.8	5.85	8

3.2 Instrumentation

The instrumentation of the gear is configured with spraybar J100 featuring four nozzles, ensuring that each jet impinges on the middle of a tooth quarter. Due to identical nozzle geometries and the positioning of oil jets on each tooth quarter, the fundamental processes of impingement and heat transfer on each tooth quarter are also expected to be identical. Furthermore, since the oil jets are positioned at the centre of a tooth quarter, the heat transfer induced by the oil jet on both halves of a tooth quarter should also be symmetrical, especially for the central oil jets generated by the second and third nozzles. The required information about heat transfer can be obtained from one-eighth of the gear width by utilising the periodicity over the gear width and the symmetry within the tooth quarter. Additionally, the fundamental processes occurring on each tooth should also be identical. This enables the placement of thermocouples on different teeth, easing the instrumentation.

Twenty-four thermocouples are installed on the surface of the gear teeth. The positioning of the thermocouples on the gear, as well as the oil jets for spraybars J100 and J101, are shown on the left side of Figure 3.3, with the axial coordinate y defined in the opposite direction of the oil flow in the spraybar from 0 mm to the gear width $W = 90$ mm as well as the circumferential coordinate s from 0 mm to the total length across one tooth $L = 23.86$ mm. Eighteen thermocouples are positioned on the same one-eighth of the gear width, between the second and third nozzles in the direction of the oil flow within the spraybar. The remaining six are located on the other half of the same tooth quarter, between the first and second nozzles. These six thermocouples are used by von Plehwe (2022) to check whether the symmetry assumption holds for the measured temperatures. Temperature differences between these so-called reference thermocouples and the corresponding thermocouples on the opposite half of the tooth quarter do not necessarily mean that the heat transfer on both halves is not symmetrical. Preliminary FEA calculations with simple correlations for rotating bodies on the axial faces of the gear have shown that the temperature distributions on both one-eighths between the second and third oil jets are practically identical. In contrast, slight differences are observed when comparing other neighbouring one-eighths. Therefore, the eighteen thermocouples located in the highly symmetrical region are suited for the measurement. The reference thermocouples are neglected in the evaluation.

The image on the right side of Figure 3.3 presents the true-to-area projection of the tooth surface into a two-dimensional surface. The newly generated tooth coordinate system is spanned between $0 \leq s^+ \leq 1$ and $0 \leq y^+ \leq 1$, with $s^+ = s/L$ and $y^+ = y/W$. Figure 3.4 depicts the instrumentation, the paths along which oil jets impinge on the gear, and the symmetry lines between nozzles for

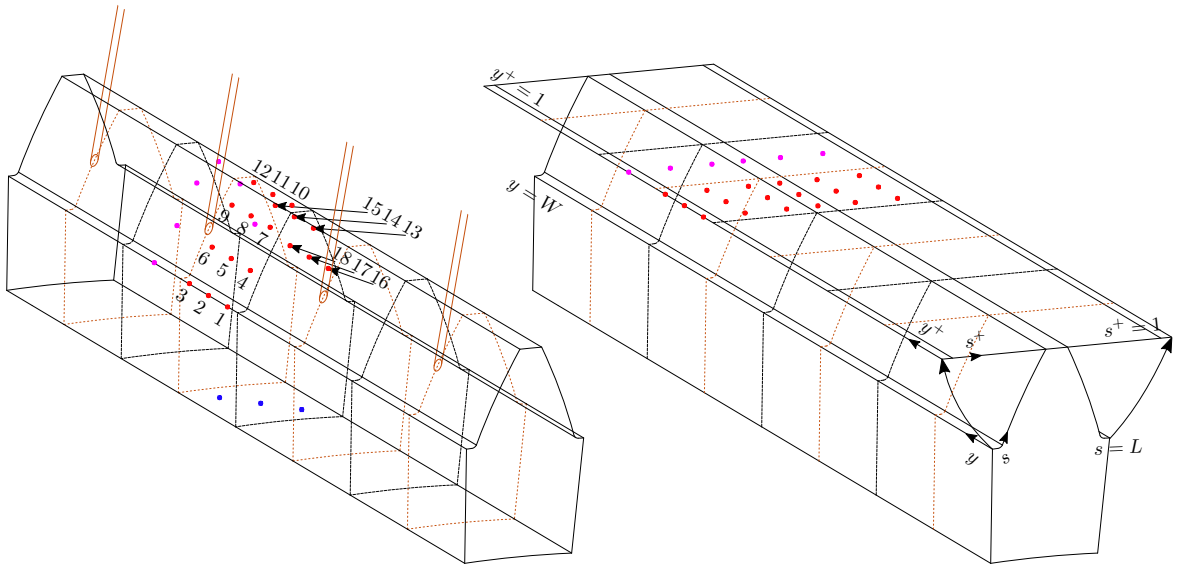

Figure 3.3: The reference thermocouples (magenta), the numbered evaluation thermocouples (red) and the inner surface thermocouples (blue) together with four oil jets on the left-hand side. The transformation into the tooth coordinate system on the right-hand side (Ayan et al., 2022b).

spraybars J100 and J101 on the left and for J102 on the right side. Different parts of the tooth -the bottomland (BL), the active flank (AF), the topland (TL) and the passive flank (PF)- are separated with vertical lines. The positions of the thermocouples used for evaluation are listed in Table 3.3. For J100 and J101, the oil jets impinge along the lines with $y^+ \in \{0.125, 0.375, 0.625, 0.875\}$, which leads to the additional symmetry lines at $y^+ \in \{0.25, 0.5, 0.75\}$. If kept at the same axial position as J100 and J101, spraybar J102 would generate eight oil jets impinging on $y^+ \in \{0.0625, 0.1875, 0.3125, 0.4375, 0.5625, 0.6875, 0.8125, 0.9375\}$. Note that the oil jet along $y^+ = 0.5625$ coincides with one row of thermocouples. This leaves only six thermocouples on either side of the oil jet available for evaluation. In order to keep the measurement resolution as high as possible, the spraybar is moved in the y^+ direction with $\Delta y^+ = 0.0104$ for the measurements with J102. This translative movement results in the symmetry lines depicted on the right side of Figure 3.4, with twelve thermocouples within one-sixteenth of the tooth with $0.5104 \leq y^+ \leq 0.5729$ available for measurement evaluation.

There are three thermocouples in Figure 3.3 that have not been addressed yet. These are positioned on the inner surface of the gear and will be referred to as thermocouples 19, 20 and 21 in the following. The inner surface temperature does not vary as significantly as the tooth surface temperature. Therefore, only three of the available telemetry channels are dedicated to temperature measurements on the inner surface. The measured temperatures are averaged and used as a uniform inner surface temperature T_{in} in the evaluation.

The oil temperature T_{oil} is also required for the evaluation. Von Plehwe et al. (2021) used a type K class 1 thermocouple near the spraybar inlet to measure the oil temperature. The measurements in the initial test matrix of this work utilise this thermocouple. It is replaced by two type T

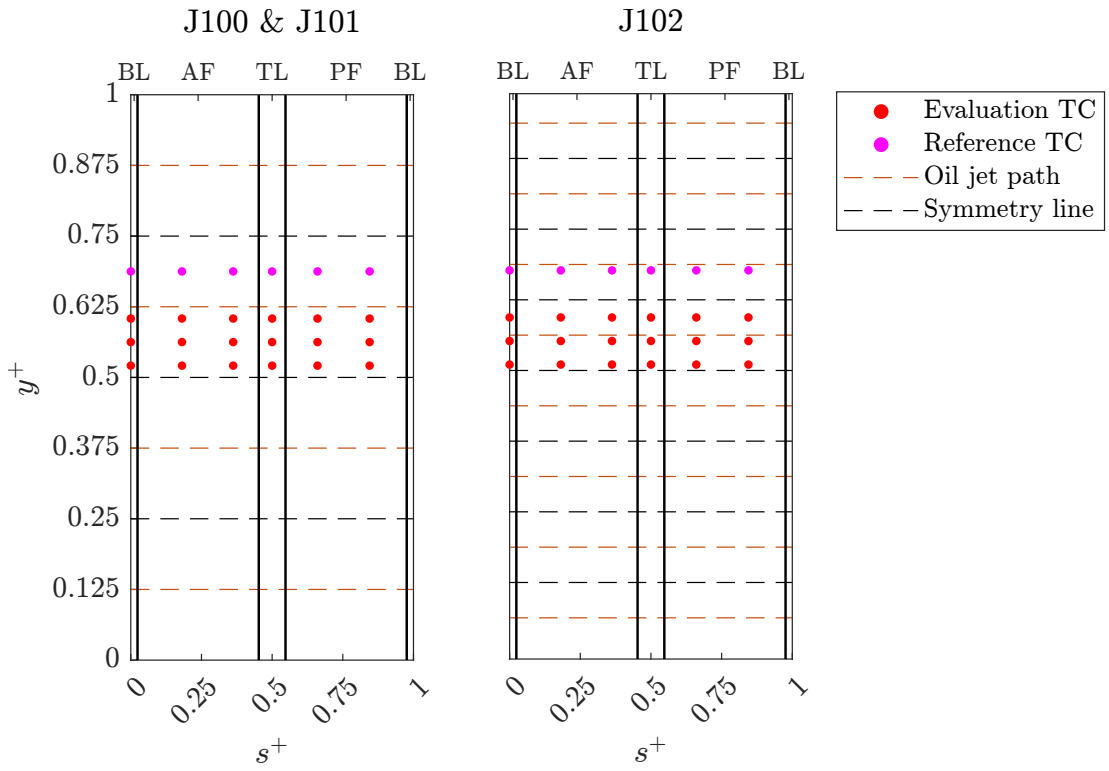

Figure 3.4: Thermocouple, oil jet impingement and symmetry positions for spraybars J100, J101 and J102.

Table 3.3: Positions of the evaluation thermocouples.

TC	s^+	y^+	TC	s^+	y^+	TC	s^+	y^+
1	0	0.5208	7	0.3621	0.5208	13	0.6605	0.5208
2	0	0.5625	8	0.3621	0.5625	14	0.6605	0.5625
3	0	0.6042	9	0.3621	0.6042	15	0.6605	0.6042
4	0.1811	0.5208	10	0.5	0.5208	16	0.8449	0.5208
5	0.1811	0.5625	11	0.5	0.5625	17	0.8449	0.5625
6	0.1811	0.6042	12	0.5	0.6042	18	0.8449	0.6042

class 1 thermocouples with higher accuracy for the measurements in the optimal test matrix (see Chapter 5). One of the type T thermocouples is installed further downstream, between the second and third nozzles, to eliminate a measurement error that could arise from possible losses in the section between the nozzle and the oil temperature thermocouple. No significant difference between the measured temperatures of these type T thermocouples is observed in the experiments. Nevertheless, the thermocouple further downstream is used to measure T_{oil} in the optimal test matrix.

3.3 Evaluation Methodology

The boundary conditions explained in the previous section are summarised in Figure 3.5 for any generic spraybar with four nozzles. This summary also describes the FEA model used in the evaluation. The tooth surface is the only boundary for which the boundary condition is not fully defined yet. The only information acquired from the measurements is the discrete temperature values at the thermocouple positions. The temperature on the rest of the tooth surface is unknown. The trivial approach to complete the missing information is a simple linear interpolation and extrapolation of the temperature data over the tooth surface, utilising symmetry and periodicity conditions. A validation study is conducted by Ayan et al. (2022b) to test this approach. The VOF setup of Keller (2022) for the oil jet gear interaction investigation is modified to account for the heat transfer. Two reference heat transfer coefficient distributions are obtained from the simulations, one with relatively low and another with relatively high heat transfer. FEA calculations are conducted with the reference heat transfer coefficient distributions with typical values for T_{oil} and T_{in}. The FEA simulation delivers a temperature distribution on the tooth surface. Temperature samples are taken from this distribution at the real thermocouple positions. A new temperature distribution is generated by interpolating the sampled temperatures to test the temperature interpolation approach. The interpolated temperature distribution is applied on the tooth surface boundary in the FEA to calculate a heat transfer coefficient distribution, which is then compared to the reference heat transfer coefficient distribution. Figure 3.6 shows the heat transfer coefficient distribution for the high heat transfer case (Case H) calculated with the temperature interpolation approach (TIA) compared to the reference distribution. The so-called heat transfer maps are depicted in the tooth coordinate system for one tooth quarter. The heat transfer coefficient h_{local} depicted in the colour map is normalised via

$$h_{\mathrm{local}} = \frac{h}{\overline{h}_{\mathrm{ref}}}, \tag{3.1}$$

with the surface-averaged heat transfer coefficient of the reference case $\overline{h}_{\mathrm{ref}}$. The heat transfer coefficient h is defined with the difference between the oil temperature T_{oil} and the tooth surface temperature T_{tooth}.

The qualitative visual comparison in Figure 3.6 demonstrates the weaknesses of the TIA. The reference heat transfer coefficient distribution is not reproduced accurately, with especially high deviations at transition points from one part of the tooth to another, e.g. between the active flank and the topland. The subpar performance is not only limited to the local distribution of the heat transfer coefficient but is also apparent in the surface-averaged values. The surface-averaged heat transfer coefficient is 13.5% and 27.1% less than the reference values of the low and high heat transfer cases, respectively. Therefore, this approach is not suitable for measurement evaluation.

Von Plehwe et al. (2021) propose an iterative evaluation methodology to determine the heat transfer coefficient from temperature measurements. The algorithm of this methodology is depicted as a flow chart in Figure 3.7. An initial heat transfer coefficient distribution is required at the beginning. The algorithm converges to the same solution regardless of the initial distribution. However, the time required to reach the convergence is reduced if a convenient initial

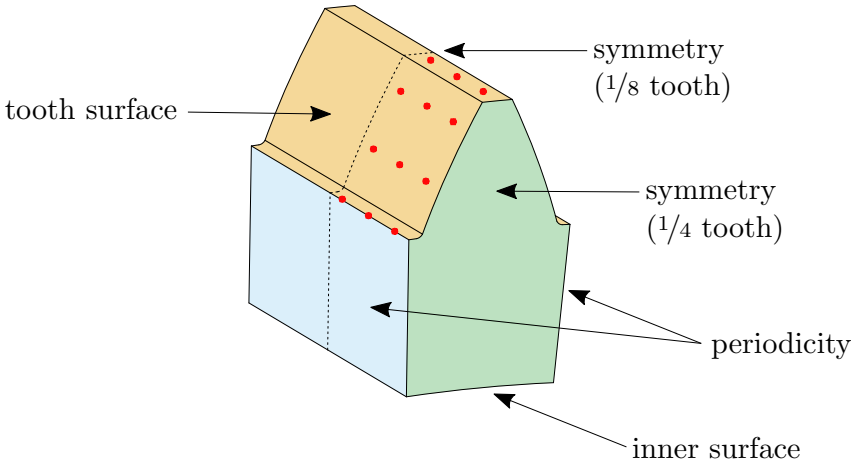

Figure 3.5: The model used for the finite element analysis, specific to spraybars with four nozzles (Ayan et al., 2022b).

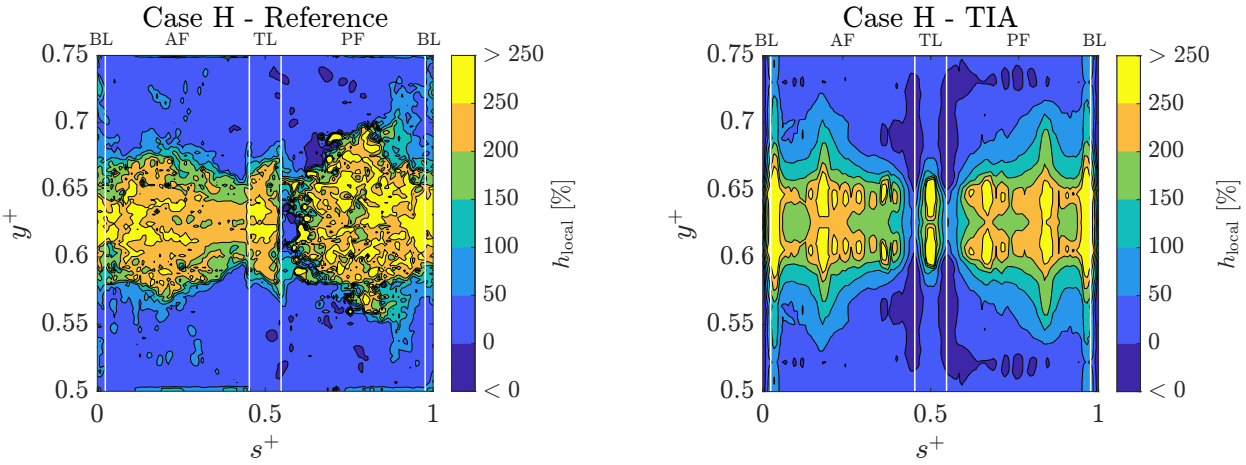

Figure 3.6: The reference heat transfer map and the heat transfer map determined via the temperature interpolation approach for the high heat transfer case (Ayan et al., 2022b).

distribution is chosen. Preliminary studies have shown that an average heat transfer coefficient of 500 W/(m^{2}K) with local variation depending on the measured temperatures leads to excellent convergence times. 500 W/(m^{2}K) is applied as the average value of vector **h**, which contains the individual heat transfer coefficient values at thermocouple positions h_i. The h_i values are adjusted depending on the temperature measured by the corresponding thermocouple by keeping h_i for the thermocouple with the lowest temperature at 0 W/(m^{2}K) and scaling the remaining h_i linearly with the temperature difference between the respective thermocouples and the lowest temperature. The vector **h** is interpolated linearly in the tooth coordinate system to generate the required initial distribution.

The first step in an iteration is the FEA calculation with the latest heat transfer coefficient distribution applied on the tooth surface. The stationary simulation is conducted with the PARDISO solver and the COMSOL Multiphysics® software (COMSOL AB, 2019). One-eighth of a tooth is meshed with 87037 tetrahedra and a maximum element size of 1 mm. In

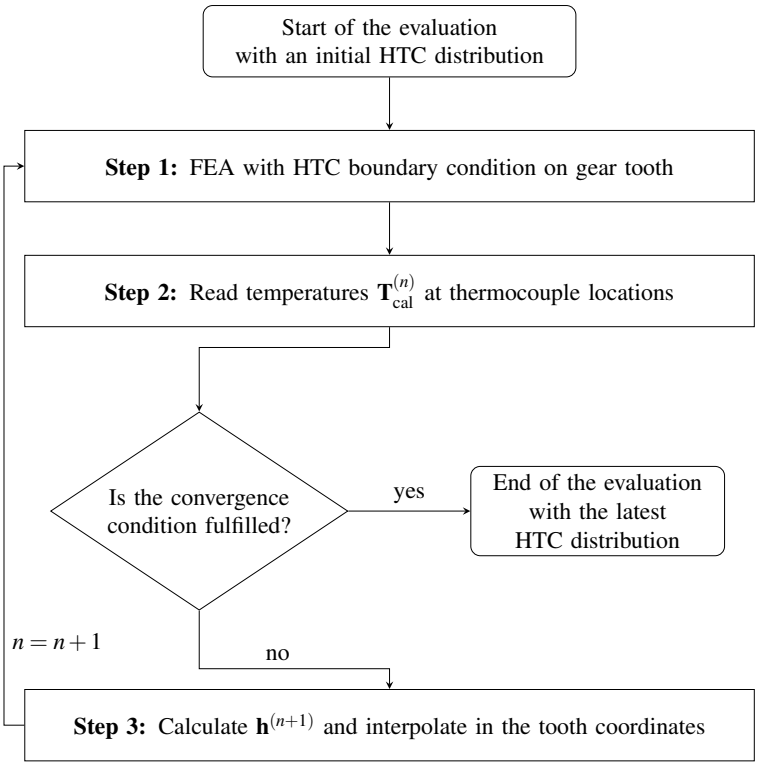

Figure 3.7: Flow diagram of the evaluation algorithm (Ayan et al., 2022b).

Step 2, the temperature values at thermocouple positions $\mathbf{T}_{\text{cal}}^{(n)}$ of the iteration n are sampled from the resulting temperature field. These calculated temperatures are compared to the measured temperatures $\mathbf{T}_{\text{mes}}$ to check the convergence of the solution. Von Plehwe (2022) defines the convergence condition as

$$\max(|\mathbf{T}_{\text{mes}} - \mathbf{T}_{\text{cal}}^{(n)}|) < 0.25 \text{ K}. \tag{3.2}$$

Improvements in the evaluation code allowed the realisation of a much stricter convergence condition with the square error

$$S^{(n)} = (\mathbf{T}_{\text{mes}} - \mathbf{T}_{\text{cal}}^{(n)})^{\text{T}}(\mathbf{T}_{\text{mes}} - \mathbf{T}_{\text{cal}}^{(n)}) < 0.0018 \text{ K}^2, \tag{3.3}$$

interpretable as a mean error of 0.01 K per thermocouple. The evaluation is finished if the defined convergence condition is fulfilled. The latest heat transfer coefficient distribution is determined as the solution to the heat transfer problem. The estimated distribution with $\mathbf{h}^{(n)}$ has to be improved if the convergence condition is not fulfilled. Von Plehwe (2022) utilises the function

$$\mathbf{h}^{(n+1)} = \mathbf{h}^{(n)} + \frac{\overline{\mathbf{h}}^{(n)}(\mathbf{T}_{\text{mes}} - \mathbf{T}_{\text{cal}}^{(n)})}{T_{\text{oil}} - \overline{\mathbf{T}}_{\text{cal}}^{(n)}}. \tag{3.4}$$

in Step 3 to calculate $\mathbf{h}^{(n+1)}$ for the next iteration based on the average values of $\mathbf{h}^{(n)}$ and $\mathbf{T}_{\text{cal}}^{(n)}$. Ayan et al. (2022b) propose an alternative for this calculation based on the Levenberg-Marquardt algorithm. This method splits Step 3 into three sub-steps. First, the Jacobian matrix $\boldsymbol{J}^{(n)}$ and

the diagonal matrix $\boldsymbol{\Omega}^{(n)}$ are calculated with

$$\boldsymbol{J}^{(n)} = (\nabla \mathbf{T}_{\mathrm{cal}}^{(n)}(\mathbf{h}^{(n)}))^{\mathrm{T}} \tag{3.5}$$

$$\boldsymbol{\Omega}^{(n)} = \mathrm{diag}[(\boldsymbol{J}^{(n)})^{\mathrm{T}}\boldsymbol{J}^{(n)}]. \tag{3.6}$$

Then, the linear system of equations

$$[(\boldsymbol{J}^{(n)})^{\mathrm{T}}\boldsymbol{J}^{(n)} + \mu^{(n)}\boldsymbol{\Omega}^{(n)}]\Delta\mathbf{h}^{(n)} = (\boldsymbol{J}^{(n)})^{\mathrm{T}}(\mathbf{T}_{\mathrm{mes}} - \mathbf{T}_{\mathrm{cal}}^{(n)}), \tag{3.7}$$

is solved for $\Delta\mathbf{h}^{(n)}$. The damping factor $\mu^{(n)}$ is set to $\mu^{(0)} = 1$ at the beginning of the evaluation. Afterwards, the heat transfer coefficient distribution of the next iteration is computed with

$$\mathbf{h}^{(n+1)} = \mathbf{h}^{(n)} + \Delta\mathbf{h}^{(n)}. \tag{3.8}$$

In the next iteration, Steps 1 and 2 are carried out as usual with $\mathbf{h}^{(n+1)}$. The Levenberg-Marquardt method (LMM) introduces an acceptance criterion

$$S^{(n+1)} < S^{(n)} \tag{3.9}$$

before Step 3. This criterion checks whether the new estimation of $\mathbf{h}^{(n+1)}$ performs better than the previous estimation of $\mathbf{h}^{(n)}$. If the performance is improved, the iteration with $\mathbf{h}^{(n+1)}$ is accepted. The damping factor μ in Equation 3.7 is reduced for iteration $n + 1$ with

$$\mu^{(n+1)} = 0.1\mu^{(n)}. \tag{3.10}$$

The calculations in Step 3 are carried out with the new damping factor to determine $\mathbf{h}^{(n+2)}$ for the next iteration. If the acceptance criterion is not fulfilled, the algorithm reverts to Step 3 of iteration n with an increased damping factor

$$\mu^{(n)} = 10\mu_{\mathrm{rej}}, \tag{3.11}$$

where μ_{rej} is the damping factor of the rejected iteration.

One major challenge of the LMM is calculating the Jacobian matrix $\boldsymbol{J}$ in Equation 3.5. The heat transfer problem is too complex to determine the individual differential equations of $\partial T_{\mathrm{i}}/\partial h_{\mathrm{j}}$. An approximate $\boldsymbol{J}$ is calculated utilising a simplified heat transfer model, where the convection between the oil and the gear as well as the conduction within the gear are modelled in a three-dimensional grid with three layers in the radial direction (Figure 3.8). Each layer consists of 18 nodes, one for each thermocouple. The nodes in the outer layer have two attributes: the constant oil temperature T_{oil} and the heat transfer coefficient at the thermocouple position h_{i}. The nodes in the middle layer imitate the thermocouples themselves and have the calculated temperature $T_{\mathrm{cal,i}}$. This layer is created in the tooth coordinate system with the actual distances between each thermocouple. The distance to the inner surface is reproduced in the inner layer, where the nodes are placed at a distance specific to each thermocouple. These nodes have a uniform inner surface temperature T_{in}. The simple model has three components of heat transfer for each

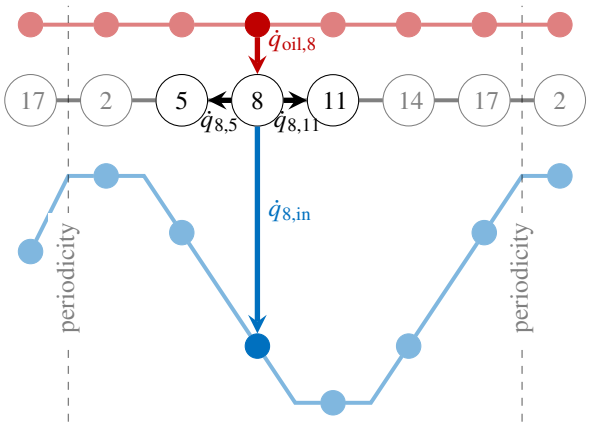

Figure 3.8: Simplified heat transfer model from radial view with heat fluxes for thermocouple 8 (Ayan et al., 2022b).

thermocouple i: the convective heat flux $\dot{q}_{\mathrm{oil,i}}$, the conductive heat flux $\dot{q}_{\mathrm{i,j}}$ to or from its four direct neighbours j, and the conductive heat flux into the inner layer $\dot{q}_{\mathrm{i,in}}$. For the stationary solution, each thermocouple has to demonstrate an equilibrium of

$$\underbrace{h_{\mathrm{i}}(T_{\mathrm{oil}} - T_{\mathrm{cal,i}})}_{\dot{q}_{\mathrm{oil,i}}} = \sum_{\mathrm{j}} \underbrace{\frac{\lambda(T_{\mathrm{cal,i}} - T_{\mathrm{cal,j}})}{d_{\mathrm{ji}}}}_{\dot{q}_{\mathrm{i,j}}} + \underbrace{\frac{\lambda(T_{\mathrm{cal,i}} - T_{\mathrm{in}})}{l_{\mathrm{i}}}}_{\dot{q}_{\mathrm{i,in}}}, \tag{3.12}$$

with the thermal conductivity of the gear λ, the distance d_{ji} between thermocouple i and its direct neighbour j, and the radial distance l_{i} between i and the inner surface. The resulting equation system can be solved analytically. The case-specific constants (T_{oil}, T_{in}) and the variables (**h** and **T**) can be substituted into the analytical solution in each iteration to determine the numerical values of $\boldsymbol{J}^{(n)}$.

The aforementioned validation study of Ayan et al. (2022b) also investigates the validity of the iterative evaluation methods. The von Plehwe Method (VPM) and the LMM reproduce the reference heat transfer coefficient distributions with very high accuracy. The heat transfer maps are depicted in Figure 3.9. The iterative methods result in practically identical heat transfer coefficient distributions. Both heat transfer maps demonstrate the same qualitative distribution of the heat transfer coefficient as the reference map, albeit at a lower resolution because of the limited number of discrete temperature measurement positions. The surface-averaged heat transfer coefficients are also in very good agreement with the reference cases. Both methods resulted in $\overline{h}$ values that are only 1.8% and 6% lower than the reference values of high and low heat transfer cases, respectively. Ayan et al. (2022b) also show that a substantial part of these deviations can be attributed to the asymmetrical heat transfer coefficient distribution of the reference cases. The iterative methods result in $\overline{h}$ values that are off by less than 0.8% if the neighbouring one-eighth of the tooth is also instrumented with thermocouples. This keeps the spatial resolution of the measurement constant while eliminating the need for the symmetry assumption in the middle of the tooth quarter. The measured temperatures are time-

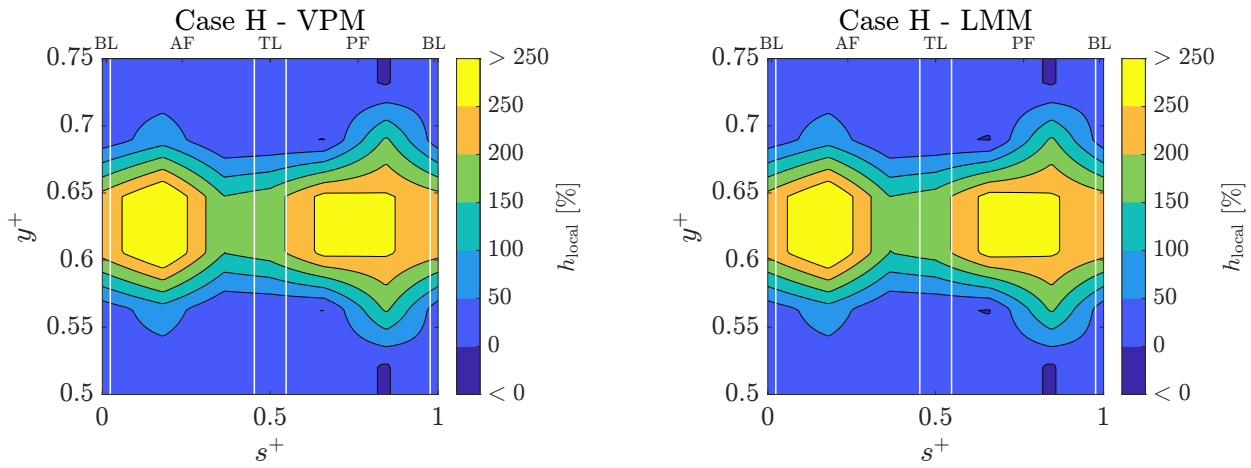

Figure 3.9: The heat transfer maps of the high heat transfer case determined via the von Plehwe and Levenberg-Marquardt Methods (Ayan et al., 2022b).

averaged results of multiple thousand impingements in contrast to the single impingement in the CFD simulation used as a reference here. Therefore, the symmetry assumption utilised in the evaluation would not lead to a lower accuracy in the measurements, as is the case in this comparison. The exceptional accuracy of less than 0.8% deviation showcases the capabilities of the evaluation methodology despite the relatively low spatial resolution of the measurements. Ayan et al. (2022b) also show that the LMM can reach the converged solution nearly twice as fast as the VPM. Therefore, the LMM is used to evaluate the measurements conducted in this work.

3.4 Calibration

The experimental methodology is based on temperature measurements taken by thermocouples on the gear. The voltage difference between both ends of a thermocouple is not directly acquired. These ends are soldered on the printed circuit board of the telemetry unit. The measured voltage signal is converted to a digital signal and transmitted wirelessly to the receiver unit. The digital signal acquired by the measurement computer is converted back to a voltage signal utilising the calibration curve supplied by the manufacturer

$$U/\mu\mathrm{V} = aD_{\mathrm{out}} + b, \tag{3.13}$$

with the voltage U, the digital output D_{out}, the calibration gain a and the calibration offset b. The voltage is then used to calculate the temperature at the measurement position utilising the cold junction temperature, which is acquired by the PT100 thermistor located on the printed circuit board of the telemetry unit. The calculation follows the DIN EN 60584-1 norm (DIN e.V., 2014). However, this procedure leads to some inexplicable temperature differences between the thermocouples and the PT100 thermistor. Figure 3.10a shows temperature readings by the spraybar thermocouple (SB), the gear thermocouples (TC) and the PT100 thermistor as the cold junction (CJ) at the beginning of a measurement day before the rotation and oil feed are

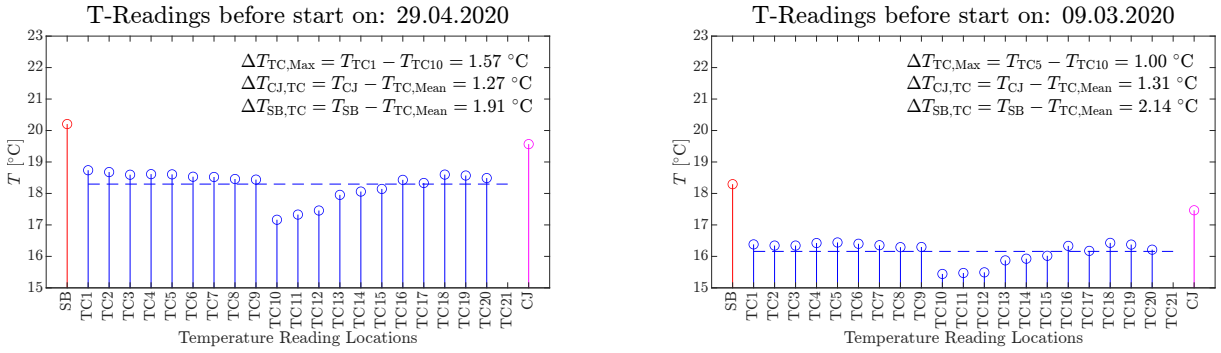

(a) (b)

Figure 3.10: Temperature readings at the cold state on a measurement day (a) and after keeping the instrumented gear, the telemetry unit and the spraybar thermocouple in an insulated box for three days (b).

switched on, from now on referred to as the cold state. The dashed blue line is the mean temperature measured by the working thermocouples on the gear[1]. The maximum temperature difference between two gear thermocouples ($\Delta T_{TC,Max}$), the temperature difference between the PT100 thermistor and the mean of gear thermocouples ($\Delta T_{CJ,TC}$), and the temperature difference between the spraybar thermocouple and the mean of gear thermocouples ($\Delta T_{SB,TC}$) are given on the upper right side of the figure. These temperature differences are greater than the expected accuracy of a type K thermocouple. Errors in the same order are measured, even after the spraybar thermocouple, the instrumented gear and the telemetry unit are kept in an insulated box for three days (Figure 3.10b). The similar differences between gear thermocouples in both measurements imply a systematic error specific to each thermocouple.

One way to correct the systematic errors is to define an offset voltage for each thermocouple so that the same temperature as the PT100 thermistor is measured in the cold state. This effectively means that the offset b in Equation 3.13 is redefined for each thermocouple. The correction is applied for all measurements in the so-called initial test matrix (see Chapter 5), including those conducted by von Plehwe (2022). If data is available, the new offsets are acquired in the cold state of a measurement day. If not, the most recent offsets are used for the correction. A critical shortcoming of this approach is the assumption that the gain a is the same for each thermocouple as initially determined by the telemetry manufacturer. A calibration scheme is utilised to test this assumption and define individual calibration curves for each thermocouple. The calibration setup involves a temperature-controlled oil bath filled with silicon oil KORASILON M7. The oil is kept recirculating within the oil bath to make the temperature distribution as uniform as possible. The gear is partly submerged in the oil, as depicted in Figure 3.11. The gear thermocouples are symbolically shown with black dots. The gear is mounted on the rotatable spool with the telemetry unit and its receiver set up as usual. Only some of the thermocouples are submerged in the oil bath at any given position of the gear. The dashed line in Figure 3.11 is drawn vertically at the lowest point of the pitch circle. The preliminary results have shown that the temperature measured by a thermocouple does not change if the gear is rotated up to

[1]The thermocouple TC21 is excluded in this case since it was defective during these measurements.

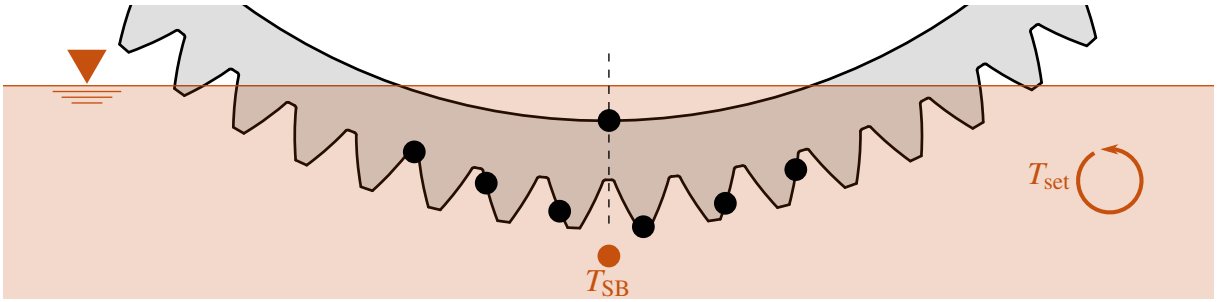

Figure 3.11: Calibration setup with the recirculating heated oil bath and the instrumented gear.

an angle equivalent to three teeth in either direction. Therefore, thermocouples installed on the three teeth on each side of the dashed line and thermocouples on the inner surface within an angle equivalent to one tooth from the dashed line are assumed to be at the oil temperature. In order to ensure that enough data is available for each thermocouple, seven rotational positions of the gear are required for each oil bath temperature. The gear is kept at each position until the measured signals are stationary for the designated thermocouples. The digital output is recorded over 30 seconds. After that, the gear is rotated to the next position. The set oil bath temperature is varied between 35 °C $\leq T_{set} \leq$ 70 °C with steps of 5 °C. The oil temperature in the vicinity of the gear is measured with a type T thermocouple (T_{SB}), depicted as an orange dot in Figure 3.11. This is the same thermocouple installed in the spraybar to measure the oil temperature during measurements in the optimal test matrix. The measured oil temperature is used for the calibration and varies slightly from the oil temperature set for the heater unit T_{set}.

The resulting data points for one of the thermocouples, TC9, are shown in Figure 3.12, together with the new and original calibration curves. The voltage $U_{req,TC9}$ on the y-axis is the voltage required to measure T_{SB} with the measured cold junction temperature T_{CJ}, determined following the DIN EN 60584-1 norm (DIN e.V., 2014). The digital output $D_{out,TC9}$ of the telemetry unit is given on the x-axis. The new calibration curve is generated analogously to Equation 3.13 with new gain and offset values specific to this thermocouple. The new gain and offset values for all thermocouples are depicted in Figure 3.13, together with the original gain and offset values, a_{org} and b_{org}. The highest difference between the new and original gain values is $\Delta a_{max} = 0.01$. If an extreme case with a temperature difference of $T_{TC} - T_{CJ} = 35$ K is considered, this deviation will result in a measurement error of 1.2 K. The error originating from the difference in offset values has a more significant effect. The highest deviation from the original offset value is $\Delta b_{max} = 107.06$. The voltage difference of 107.06 μV would be present over the whole temperature range, leading to temperature errors up to 3 K. This means that most errors are corrected via the simple offset correlation conducted for the measurements in the initial test matrix. Nevertheless, the newly determined and more accurate calibration curves are applied to the optimal test matrix measurements.

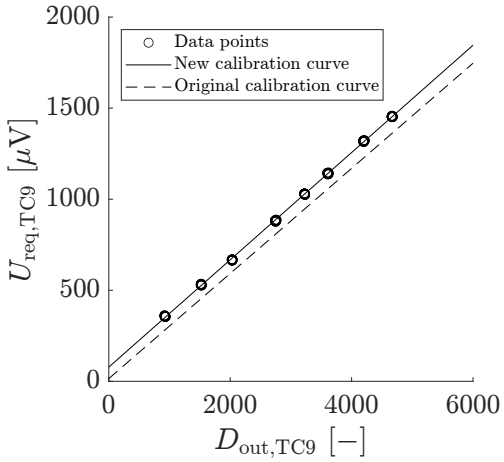

Figure 3.12: Required voltage U_{req} for T_{SB} over the digital output D_{out} for thermocouple TC9, together with the new and original calibration curves.

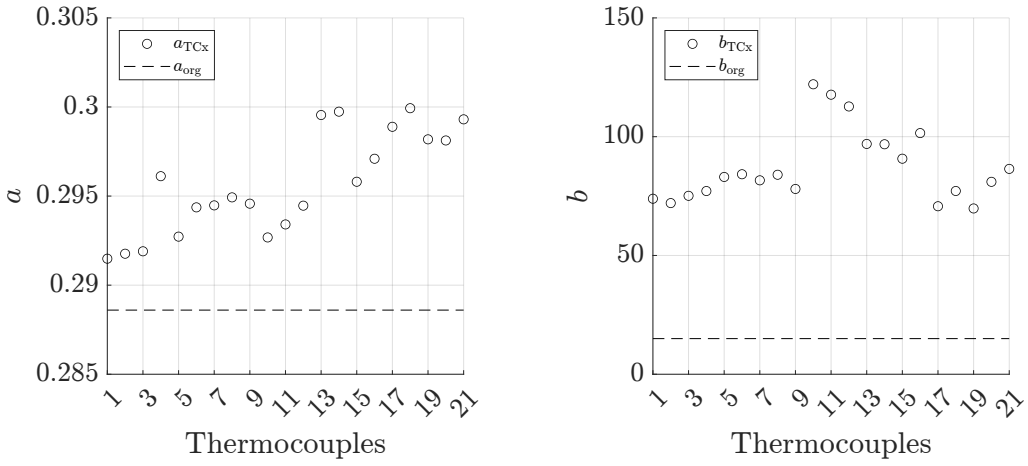

(a) (b)

Figure 3.13: The new gain (a) and offset (b) values acquired via calibration compared to the original values.

4 Oil Jet Flow Investigation

It has long been established that the impingement depth of the oil jet plays a significant role in heat transfer. Determining the impingement depth requires solving an analytical model with a known jet velocity. As von Plehwe (2022) states, two flow regimes are observed during the experiments. Understanding each flow regime is essential since the velocity of an attached jet differs from that of a separated one. The nozzle flow is therefore investigated experimentally and numerically. The findings are then applied to the results of von Plehwe (2022) to study their consistency and applicability.

4.1 Experimental Investigation of the Oil Jet

The first step in investigating the oil jet flow is classifying and characterising the flow regimes. A visual investigation is conducted with the spraybar J100, which has four nozzles of type N115 with $d_\mathrm{n} = 1.15$ mm. The goal is to capture the oil jet flow and its change depending on the applied pressure difference $\Delta p = p_\mathrm{up} - p_\mathrm{exit}$, with the constant exit pressure $p_\mathrm{exit} = p_\mathrm{ambient}$ and the upstream pressure p_up. Three nozzles are blanked to capture clear images of a singular jet. The oil temperature measured in the spraybar is kept within the range of $T_\mathrm{oil} = 80 \pm 2°\mathrm{C}$. The oil jets at pressure differences of 1 bar, 1.9 bar, 2.7 bar, 3.3 bar and 17 bar are shown in Figures 4.1, 4.2, 4.3, 4.4 and 4.5, respectively. Ten images are captured within one-third of a second for each pressure difference. At low pressure differences, a visually laminar and stable oil jet is observed, as depicted in Figure 4.1, with a pressure difference of $\Delta p = 1$ bar and a volume flow rate of $\dot{V}_\mathrm{nozzle} = 0.55\,\mathrm{l/min}$. Increasing the upstream pressure leads to instabilities within the oil jet. These lead to the turbulent jet shown in 4.2 with $\Delta p = 1.9$ bar and $\dot{V}_\mathrm{nozzle} = 0.8\,\mathrm{l/min}$. The instabilities amplify with increasing pressure difference, leading to the highly disturbed jet in 4.3 with $\Delta p = 2.7$ bar and $\dot{V}_\mathrm{nozzle} = 1\,\mathrm{l/min}$. A further pressure increase triggers the transition from a highly disturbed jet to a more stable one, as shown in Figure 4.4. The volume flow rate drops spontaneously to $\dot{V}_\mathrm{nozzle} = 0.97\,\mathrm{l/min}$ despite the greater pressure difference of $\Delta p = 3.3$ bar. At this point, the jet visually differs from the laminar jet with a low pressure difference (Figure 4.1). However, the surface disturbances are not as substantial as in the jet before the transition. The oil jet structure remains similar up to the greatest applied pressure difference, $\Delta p = 17$ bar, whereas the droplet formation intensifies with increasing pressure difference. The accumulated droplet splashing on the front glass leads to the blurred image depicted in Figure 4.5 with $\Delta p = 17$ bar and $\dot{V}_\mathrm{nozzle} = 2.2\,\mathrm{l/min}$. The same regimes are also observed for the other nozzle geometry N082 with $d_\mathrm{n} = 0.82$ mm, albeit with transition at different pressure differences.

The change in volume flow rate over the measured pressure range is depicted in Figure 4.6a. The volume flow rate increases continuously for both nozzle geometries until the transition point Δp_crit is reached. Here, a sudden drop occurs in the flow rate, whereafter, a continuous increase is observed within the pressure range. The continuous behaviours before and after the transition and the visual observations suggest a singular event in the nozzle after reaching a certain threshold. A similar phenomenon is reported in the literature for cavitating nozzle flows by Hiroyasu et al. (1991), who investigated a cavitating flow in a transparent nozzle. Hiroyasu

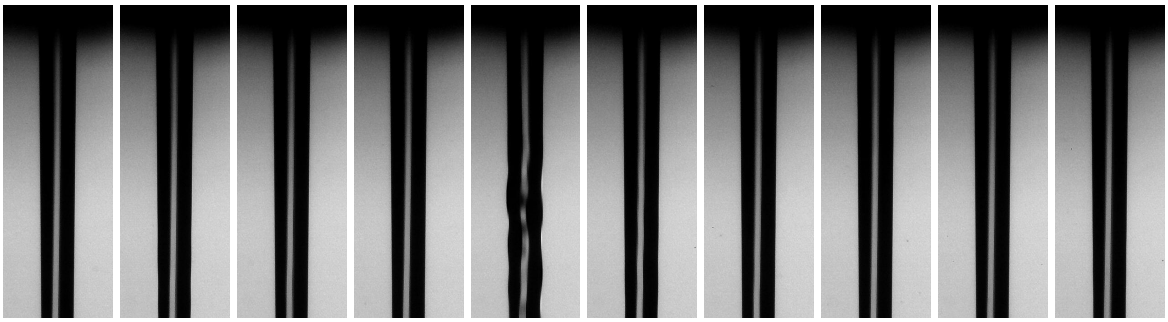

Figure 4.1: Oil jet with $\Delta p = 1$ bar and $\dot{V}_{\text{nozzle}} = 0.55$ l/min.

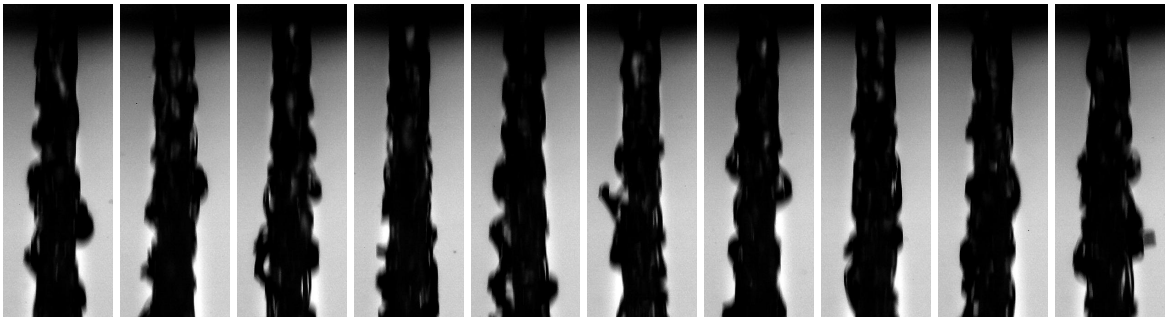

Figure 4.2: Oil jet with $\Delta p = 1.9$ bar and $\dot{V}_{\text{nozzle}} = 0.8$ l/min.

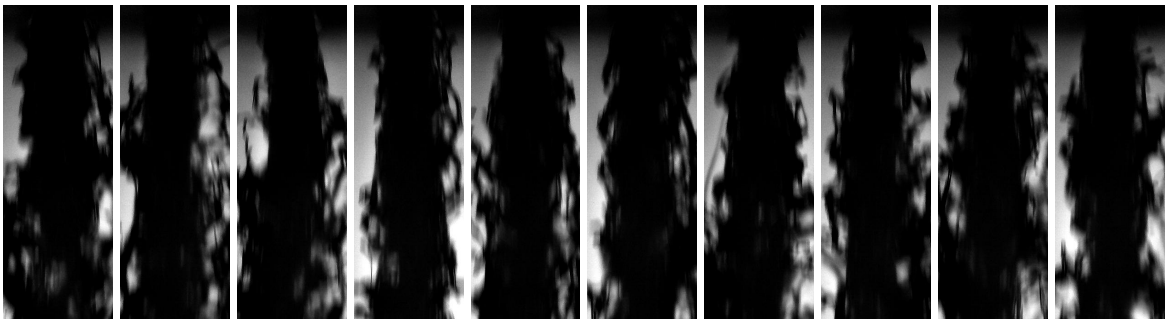

Figure 4.3: Oil jet with $\Delta p = 2.7$ bar and $\dot{V}_{\text{nozzle}} = 1$ l/min.

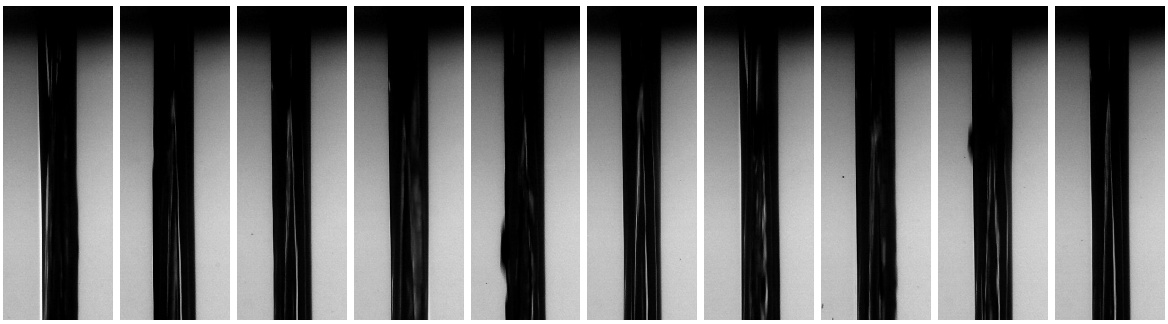

Figure 4.4: Oil jet with $\Delta p = 3.3$ bar and $\dot{V}_{\text{nozzle}} = 0.97$ l/min.

et al. (1991) observed strong turbulence after the initial onset of cavitation at the nozzle inlet. This turbulence led to increased surface disturbances and decreased break-up length of the jet. A further increase in jet velocity caused the cavitation zone to reach the nozzle exit, separating the

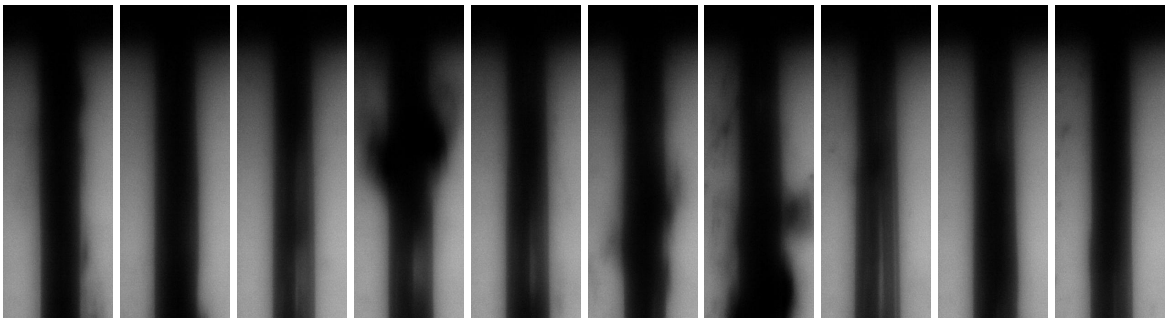

Figure 4.5: Oil jet with $\Delta p = 17$ bar and $\dot{V}_{\text{nozzle}} = 2.2\,\text{l/min}$.

jet from the nozzle walls. The separation decreased the turbulence, and the jet became visually smooth. The nozzle with this so-called super cavitation or hydraulic flip behaved like an orifice.

In an orifice, the contraction coefficient

$$C_{\text{c}} = \frac{d_{\text{jet}}^2}{d_{\text{n}}^2} \tag{4.1}$$

can be approximated by the discharge coefficient

$$C_{\text{d}} = \frac{\dot{V}_{\text{nozzle}}}{\frac{\pi d_{\text{n}}^2}{4}\sqrt{\frac{2\Delta p}{\rho}}}, \tag{4.2}$$

which is the ratio of the real volume flow rate to the ideal volume flow rate with the applied pressure difference over the nozzle (Lienhard, 1984). Abderrezzak and Huang (2017) argue that the relation $C_{\text{c}} = C_{\text{d}}$ is also valid for a nozzle with hydraulic flip. Neither Hiroyasu et al. (1991) nor Abderrezzak and Huang (2017) elaborate on the variation of the discharge coefficient after the onset of hydraulic flip. Yokota et al. (1988) investigated the flow through a cavitating nozzle, albeit with a confined jet. The discharge coefficient they report and its dependency on the cavitation number

$$\sigma = \frac{p_{\text{exit}} - p_{\text{v}}}{\Delta p} \approx \frac{p_{\text{exit}}}{\Delta p}, \tag{4.3}$$

with the vapour pressure $p_{\text{v}} \ll p_{\text{exit}}$, is in very good agreement with the measurements conducted for this work (see Figure 4.7), supporting the hydraulic flip hypothesis for the observed phenomenon. Both results show an increase in discharge coefficient for decreasing cavitation number until a critical cavitation number σ_{crit} is reached. Even though σ_{crit} differs for both studies, the discharge coefficient declines for $\sigma < \sigma_{\text{crit}}$ and remains constant in both cases with $\lim_{\sigma \to 0} C_{\text{d}} \approx 0.6$. The sudden decrease in C_{d} coincides with the transition point observed in $\dot{V}_{\text{nozzle}}$, as can be deduced by comparing Figures 4.6a and 4.6b. Similar observations are also reported in the literature for free surface jets (Cordes, 2021; He et al., 2016, 2015).

Hydraulic flip is inferred to be a suitable explanation for the observed flow regimes. The onset of hydraulic flip changes the geometry of the oil jet by separating it from the nozzle walls. The separated flow is analogous to an orifice flow with $C_{\text{c}} = C_{\text{d}} = 0.6$. The effective jet diameter of

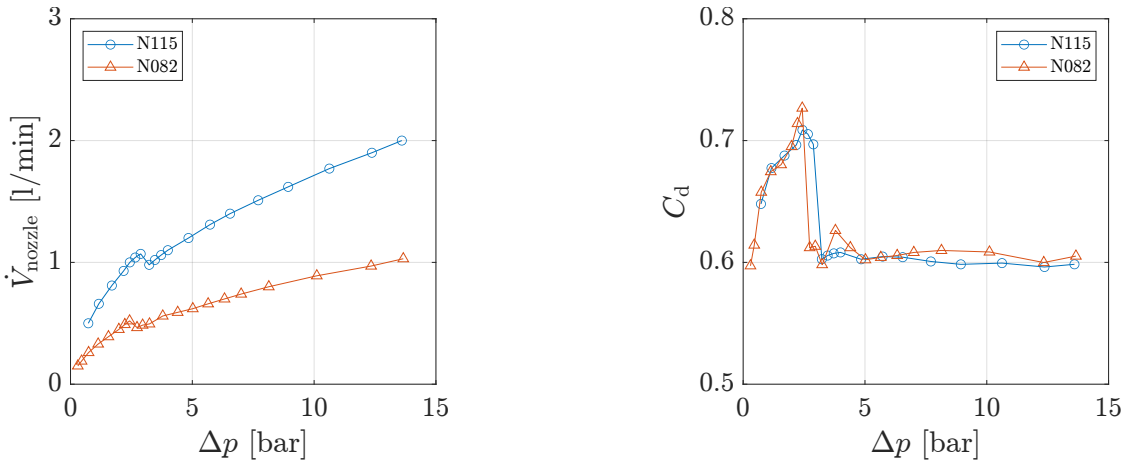

(a) (b)

Figure 4.6: Change of volume flow rate (a) and discharge coefficient (b) with the pressure difference.

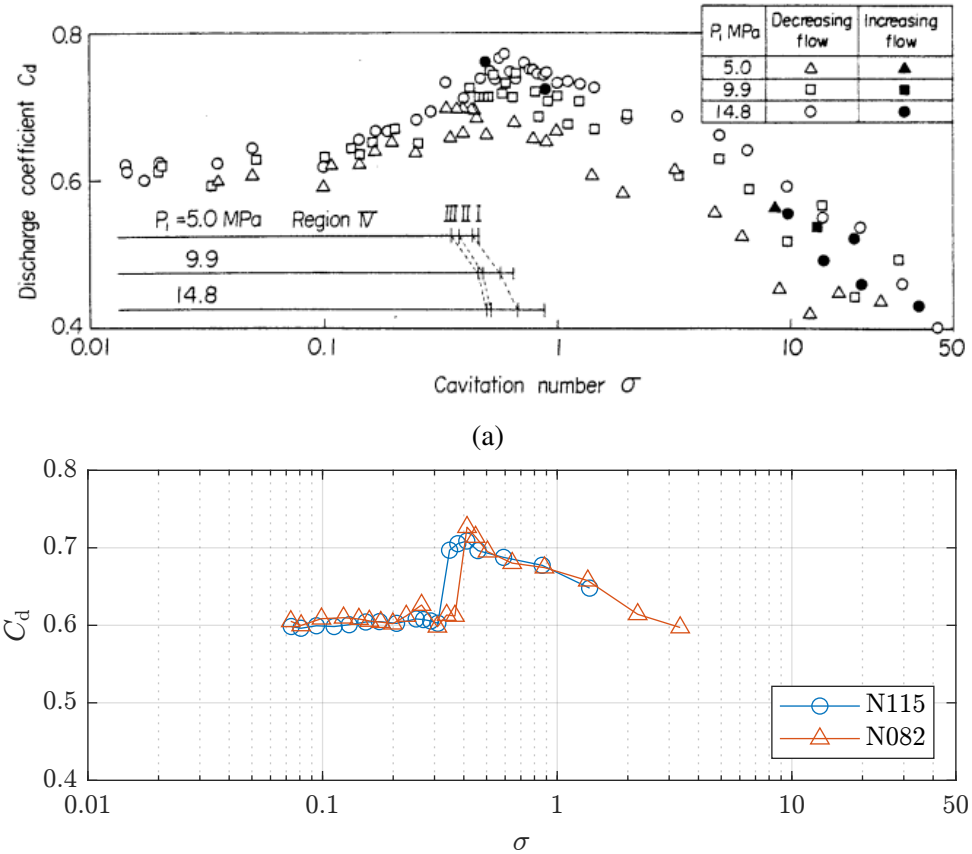

(a)

(b)

Figure 4.7: Discharge coefficient and the cavitation number reported by Yokota et al. (1988) (a) and measured in this work (b).

an operating point is defined as

$$d_{\mathrm{jet}} = \begin{cases} d_{\mathrm{n}}, & \text{if } \Delta p < \Delta p_{\mathrm{crit}}. \\ \sqrt{0.6}\, d_{\mathrm{n}}, & \text{otherwise.} \end{cases} \tag{4.4}$$

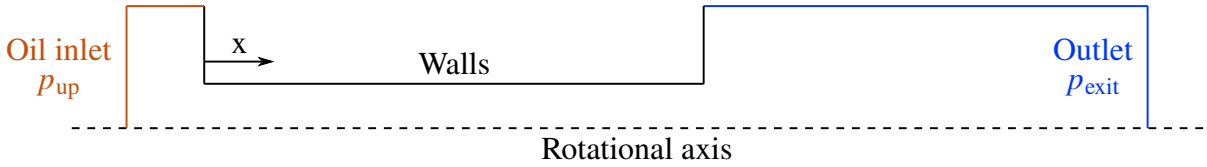

Figure 4.8: The axisymmetric numerical setup with the oil inlet on the left in orange,the outlet on the right in blue, the no-slip walls with solid black lines and rotational axis with dashed black line.

4.2 Numerical Investigation of the Oil Jet

A numerical study with a simplified model is conducted to simulate the separation of a free jet in case of a cavitating nozzle flow in order to ascertain whether the observed nozzle characteristics can be explained by the hydraulic flip hypothesis. Three materials are defined for the multiphase modelling via VOF. The first phase is the liquid oil phase, with material properties of Mobil Jet Oil II at a temperature of 80 °C. The second phase is the oil vapour, which is formed if the liquid pressure falls below the vapour pressure of the oil. The vapour pressure and other properties of Mobil Jet Oil II vapour are not publicly available. However, the liquid *"fuel-oil-liquid"* in the materials database of ANSYS (2019) exhibits properties similar to those of Mobil Jet Oil II, and the same database contains an entry for *"fuel-oil-vapour"*. This material was selected for the oil vapour as it is the closest available candidate. The third phase is air, as defined in the materials database of ANSYS (2019). The multiphase model is based on the implicit formulation with an interface modelling of dispersed type. The cavitation process is modelled using the Schnerr-Sauer model with the default bubble number density of 10^{11}. The flow is modelled as an isothermal, axisymmetric, transient and laminar flow without compressibility. Gravitational forces are considered in the same direction as in the experiments, denoted with x in the following.

Two setups are generated for the simulations with the lengths and diameters of the experimental nozzles. The inlet boundary, depicted in orange in Figure 4.8, is defined as a pressure inlet with the set pressure p_{up} and liquid oil flow. Analogously, the outlet boundary, depicted in blue in Figure 4.8, is defined as a pressure outlet with the back pressure of $p_{exit} = 1$ bar. Only the air phase is allowed to flow back in over the outlet. The nozzle walls are no-slip walls.

The inlet pressure is varied in the simulations with $\Delta p \in \{2, 2.5, 3, 3.5, 4, 6, 8, 12\}$ bar. The individual simulations are initialised at $t = 0$ with the converged solution of a stationary simulation where $\Delta p = 2$ bar and no cavitation is observed. The simulations are carried out with the pressure-based solver of ANSYS Fluent and the Coupled pressure-velocity coupling scheme. The option for volume fractions is activated. The variable time step size is adjusted at each time step for a global Courant number of 5. The discretisation schemes are given in Table 4.1.

The simulations successfully reproduce the hydraulic flip phenomenon in the nozzles. The change of internal nozzle flow over time is shown in Figure 4.9 for the N115 case with $\Delta p = 12$ bar. Already at $t = 6.7 \cdot 10^{-4}$ s, the oil vapour extends out to the nozzle exit (Fig-

Table 4.1: The discretisation schemes of the numerical setup.

Variable	Discretisation Scheme
Pressure	PRESTO!
Momentum	Second Order Upwind
Volume Fraction	Second Order Upwind
Energy	Second Order Upwind
Transient Formulation	First Order Implicit

ure 4.9a). Then, the surrounding air starts flowing back into the nozzle, displacing the oil and oil vapour phases (Figure 4.9b, 4.9c, 4.9d and 4.9e). No cavitation occurs after the air phase reaches the nozzle inlet and separates the oil flow from the nozzle walls (Figure 4.9f). The nozzle flow remains stationary after the completion of the hydraulic flip.

The change of volume flow rate $\dot{V}_{\mathrm{nozzle}}$ with the pressure difference Δp is depicted in Figure 4.10a for both the experimental and numerical cases. The simulations reproduce the same transition, albeit at a slightly different pressure difference for N082. The discharge characteristics display a very good agreement with the experiments in both flow regimes (Figure 4.10b). The discharge coefficient C_{d} increases with increasing Δp before the transition point, at which a sudden drop in C_{d} occurs. Further increase in Δp results in a slight decrease of C_{d}, changing from $C_{\mathrm{d}} = 0.62$ at $\Delta p = 4$ bar to $C_{\mathrm{d}} = 0.61$ at $\Delta p = 12$ bar for the nozzle N115. C_{c} is also obtained from the simulations, calculated as the ratio of the oil jet cross-section to the nozzle cross-section. Figure 4.11 shows the ratio $C_{\mathrm{d}}/C_{\mathrm{c}}$ in numerical results. The ratio is $C_{\mathrm{d}}/C_{\mathrm{c}} \approx 0.95$ for both nozzles at $\Delta p > \Delta p_{\mathrm{crit}}$. This ratio supports the assumption $C_{\mathrm{c}} = C_{\mathrm{d}}$, which will be used in the following.

4.3 Applying the Jet Contraction to the Results of von Plehwe

Von Plehwe (2022) presents a complex correlation between the surface-averaged normalised Nusselt number $\overline{\mathrm{Nu}^*}$, the nozzle Reynolds number $\mathrm{Re}_{\mathrm{nozzle}}$ and the gear Reynolds number Re_ω. The nozzle Reynolds number is defined as

$$\mathrm{Re}_{\mathrm{nozzle}} = \frac{u_{\mathrm{jet,ideal}} d_{\mathrm{n}}}{\nu}, \tag{4.5}$$

with the ideal jet velocity $u_{\mathrm{jet,ideal}}$ for attached jets with $d_{\mathrm{jet}} = d_{\mathrm{n}}$ and the dynamic viscosity ν. The gear Reynolds number is

$$\mathrm{Re}_\omega = \frac{2\omega r_{\mathrm{t}}^2}{\nu}. \tag{4.6}$$

This complex correlation for varying $\mathrm{Re}_{\mathrm{nozzle}}$ and Re_ω is depicted in Figure 4.12. Von Plehwe (2022) postulates that the oil jet can reach the bottomland of the tooth at low rotational speeds, resulting in high heat transfer. Increasing the rotational speed further causes a decrease in heat transfer, as the jet can only reach the active flank of the gear tooth. Von Plehwe (2022) makes

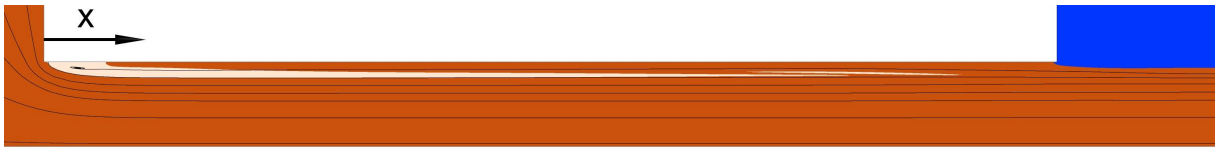

(a) $t = 6.7 \cdot 10^{-4}$ s

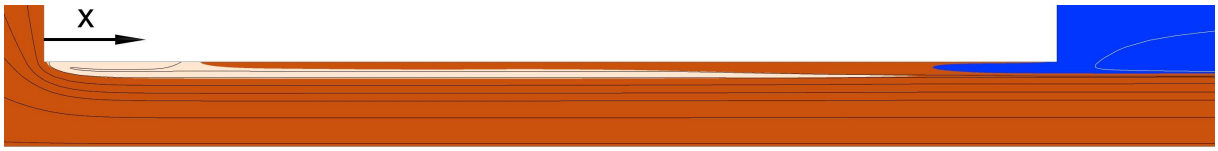

(b) $t = 12 \cdot 10^{-4}$ s

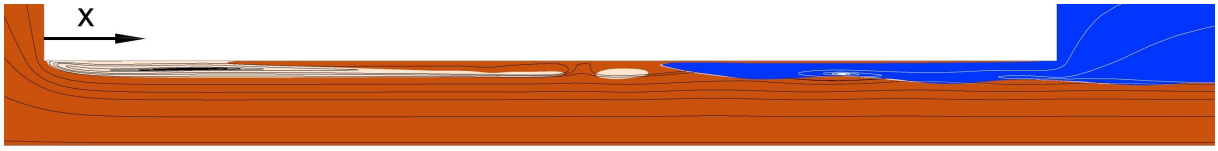

(c) $t = 17.3 \cdot 10^{-4}$ s

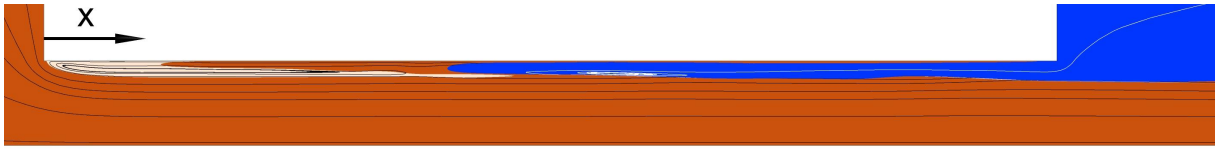

(d) $t = 22.6 \cdot 10^{-4}$ s

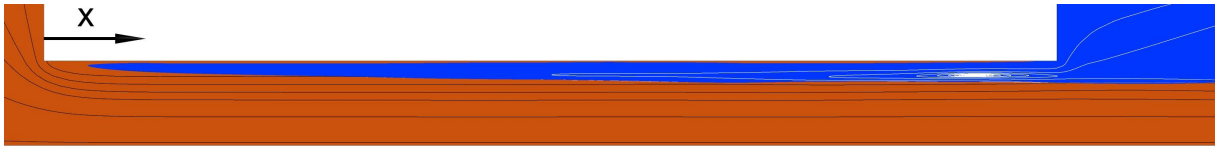

(e) $t = 28.1 \cdot 10^{-4}$ s

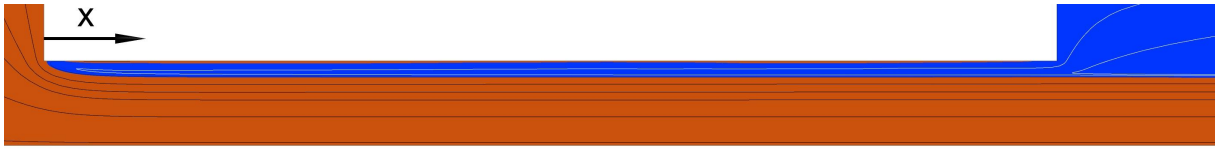

(f) $t = 33.6 \cdot 10^{-4}$ s

Figure 4.9: Simulated nozzle flow with N115 and $\Delta p = 12$ bar with the liquid oil in dark orange, oil vapour in light orange and air in blue at different time steps t. The streamlines of both oil phases are depicted in black. The streamlines of the air phase are depicted in white.

use of the impingement angle β to differentiate between operating points, where the jet only impinges on the active flank or is capable of reaching the bottomland ($\beta \leq 33.8°$) or even the

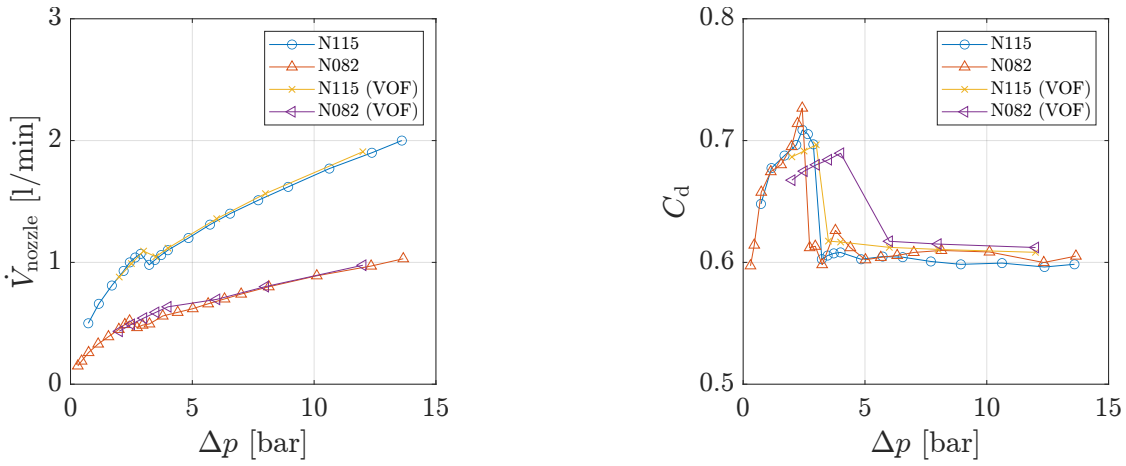

(a) (b)

Figure 4.10: Change of volume flow rate (a) and discharge coefficient (b) with the pressure difference. Numerical results with (VOF) in the legend.

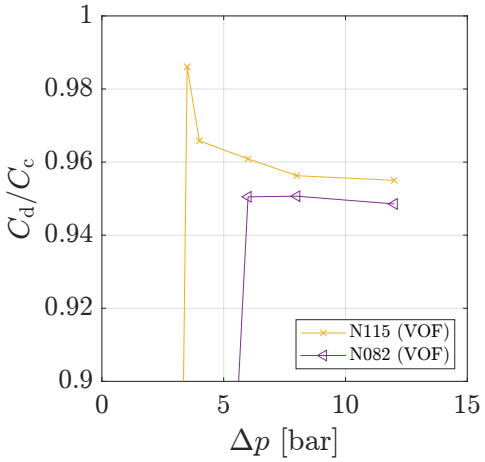

Figure 4.11: Ratio of C_d to C_c in numerical results.

passive flank of the tooth ($\beta \leq 28.7°$). The impingement angle is defined as

$$\beta = \mathrm{atan}\left(\frac{u_\mathrm{gear} - u_\mathrm{jet,t}}{u_\mathrm{jet,r}}\right), \tag{4.7}$$

with the circumferential gear speed at pitch radius u_gear, the tangential and radial jet speeds at the nozzle outlet, $u_\mathrm{jet,t}$ and $u_\mathrm{jet,r}$. However, von Plehwe (2022) employs the ideal jet velocity $u_\mathrm{jet,ideal}$ to calculate β, which is different from the real jet velocity in operating points with hydraulic flip. The ideal and real impingement angles β_ideal and β_real will be used in the following to account for the effective jet diameters of N115 nozzles in spraybar J100, calculated with Equation 4.4. The decline of heat transfer for separated oil jets, where $\mathrm{Re}_\mathrm{nozzle} > 2251$, starts at impingement angles of $\beta_\mathrm{ideal} = 56.7°$, $55.5°$ and $48.8°$ for $\mathrm{Re}_\mathrm{nozzle} = 2639$, 3295 and 3954, respectively. When calculated with $d_\mathrm{jet,real}$, the declines start at $\beta_\mathrm{real} = 37.5°, 36°$ and $29°$ respectively, which are similar to those calculated for $\mathrm{Re}_\mathrm{nozzle} = 1757$ and 2251 with $\beta_\mathrm{ideal} = \beta_\mathrm{real} = 25.2°$ and $26.6°$. These values are also closer to the threshold values of $\beta = 33.8°$ and $28.7°$ for impingement on

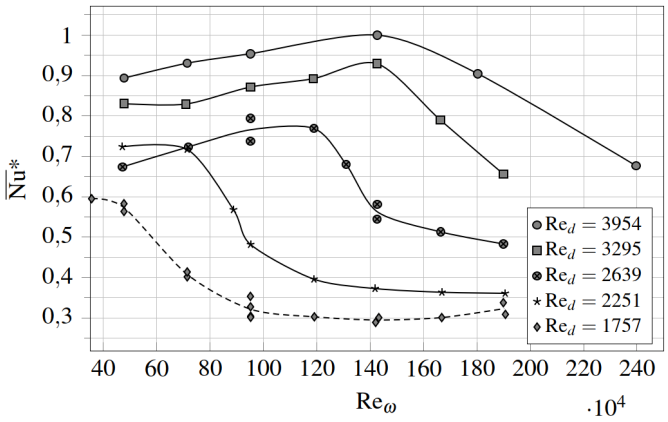

Figure 4.12: Change of $\overline{Nu^*}$ with $Re_d = Re_{nozzle}$ and Re_ω (von Plehwe, 2022).

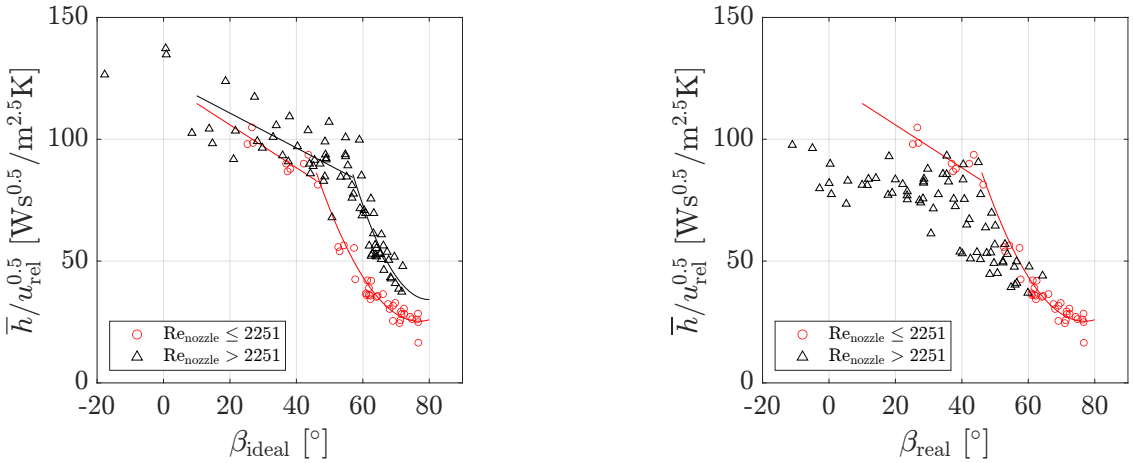

Figure 4.13: Change of $\overline{h}$ with β_{ideal} (a) and β_{real} (b) for attached ($Re_d = Re_{nozzle} \leq 2251$) and separated J100 (N115) jets (von Plehwe, 2022).

the bottomland and passive flank, respectively.

Von Plehwe (2022) introduces a correlation for the average heat transfer coefficient in the form of

$$\overline{h} = u_{rel}^{0.5}(C_1\beta^2 + C_2\beta + C_3), \tag{4.8}$$

with the relative jet velocity u_{rel} calculated via vector subtraction of u_{gear} from u_{jet}. The constants C_1, C_2 and C_3 differ for attached and separated jets as well as for $\beta < \beta_{crit}$ in each regime (Figure 4.13a). It is investigated whether accounting for the jet contraction eliminates the need for a second correlation for the separated jet. Eliminating the second correlation could mean that the derived correlation is not specific to a jet diameter and can potentially be applied to other nozzle geometries. However, the correlation for the attached jet does not reproduce the same level of accuracy when applied on operating points with jet separation if the changed jet diameter is accounted for (Figure 4.13b). This means that the correlation derived is specific to a jet diameter. This shortcoming of the correlation will be addressed by the empirical model developed in the next chapter.

5 Development of the Empirical Heat Transfer Model

The first phase of the empirical heat transfer model development is the investigation of an initial test matrix to derive the significant parameters that influence the heat transfer the most. This test matrix includes 128 operating points (OPs) with spraybar J100, already reported by von Plehwe (2022), 63 new OPs with J101 and 36 new OPs with J102. From these OPs, those with an oil temperature outside the range $T_{\mathrm{oil}} = 80 \pm 4°\mathrm{C}$ are neglected to rule out the viscosity influence, which is not investigated in this work. An optimal test matrix will be generated in the second phase to uniformly cover the relevant parameter space measurable with the test rig. New measurement results will be utilised to develop the empirical model.

5.1 Determination of Significant Parameters

The dataset for determining significant parameters consists of 111 OPs with J100, 51 OPs with J101 and 36 OPs with J102. The operating parameters of these OPs are within the ranges of

- $78\ \mathrm{rad/s} \leq \omega \leq 524\ \mathrm{rad/s}$ for angular velocity,
- $-30° \leq \alpha \leq 45°$ for jet inclination and
- $1.13\ \mathrm{l/min} \leq \dot{V}_{\mathrm{oil}} \leq 10.33\ \mathrm{l/min}$ for total volume flow rate.

522 data pairs of OPs are created to enable a comparison of the spraybars with each other. These data pairs fulfil the following conditions:

- both OPs have different spraybars (J100, J101 or J102),
- both OPs have similar angular velocities ω and jet inclinations α (both within ±5%),
- the total oil volume flow rate $\dot{V}_{\mathrm{oil}}$ may vary,
- the jet velocity u_{jet} may vary.

Figure 5.1a shows all 522 data pairs with the surface-averaged heat transfer coefficients $\overline{h}$ of individual OPs A and B as the x and y coordinates. As described in Chapter 3, spraybar J100 has 4 nozzles of type N115 with $d_{\mathrm{N115}} = 1.15$ mm, whereas J101 and J102 have 4 and 8 nozzles of type N082 with $d_{\mathrm{N082}} = 0.82$ mm, respectively. This difference in diameter means that the cross-section of N115 is nearly twice as large as that of N082. Since the contraction of both geometries is similar in the case of a hydraulic flip, the same is true for the separated jet diameters as well. Therefore, two operating points with $\dot{V}_{\mathrm{N115}} = 2\dot{V}_{\mathrm{N082}}$ would have similar jet velocities $u_{\mathrm{jet,N115}} \approx u_{\mathrm{jet,N082}}$. If the jet inclination α, the angular velocity ω, and the oil temperature T_{oil} are also kept constant, which is the case for each data pair, the resulting kinematics and impingement depths will be identical in both cases. This enables an investigation of the influence of volume flow rate on the heat transfer with the number of jets and jet velocities remaining constant if the spraybars J100 and J101 are compared. Furthermore, a second comparison is possible, where the total volume flow rate is kept constant, but each jet is split into two smaller jets with constant velocities, as in the case of J100 and J102. A third investigation regarding how doubling the volume flow rate by doubling the number of jets affects the heat transfer can

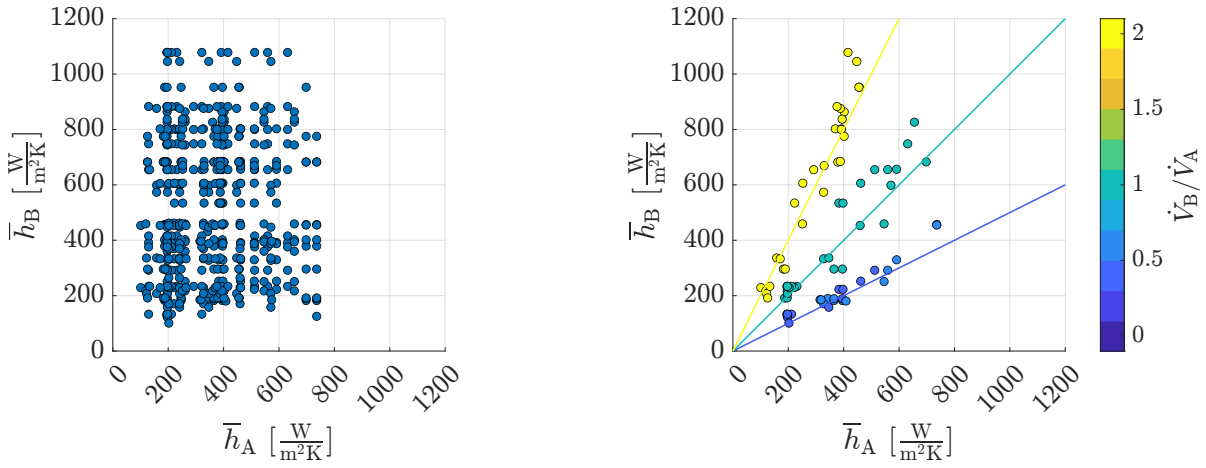

(a) (b)

Figure 5.1: All OP pairs with different spraybars, similar angular velocities, and similar jet inclinations (a) and OP pairs where the volume flow rate investigation is possible (b). The volume flow rate ratios are depicted via the colour scale in (b).

be performed by comparing J101 and J102. Figure 5.1b includes all 81 OP pairs for which one of these three comparisons is possible. The ratio of total volume flow rates $\dot{V}_B/\dot{V}_A$ is depicted in colour. A ratio of $\dot{V}_B/\dot{V}_A \approx 0.5$ means that A is an OP with J100, and B is an OP with J101. For $\dot{V}_B/\dot{V}_A \approx 1$, A is an OP with J100, and B is an OP with J102. If the ratio is $\dot{V}_B/\dot{V}_A \approx 2$, A is an OP with J101, and B is an OP with J102. The lines going through the origin are linear functions with slopes 0.5, 1, or 2, matching the line's colour.

As shown in Figure 5.1b, the ratio of heat transfer coefficients follows the same trend as the ratio of volume flow rates. This implies a linear correlation between the volume flow rate and the heat transfer coefficient if the kinematics is kept constant, even if the number of jets and jet diameters differ. Figure 5.2a has the same data pairs as Figure 5.1b, where $\overline{h}$ is scaled with the ratio $\dot{V}_A/\dot{V}_B$. The colour scale depicts the ratio of $u_{jet,B}/u_{jet,A}$, which is, in this case, equal to 1 for all data pairs. The diagonal line is a linear function with $\overline{h}_B(\dot{V}_A/\dot{V}_B) = \overline{h}_A$. The coefficient of determination for this basic fit is $R^2 = 0.912$. Therefore, the volume flow rate is selected as the first significant parameter of the heat transfer model. The mean heat transfer coefficient will be scaled with the normalised volume flow rate

$$\Psi = \frac{\dot{V}}{\dot{V}_{max}} \tag{5.1}$$

and with the maximum measured surface and time-averaged heat transfer coefficient $\overline{h}_{max}$

$$\overline{h^*} = \frac{\overline{h}}{\overline{h}_{max}\Psi}, \tag{5.2}$$

for the model development.

Including the remaining OP pairs, where $u_{jet,B}/u_{jet,A} \neq 1$, into the diagram (Figure 5.2b) shows

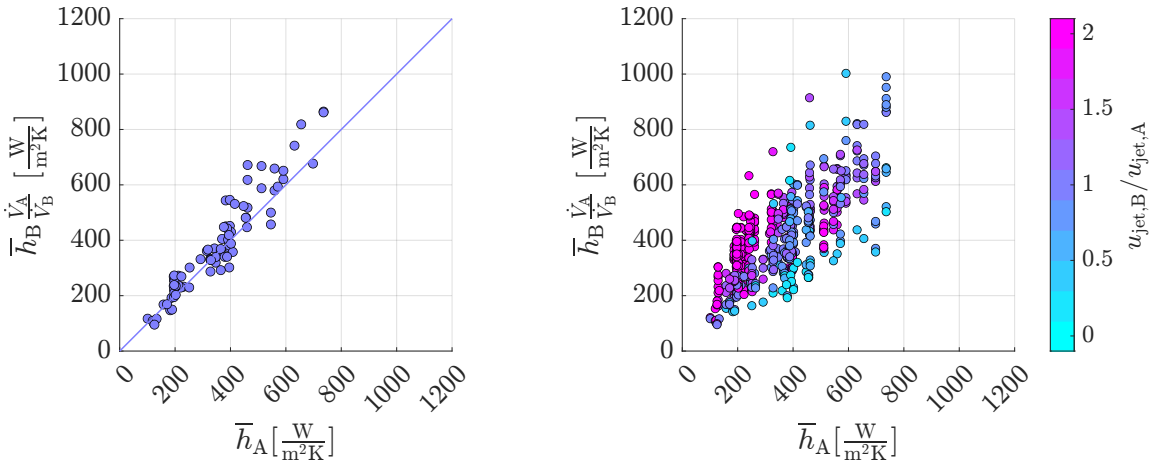

(a) (b)

Figure 5.2: OP pairs of volume flow rate investigation with heat transfer coefficients scaled by volume flow rate ratios (a) and all OP pairs with scaled heat transfer coefficients (b). The jet velocity ratios are depicted via the colour scale in (b).

how complex the correlation between the heat transfer and the oil jet gear kinematics can be. Most OP pairs with $u_{\mathrm{jet,B}}/u_{\mathrm{jet,A}} > 1$ are positioned above the diagonal resulting in higher heat transfer coefficients than what is explicable with the volume flow rate differences. The opposite is true for most of the cases where $u_{\mathrm{jet,B}}/u_{\mathrm{jet,A}} < 1$. However, there are numerous OP pairs for which a simple generalisation such as the higher the jet speed, the higher the heat transfer coefficient, would lead to severe over- or underestimation errors, e.g. for the OP pairs with $u_{\mathrm{jet,B}}/u_{\mathrm{jet,A}} \ll 0.5$, $\overline{h}_A \approx 400\ \mathrm{W/(m^2K)}$ and $\overline{h}_B(\dot{V}_A/\dot{V}_B) > 400\ \mathrm{W/(m^2K)}$. Further investigation is required to understand the complex interdependency observed here.

Parameters describing how deep the oil reaches into the tooth space, such as impingement angle, impingement depth, or penetration depth, have long been advocated as significant parameters to predict the heat transfer on impingement cooled gears. The reason for the significance of these parameters is that they are a measure to describe how much of the gear flank is directly impinged by the jet before exiting the tooth space. If the jet can reach, for example, the passive flank of the tooth, it will impinge on the bottomland and the active flank as well. A greater area will be available for the heat transfer between the gear surface and the oil, even if the total oil volume within a tooth space is the same as another operating point where the impingement only takes place on a small part of the active flank. Using the vectorial model of Akin et al. (1975) with the modifications introduced by Keller (2022), it is possible to find an impingement radius r_{im}, where the jet first reaches the gear surface

$$r_{\mathrm{im,vectorial}} = r_{\mathrm{t}} - \frac{\frac{\pi}{2} + 2\tan(\gamma_{\mathrm{p}})}{\frac{1}{m}\left(\tan(\gamma_{\mathrm{p}}) + \frac{u_{\mathrm{gear}} - u_{\mathrm{jet}}\sin(\alpha_{\mathrm{eff}})}{u_{\mathrm{jet}}\sin(\alpha_{\mathrm{eff}})}\right)}, \tag{5.3}$$

with the pressure angle at the pitch radius γ_{p} and the effective jet inclination α_{eff}. The jet

inclination α is set and measured at the rotational axis of the spraybar with r_{spraybar}. However, the vectorial model defines the starting point as the last contact point of the oil jet tip and topland of the leading tooth with r_{t}. If the oil jet is inclined, the starting point will not be located at the same radius as r_{spraybar}. Therefore, the radial and tangential components of the oil jet velocity will differ at the rotational axis of the spraybar and the starting point of the vectorial model (Figure 5.3a). The effective jet inclination α_{eff} considered in the vectorial model can be determined via

$$\alpha_{\text{eff}} = \arcsin\left(\frac{r_{\text{spraybar}}}{r_{\text{t}}}\sin(\alpha)\right). \tag{5.4}$$

The impingement length l_{im}, also called wetted length by Kromer et al. (2020), is used in this work instead of the impingement depth and impingement angle since it precisely represents the length of the path directly impinged by the oil jet. l_{im} equals the distance between the first impingement point and the topland in s coordinates. For an involute gear flank, l_{im} can be calculated by making use of the arc length for a circle involute with

$$l_{\text{arc}} = \frac{r_{\text{b}}}{2}\tau^2, \tag{5.5}$$

with the base radius r_{b} and tangential angle τ. The tangential angle is equal to the tangent of the pressure angle γ with

$$\tau = \tan(\gamma_{\text{r}}) = \tan\left(\cos\left(\frac{r_{\text{b}}}{r}\right)\right), \tag{5.6}$$

at a radius r. Using both equations, the impingement length of the vectorial model $l_{\text{im,vectorial}}$ can be calculated via

$$l_{\text{im,vectorial}} = \frac{r_{\text{b}}}{2}\left(\tan\left(\cos\left(\frac{r_{\text{b}}}{r_{\text{t}}}\right)\right)^2 - \tan\left(\cos\left(\frac{r_{\text{b}}}{r_{\text{im,vectorial}}}\right)\right)^2\right). \tag{5.7}$$

The impingement length is normalised as

$$l^*_{\text{im,vectorial}} = \frac{l_{\text{im,vectorial}}}{l_{\text{max}}} \tag{5.8}$$

with the maximum possible impingement length l_{max}, which equals the total circumferential length between two toplands.

Alternatively, the virtual kinematic model of Akin and Townsend (1989) can be utilised to calculate the impingement radius and length. The modifications of Keller (2022) are required for the investigated gear geometry. The impingement radius is calculated via

$$r_{\text{im,virtual}} = \frac{\theta_{\text{w}} u_{\text{jet}} \sin(\alpha_{\text{eff}})}{\omega \sin(\theta_{\text{a}})}, \tag{5.9}$$

analogous to Equation 2.17, and the normalised impingement length $l^*_{\text{im,virtual}}$ analogous to Equations 5.7 and 5.8. The definition of angles θ_{w} and θ_{a} will be omitted here and are taken from Akin and Townsend (1989).

Both calculation methods have some weaknesses in their definitions. Firstly, for those OPs

where the oil jet can reach the bottomland, Equations 5.3 and 5.9 will result in impingement radii less than r_r. In this case, the impingement length calculated with Equation 5.7 would assume a continuation of the involute profile below r_r and cannot generate an accurate value for the actual tooth profile. This shortcoming is solved relatively easily for the virtual kinematic model since the gear is not modelled as a linear rack. A second shortcoming of both models is for OPs with impingement on the passive flank. Equation 5.7 would lead to a continuous change of impingement length over the passive flank. However, the impingement on the passive flank would either start at the tip or not occur at all. This problem is also solvable for the virtual model by defining a minimum θ angle, below which the impingement starts on the passive flank setting $l_{im} = 1$.

The relatively simple vectorial model of Akin et al. (1975) is easier to apply to different geometries with negligible computational requirements. However, it suffers from the aforementioned challenges and could generate inaccurate predictions if the gear has a smaller curvature and the oil jet does not impinge on the active flank. The virtual kinematic model of Akin and Townsend (1989) is more accurate and adjustable for different gear geometries and impingement positions. However, its definition is relatively complex and error-prone in its implementation. The virtual kinematic model also requires an iterative numerical approach to find the impingement radius, which increases the computational effort compared to the vectorial model. Furthermore, none of the methods can account for slight deviations from an idealised involute gear profile, such as the fillets between the bottomland and gear flanks.

A new impingement position calculation method is proposed in this work. The impingement point for any given gear geometry can be determined if the flight path of the oil jet tip is simulated. This simplified simulation starts at $t = 0$ with two starting conditions: The oil jet tip's radial position is $r = r_t$, and its angular position is $\zeta = 0.5\pi$. The radial velocity component is

$$u_{tip} = \frac{dr}{dt} = -u_{jet}\cos(\alpha_{eff}), \tag{5.10}$$

and the angular velocity component is

$$\omega_{tip} = \frac{d\zeta}{dt} = -\omega + \frac{u_{jet}\sin(\alpha_{eff})}{r}. \tag{5.11}$$

The radial and angular positions of the oil jet tip can be calculated for a given time range using the starting conditions. These positions can then be converted into Cartesian coordinates with

$$x_c(t) = r(t)\cos(\zeta(t)), \tag{5.12}$$

$$y_c(t) = r(t)\sin(\zeta(t)). \tag{5.13}$$

The gear profile is projected onto the same coordinate system with the tip of the passive flank positioned at $x_c = 0$ and $y_c = r_t$, as shown in Figure 5.3b. The impingement point is where the flight path (the dotted line in Figure 5.3b) intersects the gear profile. The impingement length l_{im} can be calculated using the actual gear profile instead of Equation 5.7. In some occasions, the impingement can start at the topland, but the oil jet will fly over a portion of the passive flank

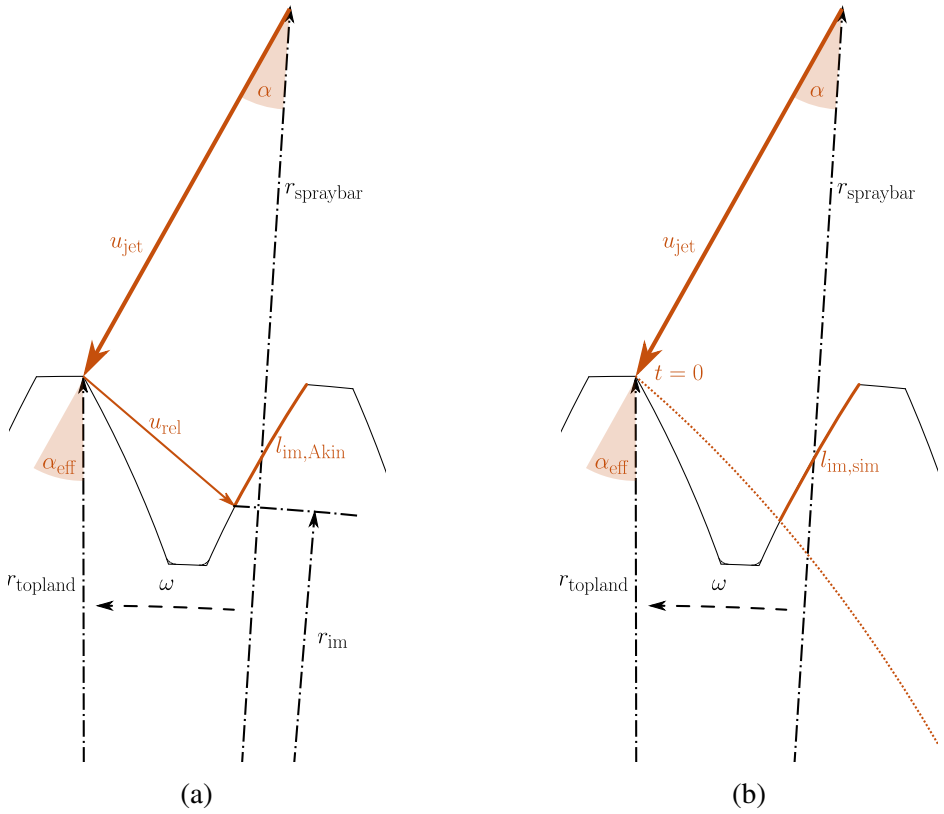

Figure 5.3: Determination of impingement lengths via the vectorial model (a) and the oil jet tip simulation (b).

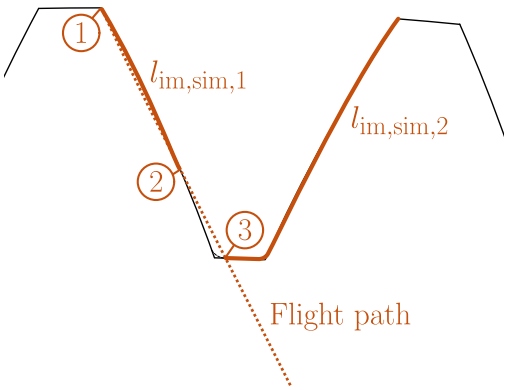

Figure 5.4: Calculation of impingement length for operating points with intermittent impingement on the gear flank with three intersections of the gear profile and flow path.

due to its curvature (Figure 5.4). In this case, the impingement length consists of two sections. The first one starts at the first intersect at the topland and ends at the second intersect on the passive flank. The second section starts at the third intersection located at the bottomland and spans to the next topland.

Figure 5.5a and Figure 5.5b compare the impingement lengths calculated with the oil jet tip simulations and those calculated with the vectorial and virtual kinematic models. The horizontal and vertical lines with $l^* = 0.4485$ denote the maximum possible impingement length on the

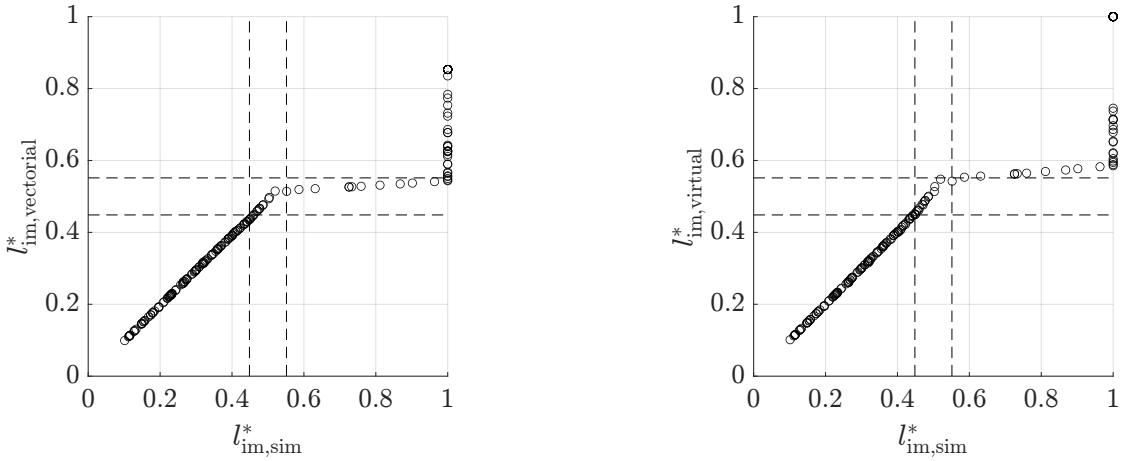

Figure 5.5: Comparison of impingement lengths calculated with the vectorial model and the oil jet tip simulation method (a) as well as with the virtual kinematic model and the oil jet tip simulation method (b).

involute profile of the active flank just above the fillet. The lines with $l^* = 0.5515$ are the limits after which the involute profile on the passive flank starts. All methods deliver similar results if the impingement begins on the active flank. The vectorial and virtual kinematic models slightly deviate from the simulation method if the impingement begins on the bottomland. The methods diverge significantly as the oil jet starts contacting the passive flank. Using the simulation method as a benchmark, the virtual kinematic model requires comparable computation times, while the vectorial model's computational requirement is negligible. Accuracy-wise, the virtual kinematic model cannot outperform the vectorial model for the investigated gear geometry. Therefore, the vectorial model is more suited to use on large datasets, e.g. if a multivariate optimisation study is conducted to decide on the geometrical and operational parameters of the cooling system. For smaller datasets, such as those used in this work to develop the empirical model, the simulation method is preferred due to its higher accuracy, especially at operating points with impingement starting on the passive flank or the bottomland. Therefore, the simulation method is used in the following if not stated otherwise.

The variation in the normalised heat transfer coefficient $\overline{h^*}$ as a function of the normalised impingement length $l^*_{\mathrm{im,sim}}$ is depicted in Figure 5.6a. If all OPs are considered together, the heat transfer increases with increasing impingement length until the passive flank is reached at $l^*_{\mathrm{im,sim}} = 0.5515$. No significant effect of impingement length is observed for OPs with $l^*_{\mathrm{im,sim}} > 0.5515$. With the effects of volume flow rate and impingement length accounted for, additional significant parameters are required to minimise the dispersion in the normalised heat transfer coefficients observed in Figure 5.6a and improve the accuracy of the empirical model.

The distribution of the oil following the impingement is expected to depend on two additional parameters: the impact impulse resulting from the relative motion of the oil jet and the gear flank, which contributes to a broader distribution of the oil film, and the centrifugal force acting upon the oil film, which hinders its propagation. A new parameter, the so-called relative velocity

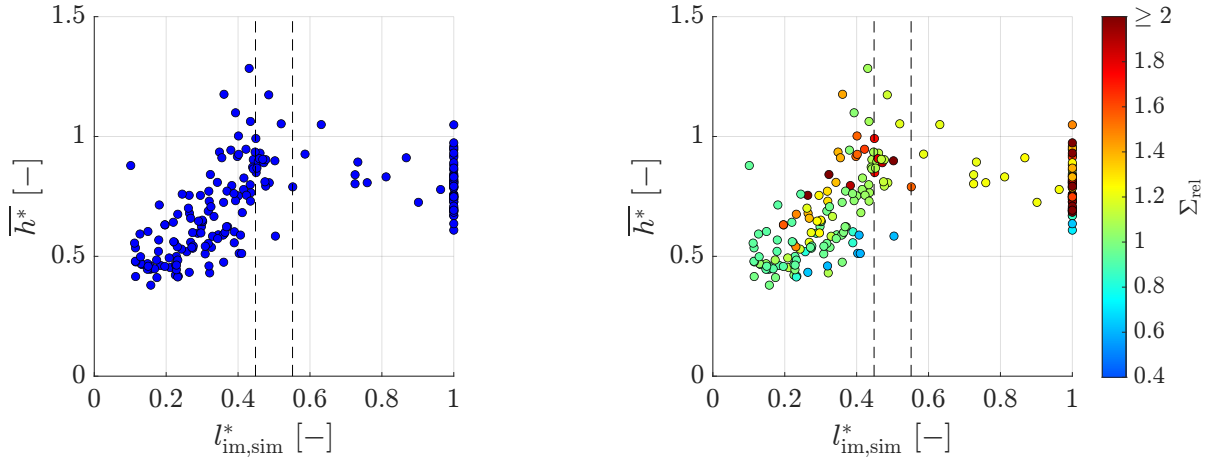

(a) (b)

Figure 5.6: Variation of normalised heat transfer coefficients with the normalised impingement lengths (a) with relative velocity ratio represented in colour scale (b).

ratio

$$\Sigma_{\mathrm{rel}} = \frac{u_{\mathrm{rel}}}{u_{\mathrm{gear}}}, \tag{5.14}$$

is proposed to model the influence of these counteracting effects. The data points in Figure 5.6a are coloured with respect to the relative velocity ratio in Figure 5.6b. For $l^*_{\mathrm{im,sim}} < 0.5515$, the general trend is that a higher Σ_{rel} results in a higher $\overline{h^*}$ at a given $l^*_{\mathrm{im,sim}}$, e.g. around $l^*_{\mathrm{im,sim}} \approx 0.3$. For a given Σ_{rel}, e.g. $\Sigma_{\mathrm{rel}} = 1.3$, $\overline{h^*}$ reaches a maximum value and declines afterwards for higher $l^*_{\mathrm{im,sim}}$. However, both observations are extremely limited in explaining the complete interdependency between $\overline{h^*}$ and the significant parameters since the test matrix is generated with the operational parameters of the test rig, which does not translate into an optimal distribution of Σ_{rel} and $l^*_{\mathrm{im,sim}}$. For example, the volume flow rate affects the jet velocity directly and indirectly since a hydraulic flip is expected after a certain threshold. The resulting jet and the remaining operational parameters, such as the jet inclination and the rotational speed, affect $l^*_{\mathrm{im,sim}}$ and Σ_{rel} in different ways. Thus, a new optimal test matrix is proposed to investigate the significant parameters thoroughly.

5.2 Measurements with an Optimal Test Matrix

The limits for the operating parameters of the experimental setup are very well defined, with the maximum possible volume flow rate, the inclination limits of the spraybar and the rotational speed limit of the rotor. It is essential to project these limits into the parameter space formed by the significant parameters

- Normalised volume flow rate Ψ,
- Normalised impingement length $l^*_{\mathrm{im,sim}}$,

- Relative velocity ratio Σ_{rel},

to determine the optimal test matrix. A 4D-grid of 42315 OPs is generated by varying ω, α, $\dot{V}_{\text{nozzle}}$ and the spraybar configuration within the limits of the experimental setup, with:

- Angular velocity 104 rad/s $< \omega <$ 420 rad/s with a step size of 10.4 rad/s,
- Jet inclination $-45° < \alpha < 45°$ with a step size of 1°,
- Nozzle volume flow rate $\dot{V}_{\text{oil}} \in \{0.35, 0.65, 0.7, 0.75, 0.95\}$ l/min,
- Spraybar J100, J101 or J102.

Figure 5.7 depicts the $l^*_{\text{im,sim}}$ and Σ_{rel} dimensions of the parameter space. The red area is the maximum possible parameter space the operational parameters allow. Within this red area, the 198 OPs of the initial test matrix discussed in the previous section are shown as red crosses. 62 OPs are in the region right of the dashed line in Figure 5.7 at $l^*_{\text{im,sim}} = 0.5515$, above which the impingement starts on the passive flank. A variation of $l^*_{\text{im,sim}}$ on the right side of the dashed line is extremely challenging since any slight variation from the target parameters of an OP may lead the oil jet to either completely miss the passive flank or have continuous impingement over it in the experiment. Furthermore, the preliminary results with the initial test matrix suggest that the maximum heat transfer coefficient is reached for $l^*_{\text{im,sim}} \leq 0.5515$. The focus of the investigation for the new empirical model should lie on the left side of the dashed line to have more OPs suited for the investigation of the influence each significant parameter has. OPs with $l^*_{\text{im,sim}} > 0.5515$ are still required to test the hypothesis of reaching the maximum heat transfer coefficient below $l^*_{\text{im,sim}} = 0.5515$. Furthermore, most of the 136 OPs of the initial test matrix with $l^*_{\text{im,sim}} \leq 0.5515$ are positioned around two curves where Σ_{rel} and $l^*_{\text{im,sim}}$ are not independently varied, which lowers the generalisation capabilities of an empirical model. A more uniform distribution of OPs in this region is essential to rule out a possible over-fitting of the model to a specific set of Σ_{rel} and $l^*_{\text{im,sim}}$ values.

An optimal test matrix is proposed to resolve the parameter space more efficiently and uniformly. The new parameter space is generated with the minimum rotational speed increased to $\omega_{\text{min}} =$ 156 rad/s and jet inclination limited between $-30° < \alpha < 30°$. This new parameter space is depicted in black in Figure 5.7. It is filled with 230 new OPs, with 184 having $l^*_{\text{im,sim}} < 0.5515$ and thus no impingement on the passive flank. The parameter space also has a third dimension, Ψ, which is not depicted in the two-dimensional plot in Figure 5.7. Using the same variations in volume flow rate with $\dot{V}_{\text{oil}} \in \{0.35, 0.65, 0.7, 0.75, 0.95\}$ l/min, it is possible to generate multiple OPs with similar Σ_{rel} and $l^*_{\text{im,sim}}$ but different Ψ values. For example, there are five OPs with Ψ values of 0.25, 0.29, 0.37, 0.58 and 0.50, for all of which $\Sigma_{\text{rel}} \approx 1.45$ and $l^*_{\text{im,sim}} \approx 0.35$, as shown in Table 5.1.

5.3 Results

The results of the optimal test matrix measurements are discussed in the following. First, the findings of the initial test matrix will be re-evaluated by drawing conclusions about the influence of each significant parameter. The results concerning the surface-averaged heat

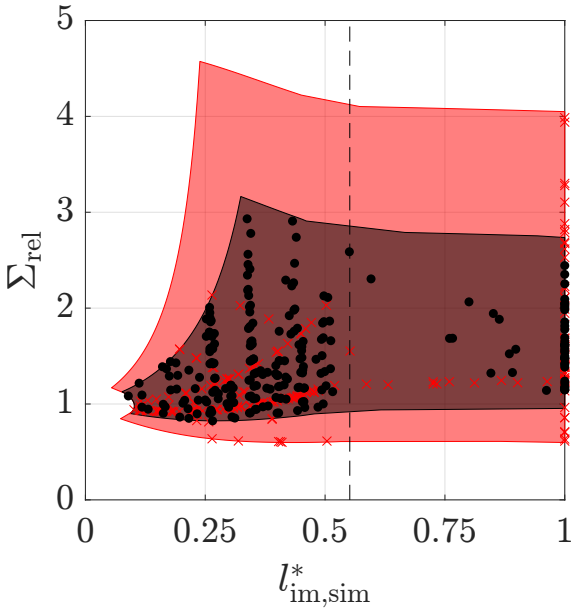

Figure 5.7: Parameter space of the experimental setup and the OPs in the initial test matrix in red, and the parameter space for optimal test matrix generation and its OPs in black.

Table 5.1: OPs with similar impingement lengths and relative velocity ratios.

	Spraybar	ω [rad/s]	α [°]	u_{jet} [m/s]	$l^*_{\mathrm{im,sim}}$	Σ_{rel}	Ψ	$\overline{h^*}$
OP017	J101	261.6	-3	33.62	0.34	1.45	0.25	0.94
OP096	J101	303.5	-3	39.33	0.35	1.45	0.29	1.00
OP131	J101	377	-3	49.93	0.35	1.47	0.37	1.02
OP196	J100	304	-3	40.07	0.35	1.47	0.58	0.90
OP209	J100	261.8	-3	34.7	0.35	1.47	0.50	0.96

transfer coefficient and the spatial distribution will be examined. Then, a novel empirical model will be proposed for the surface-averaged heat transfer coefficient. This model will be cross-validated by splitting the test matrix into training and test data sets. The surface-averaged heat transfer coefficients will be predicted for the cases numerically investigated by Keller (2022) and correlated with the wetted areas. Finally, the optimisation potential of the empirical model will be showcased.

5.3.1 Influence of Individual Parameters

In the initial test matrix, the surface-averaged heat transfer coefficient exhibits a linear dependency on the oil volume flow rate for the limited number of operating points, where the rotational speed ω, the jet inclination α and the oil jet velocity u_{jet} are kept identical. This comparison is only possible for OP pairs that incorporate different spraybars. In contrast, the optimal test matrix allows comparisons for OP pairs, where the operating parameters may differ while still resulting

in the same values for the normalised impingement length $l^*_{\mathrm{im,sim}}$ and the relative velocity ratio Σ_{rel}. Therefore, comparisons between OPs with the same spraybar are also possible. Table 5.1 presents five comparable OPs, where $l^*_{\mathrm{im,sim}}$ and Σ_{rel} differ only within a range of ±2.5% even though the rotational speed and the oil jet velocity vary up to 44% and 49%, respectively. The normalised heat transfer coefficients $\overline{h^*}$ are given in the last column, with the highest difference between these OPs being 13%.

The dependency of heat transfer on the volume flow rate can also be seen in Figure 5.8, analogous to the initial test matrix. In Figure 5.8a, the surface-averaged heat transfer coefficients of OP pairs with comparable $l^*_{\mathrm{im,sim}}$ and Σ_{rel} are presented with the volume flow rate ratios of OPs A and B depicted via the colour scale. Changing the y-axis to $\overline{h}_{\mathrm{B}}(\dot{V}_{\mathrm{A}}/\dot{V}_{\mathrm{B}})$ in Figure 5.8b collapses all OPs around the diagonal, suggesting that the previously proposed relation of $\overline{h} \propto \Psi$ is true. If the OP pairs are fitted to the function

$$\overline{h}_{\mathrm{A,prd}} = \overline{h}_{\mathrm{B}} \left(\frac{\dot{V}_{\mathrm{A}}}{\dot{V}_{\mathrm{B}}} \right)^{C_{\mathrm{V}}} \tag{5.15}$$

via least squares fitting for the predicted heat transfer coefficient of A ($\overline{h}_{\mathrm{A,prd}}$), $C_{\mathrm{V}} = 0.835$ results in the highest coefficient of determination $R^2 = 0.772$. For comparison, $R^2 = 0.666$ if $C_{\mathrm{V}} = 1$. The relatively low R^2 does not mean that it is inferior to the fitting with the initial test matrix. The lower score is due to the increased number of OP pairs with volume flow rate ratios differing from 0.5, 1 and 2. This populates the diagram in Figure 5.8a more densely around the average of all $\overline{h}_{\mathrm{A}}$, denoted by $\overline{\overline{h}_{\mathrm{A}}}$, thus lowering the denominator in

$$R^2 = 1 - \frac{\sum(\overline{h}_{\mathrm{A}} - \overline{h}_{\mathrm{A,prd}})^2}{\sum(\overline{h}_{\mathrm{A}} - \overline{\overline{h}_{\mathrm{A}}})^2}. \tag{5.16}$$

The normalised heat transfer coefficient will be redefined as

$$\overline{h^+} = \frac{\overline{h}}{\overline{h}_{\mathrm{max}} \Psi^{C_{\mathrm{V}}}} \tag{5.17}$$

with $C_{\mathrm{V}} = 0.835$ since it is better suited to fit the results in comparison to the previous definition with $\overline{h^*}$.

The change of $\overline{h^+}$ with $l^*_{\mathrm{im,sim}}$ is depicted in Figure 5.9a. Similar to the initial test matrix, it can generally be inferred that $\overline{h^+}$ initially increases with $l^*_{\mathrm{im,sim}}$, reaches a maximum and declines afterwards. However, the relatively large spread of the $\overline{h^+}$ values cannot be overlooked. Separating the OPs by jet diameter in Figure 5.9b reveals new findings. Unfortunately, it is not feasible to generate OPs by varying the occurrence of hydraulic flip and significant parameters separately. This leads to a majority of the OPs having either $d_{\mathrm{jet}} = 0.89$ mm for J100 or $d_{\mathrm{jet}} = 0.64$ mm for J101. Nevertheless, attached oil jets of J101 with $d_{\mathrm{jet}} = 0.82$ mm and separated oil jets of J100 with $d_{\mathrm{jet}} = 0.89$ mm have relatively similar diameters. Therefore, they can be grouped together while investigating the influence of significant parameters on $\overline{h^+}$. The

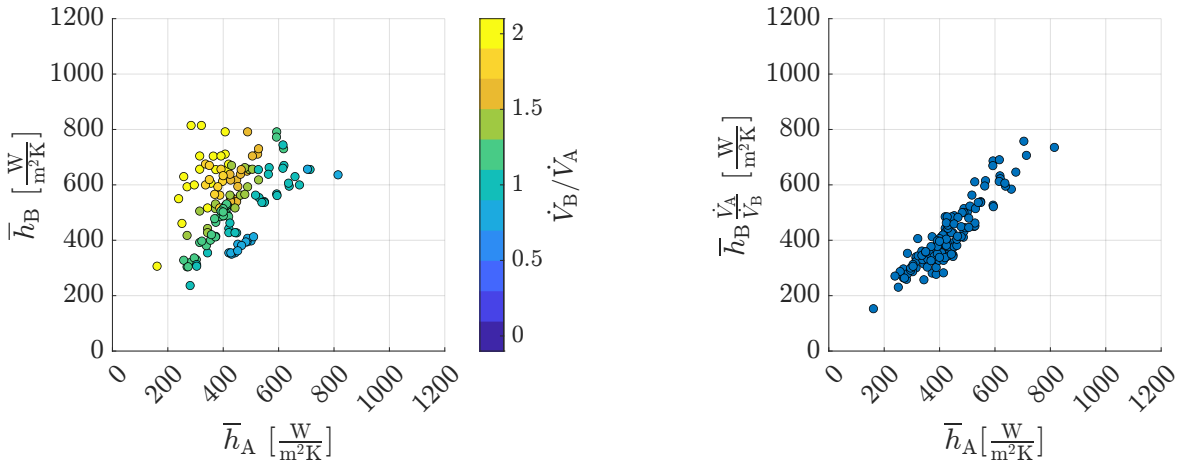

(a) (b)

Figure 5.8: Heat transfer coefficient of OP pairs with comparable impingement lengths and relative velocity ratios (a) and volume flow rate scaled heat transfer coefficients of these OP pairs (b).

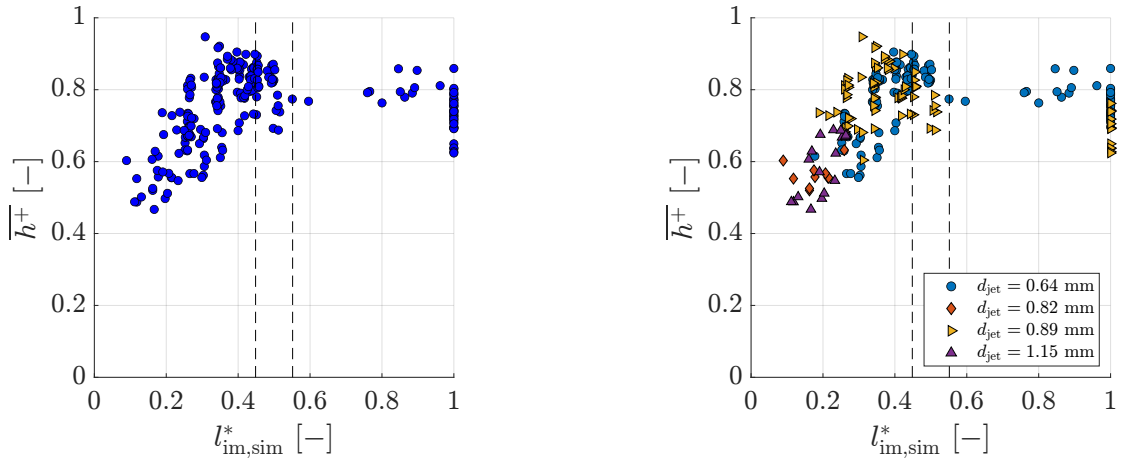

(a) (b)

Figure 5.9: Variation of normalised heat transfer coefficients with the normalised impingement lengths (a) and with distinction by jet diameter (b).

maximum $\overline{h^+}$ value, at which $l^*_{im,sim}$ is reached, and the decline for higher values of $l^*_{im,sim}$ are slightly different for the OPs with 0.82 mm $\leq d_{jet} \leq$ 0.89 mm and the OPs with d_{jet} = 0.64 mm, which suggests an influence of the jet diameter that has not been identified with the initial test matrix measurements. The number of OPs with d_{jet} = 1.15 mm and variation of $l^*_{im,sim}$ for these OPs are too limited to include them in the analysis.

Figure 5.10a shows $\overline{h^+}$ of OPs with d_{jet} = 0.64 mm with $l^*_{im,sim}$ on the x-axis and a continuous range of Σ_{rel} in the colour scale. This plot is too obscure to derive any meaningful conclusions from it. The highest resolution of the parameter space is in the range of $0.8 \leq \Sigma_{rel} < 1.5$, as shown in Figure 5.7. To enable an in-depth investigation in this range, OPs are grouped into discrete sets of Σ_{rel} within $0.8 \leq \Sigma_{rel} < 1.5$ with a step size of 0.1, starting from $0.8 \leq \Sigma_{rel} < 0.9$.

Table 5.2: Properties of fitting functions of Σ_{rel} sets of the OPs with $d_{\mathrm{jet}} = 0.64$ mm. The slope is determined with the $0.9 \leq \Sigma_{\mathrm{rel}} < 1.0$ set.

Σ_{rel} set	Slope	Offset	R^2
$0.8 \leq \Sigma_{\mathrm{rel}} < 0.9$	-	-	-
$0.9 \leq \Sigma_{\mathrm{rel}} < 1.0$	1.4885	0.1058	0.9918
$1.0 \leq \Sigma_{\mathrm{rel}} < 1.1$	1.4885	0.1585	0.9078
$1.1 \leq \Sigma_{\mathrm{rel}} < 1.2$	1.4885	0.2299	0.9124
$1.2 \leq \Sigma_{\mathrm{rel}} < 1.3$	-	-	-
$1.3 \leq \Sigma_{\mathrm{rel}} < 1.4$	1.4885	0.3017	0.8673
$1.4 \leq \Sigma_{\mathrm{rel}} < 1.5$	1.4885	0.3016	0.8405

Figure 5.10b depicts a zoomed-in version of Figure 5.10a with the colour scale limited to the discrete sets of Σ_{rel} within $0.8 \leq \Sigma_{\mathrm{rel}} < 1.5$. Previous observations have shown that the heat transfer coefficient increases linearly with the impingement length until the maximum heat transfer coefficient is reached. Each Σ_{rel} set is divided into two groups of OPs, where the first group consists of OPs with an $l^*_{\mathrm{im,sim}}$ lower than or equal to $l^*_{\mathrm{im,sim}}$ of the OP with the highest $\overline{h^+}$ of the respective Σ_{rel} set. The remaining OPs with higher $l^*_{\mathrm{im,sim}}$ are placed in the other group. The first group is used to find a fitting function, which describes the linear increase of $\overline{h^+}$. A fitting function is not created if the number of OPs in this group is less than 3. The slope of fitting functions for each Σ_{rel} set is the same and is determined with the $0.9 \leq \Sigma_{\mathrm{rel}} < 1.0$ set, which generates the fitting function with the highest coefficient of determination R^2 among all Σ_{rel} sets. The offset in the y-axis is adjusted for the remaining Σ_{rel} sets to achieve the best respective fit. Very high R^2 values are observed for the fitting functions, as listed in Table 5.2. This observation indicates a positive effect of Σ_{rel} on the heat transfer as higher $\overline{h^+}$ can be reached at lower $l^*_{\mathrm{im,sim}}$ if Σ_{rel} is increased. A physical explanation for this effect is the increased oil film propagation for higher Σ_{rel} values. The initial oil film along the impingement path is able to expand further axially and radially on the tooth surface if Σ_{rel} is higher.

Σ_{rel} seems to have a diminishing effect since the fitting functions for $1.3 \leq \Sigma_{\mathrm{rel}} < 1.4$ and $1.4 \leq \Sigma_{\mathrm{rel}} < 1.5$ are not distinguishable from each other in Figure 5.10b. However, this might be due to the limited number of OPs in the $1.3 \leq \Sigma_{\mathrm{rel}} < 1.4$ set and these OPs having very similar $l^*_{\mathrm{im,sim}}$. Remaining OPs with $\Sigma_{\mathrm{rel}} > 1.5$ should also be examined to ensure the diminishing effect. The OPs with $1.3 \leq \Sigma_{\mathrm{rel}} < 2.9$ are plotted in Figure 5.10c with the new Σ_{rel} sets of step size 0.2 in the colour scale. Even at very high values, there is no clear indication of a positive effect of $\Sigma_{\mathrm{rel}} > 1.3$, which supports the diminishing effect observation in Figure 5.10b. A possible explanation for the diminishing effect would be the increase of oil volume splashing away from the gear flank after impingement. This, in turn, would counteract the oil film propagation by decreasing the oil volume available for the heat transfer.

The same investigation is carried out for the OPs with $0.82 \text{ mm} \leq d_{\mathrm{jet}} \leq 0.89$ mm to ensure that the same effects are observed regardless of the jet diameter. Additionally, the effect of jet diameter can be assessed by comparing the outcomes for both jet diameter groups. The

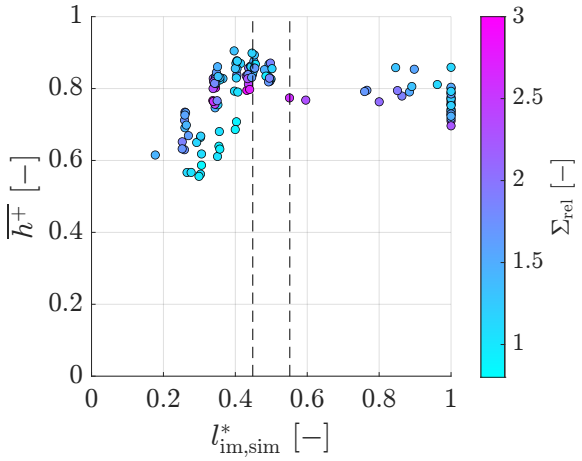

(a) $0.8 \leq \Sigma_{\mathrm{rel}} < 3$

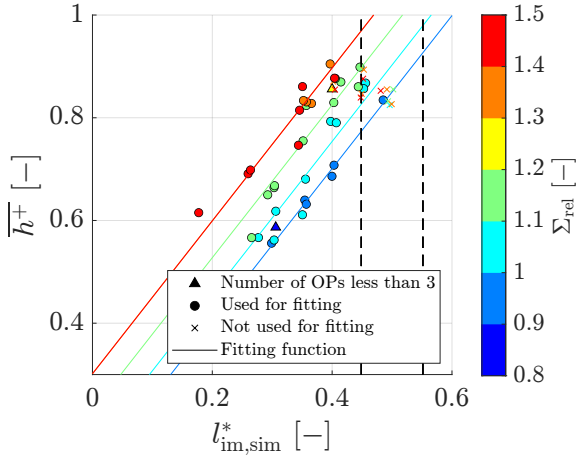

(b) $0.8 \leq \Sigma_{\mathrm{rel}} < 1.5$

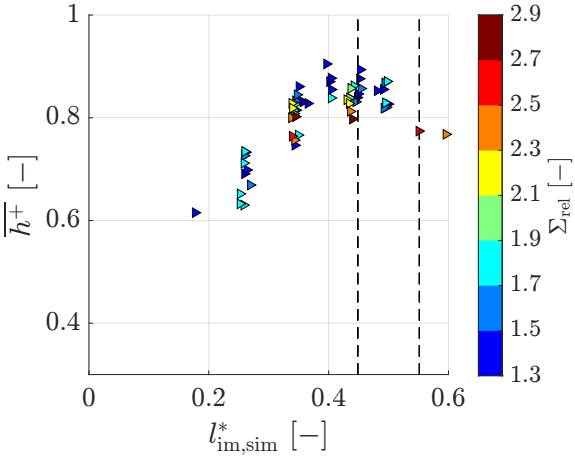

(c) $1.3 \leq \Sigma_{\mathrm{rel}} < 2.9$

Figure 5.10: Variation of normalised heat transfer coefficients with the normalised impingement lengths for OPs with $d_{\mathrm{jet}} = 0.64$ mm, with relative velocity ratio in colour scales.

$\overline{h^+}$ plot with the continuous Σ_{rel} scale is depicted in Figure 5.11a. As was the case with $d_{\mathrm{jet}} = 0.64$ mm, discrete sets of Σ_{rel} with a step size of 0.1 are required to characterise the influence of Σ_{rel}. The Σ_{rel} sets start with $0.85 \leq \Sigma_{\mathrm{rel}} < 0.95$ since the minimum value of Σ_{rel} is 0.85 for 0.82 mm $\leq d_{\mathrm{jet}} \leq$ 0.89 mm, and this division enables a more uniform grouping of these OPs. The zoomed-in plot for $0.85 \leq \Sigma_{\mathrm{rel}} < 1.55$ is depicted in Figure 5.11b. The fitting functions here are determined with the same slope as the OPs with $d_{\mathrm{jet}} = 0.64$ mm. The offset is adjusted for each Σ_{rel} set. The OP at $l^*_{\mathrm{im,sim}} \approx 0.09$ is marked as an outlier and excluded from function fitting. Furthermore, the OP with the maximum $\overline{h^+}$ of the $1.35 \leq \Sigma_{\mathrm{rel}} < 1.45$ set, located at $l^*_{\mathrm{im,sim}} \approx 0.4$, is excluded from function fitting since the trend of this Σ_{rel} set indicates that this OP is already beyond the linear region. The resulting offset values and coefficients of determination are listed in Table 5.3. The R^2 values are generally lower than the Σ_{rel} sets of the OPs with $d_{\mathrm{jet}} = 0.64$ mm. Nevertheless, the same augmenting effect of Σ_{rel} is apparent as the offset values increase with Σ_{rel}. The OPs with $1.3 \leq \Sigma_{\mathrm{rel}} < 2.9$ are plotted in Figure 5.11c

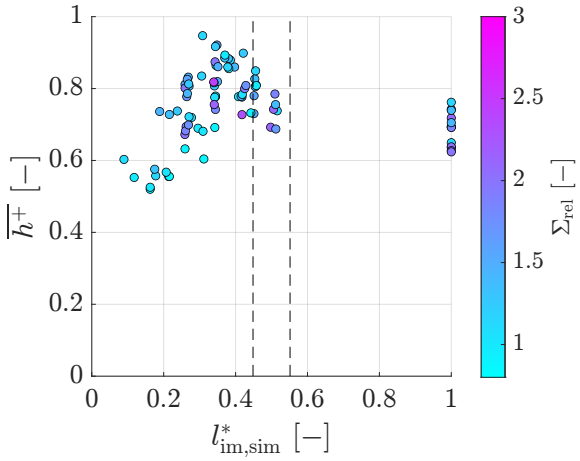

(a) $0.8 \leq \Sigma_{\mathrm{rel}} < 3$

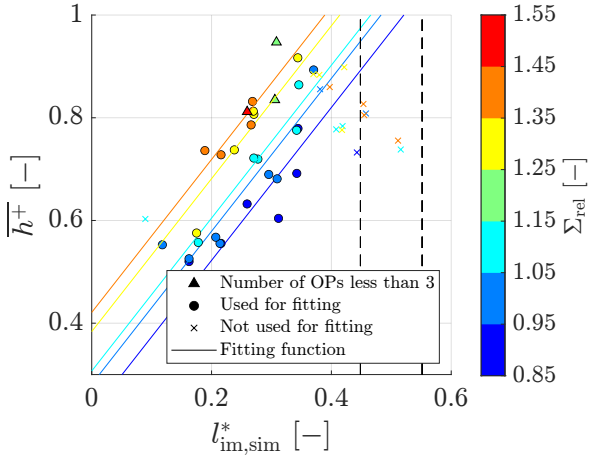

(b) $0.85 \leq \Sigma_{\mathrm{rel}} < 1.55$

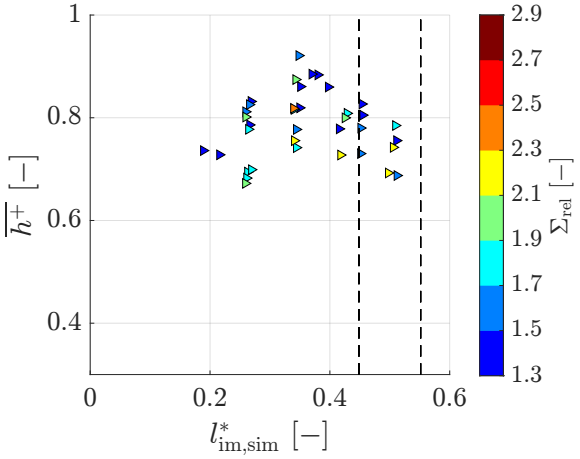

(c) $1.3 \leq \Sigma_{\mathrm{rel}} < 2.9$

Figure 5.11: Variation of normalised heat transfer coefficients with the normalised impingement lengths for OPs with 0.82 mm $\leq d_{\mathrm{jet}} \leq$ 0.89 mm, with relative velocity ratio in colour scales.

to investigate the reduction of Σ_{rel} effect at higher values. No positive effect is observed for $\Sigma_{\mathrm{rel}} > 1.3$, which is in line with the previous findings with the $d_{\mathrm{jet}} = 0.64$ mm OPs. Therefore, the effect of $\Sigma_{\mathrm{rel}} > 1.3$ will be capped at $\Sigma_{\mathrm{rel}} = 1.3$ in the empirical model. Comparing the fitting functions of the OP groups with different jet diameters reveals that the jet diameter has a similar effect as Σ_{rel}. The offset values of 0.82 mm $\leq d_{\mathrm{jet}} \leq$ 0.89 mm sets are higher than the comparable sets with $d_{\mathrm{jet}} = 0.64$ mm. Therefore, the jet diameter will also be considered a significant parameter in the model definition.

The spatial distribution of the heat transfer coefficient can also be investigated to support the findings based on the surface-averaged values. Seven OPs with Ψ and Σ_{rel} within a ±2.5% margin and $l^*_{\mathrm{im,sim}}$ varied between 0.3 and 1 are listed in Table 5.4. The respective heat transfer maps are shown in Figure 5.12 with the local heat transfer coefficient

$$h_{\mathrm{local}} = \frac{h}{\overline{h}}. \tag{5.18}$$

Table 5.3: Properties of fitting functions of Σ_{rel} sets of the OPs with 0.82 mm $\leq d_{\mathrm{jet}} \leq$ 0.89 mm. The slope is determined with the $0.9 \leq \Sigma_{\mathrm{rel}} < 1.0$ set of the OPs with $d_{\mathrm{jet}} = 0.64$ mm.

Σ_{rel} set	Slope	Offset	R^2
$0.85 \leq \Sigma_{\mathrm{rel}} < 0.95$	1.4885	0.2246	0.6814
$0.95 \leq \Sigma_{\mathrm{rel}} < 1.05$	1.4885	0.2813	0.8023
$1.05 \leq \Sigma_{\mathrm{rel}} < 1.15$	1.4885	0.3069	0.9243
$1.15 \leq \Sigma_{\mathrm{rel}} < 1.25$	-	-	-
$1.25 \leq \Sigma_{\mathrm{rel}} < 1.35$	1.4885	0.3837	0.9004
$1.35 \leq \Sigma_{\mathrm{rel}} < 1.45$	1.4885	0.4211	0.6502
$1.45 \leq \Sigma_{\mathrm{rel}} < 1.55$	-	-	-

Table 5.4: Selected OPs to investigate the influence of impingement length $0.3 \leq l^*_{\mathrm{sim}} \leq 1$.

	d_{jet} [mm]	ω [rad/s]	α [°]	u_{jet} [m/s]	$l^*_{\mathrm{im,sim}}$	Σ_{rel}	Ψ	$\overline{h^+}$
OP099	0.64	408.40	4	39.32	0.30	1.20	0.29	0.67
OP031	0.64	355.93	9	39.40	0.36	1.19	0.29	0.82
OP079	0.64	324.68	13	39.39	0.40	1.18	0.29	0.83
OP077	0.64	303.54	16	39.38	0.44	1.17	0.29	0.86
OP044	0.64	282.89	20	39.37	0.49	1.15	0.29	0.83
OP009	0.64	240.95	25	39.30	1	1.17	0.29	0.78
OP072	0.64	261.66	23	39.41	1	1.15	0.29	0.86

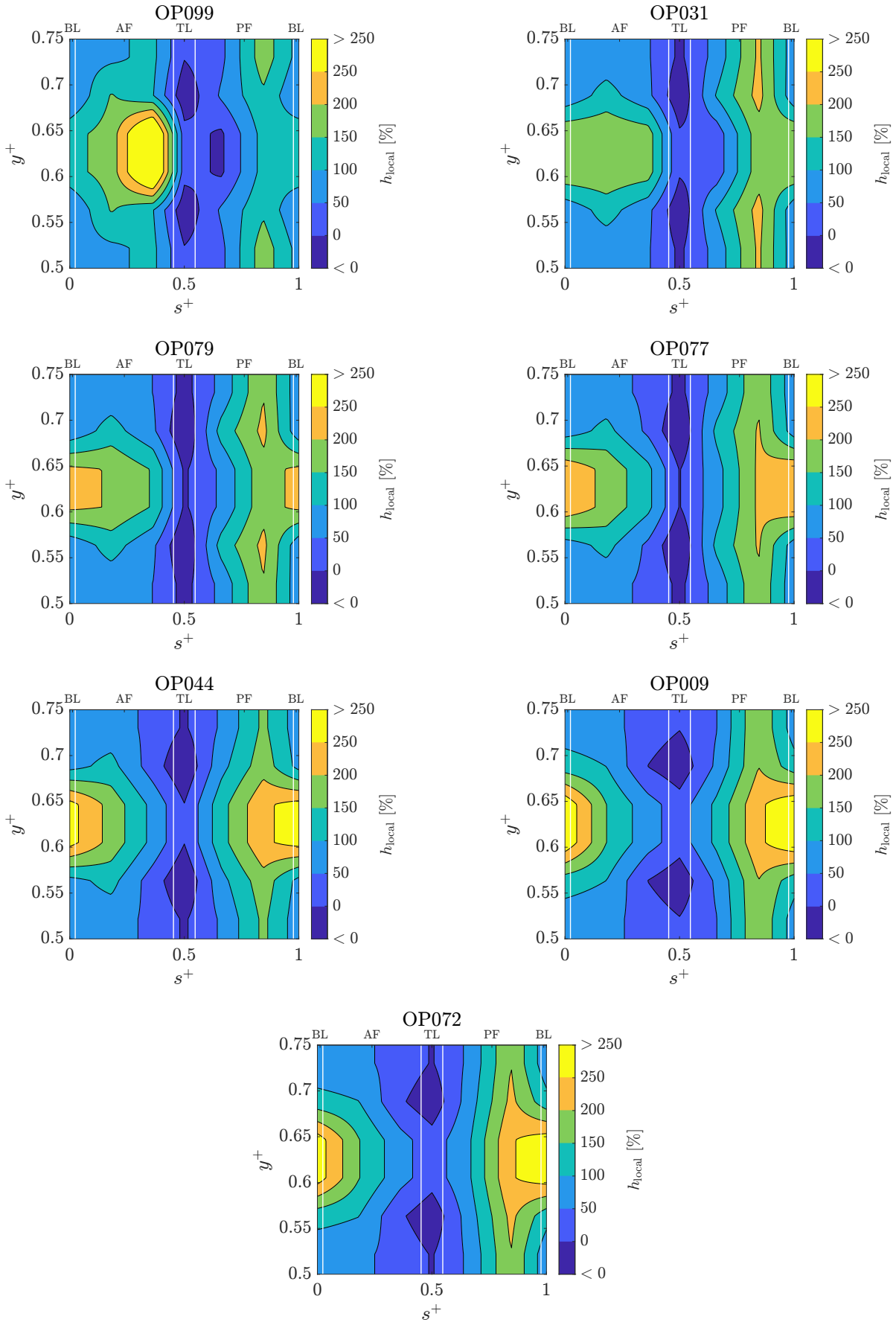

Figure 5.12: Heat transfer maps of OPs 099, 031, 079, 077, 044, 009 and 072.

OP099 exhibits the lowest impingement length out of the investigated OPs in Table 5.4 with $l^*_{\mathrm{im,sim}} = 0.3$. The heat transfer is mainly focused on the upper half of the active flank within $0.25 < s^+ < 0.5$. Nevertheless, other parts of the tooth surface are not deprived of oil. The passive flank has regions with $h_{\mathrm{local}} > 1$, indicating a considerable degree of wetting through either post-impingement propagation of the oil film or splashing. Even the slight increase of impingement length to $l^*_{\mathrm{im,sim}} = 0.36$ in OP031 significantly improves the uniformity of heat transfer. The passive flank experiences a similar, if not more pronounced, heat transfer as the active flank. The relative intensity around the bottomland increases at higher values of $l^*_{\mathrm{im,sim}}$. The heat transfer maps of OP009 and OP072 with direct impingement on the passive flank do not significantly differ from OP044 without any impingement on the passive flank. This information is vital for heat transfer modelling since it enables a straightforward inclusion of the OPs with $l^*_{\mathrm{im,sim}} = 1$ into the model.

A second group of OPs is selected to study lower values of $l^*_{\mathrm{im,sim}}$. The selected OPs are listed in Table 5.5, and their heat transfer maps are shown in Figure 5.13. For OP156 with $l^*_{\mathrm{im,sim}} = 0.19$, the heat transfer is more densely concentrated on the upper half of the active flank with sharp gradients towards the bottomland. The passive flank still has some wetting, whereas the region with $h_{\mathrm{local}} > 1$ is not continuous, as is the case with OP099, which signals that the oil on the passive flank is most likely generated by splashing. OP212 with $l^*_{\mathrm{im,sim}} = 0.27$ has a heat transfer map that is quite similar to that of OP099 with $l^*_{\mathrm{im,sim}} = 0.30$ despite the differences in Σ_{rel}, Ψ and d_{jet}. The same observations hold for OP138 ($l^*_{\mathrm{im,sim}} = 0.40$) and OP031 ($l^*_{\mathrm{im,sim}} = 0.36$).

Table 5.5: Selected OPs to investigate the influence of impingement length $0.19 \leq l^*_{\mathrm{sim}} \leq 0.40$.

	d_{jet} [mm]	ω [rad/s]	α [°]	u_{jet} [m/s]	$l^*_{\mathrm{im,sim}}$	Σ_{rel}	Ψ	$\overline{h^+}$
OP156	0.89	418.56	-26	34.73	0.19	1.43	0.50	0.74
OP212	0.89	335.13	-12	34.74	0.27	1.42	0.50	0.79
OP138	0.89	251.39	4	34.75	0.40	1.40	0.50	0.86

Analogously, the effect of Σ_{rel} can be visualised by means of the heat transfer maps. Three OPs with $\Psi = 0.27 \pm 2.5\%$, $l^*_{\mathrm{im,sim}} = 0.19 \pm 2.5\%$ and Σ_{rel} values of 0.86, 1.16 and 1.3 are listed in Table 5.6. For these OPs, $\overline{h^+}$ increases significantly with Σ_{rel}. The heat transfer maps in Figure 5.14 demonstrate why this is the case. The heat transfer is concentrated within the active flank in OP136. The heat transfer coefficient on the passive flank increases with Σ_{rel}, signalling that the oil is more evenly distributed on the tooth surface.

If the same comparison is carried out for OPs with $d_{\mathrm{jet}} = 0.64$ mm and $l^*_{\mathrm{im,sim}} = 0.45 \pm 2.5\%$, around which the maximum for $\overline{h^+}$ is located, an increase of Σ_{rel} does not necessarily result in higher heat transfer. Four OPs with $l^*_{\mathrm{im,sim}} = 0.45 \pm 2.5\%$ and $\Psi = 0.37 \pm 2.5\%$ and their heat transfer maps are given in Table 5.7 and Figure 5.15, respectively. No significant difference is observed between the heat transfer maps of OP112, OP108 and OP125 with Σ_{rel} values of 1.03, 1.32 and 1.65, respectively. The reason for this similarity could be that all OPs have an excellent wetting of both the active and passive flanks, similar to OPs 044, 009 and 072 in Figure 5.12.

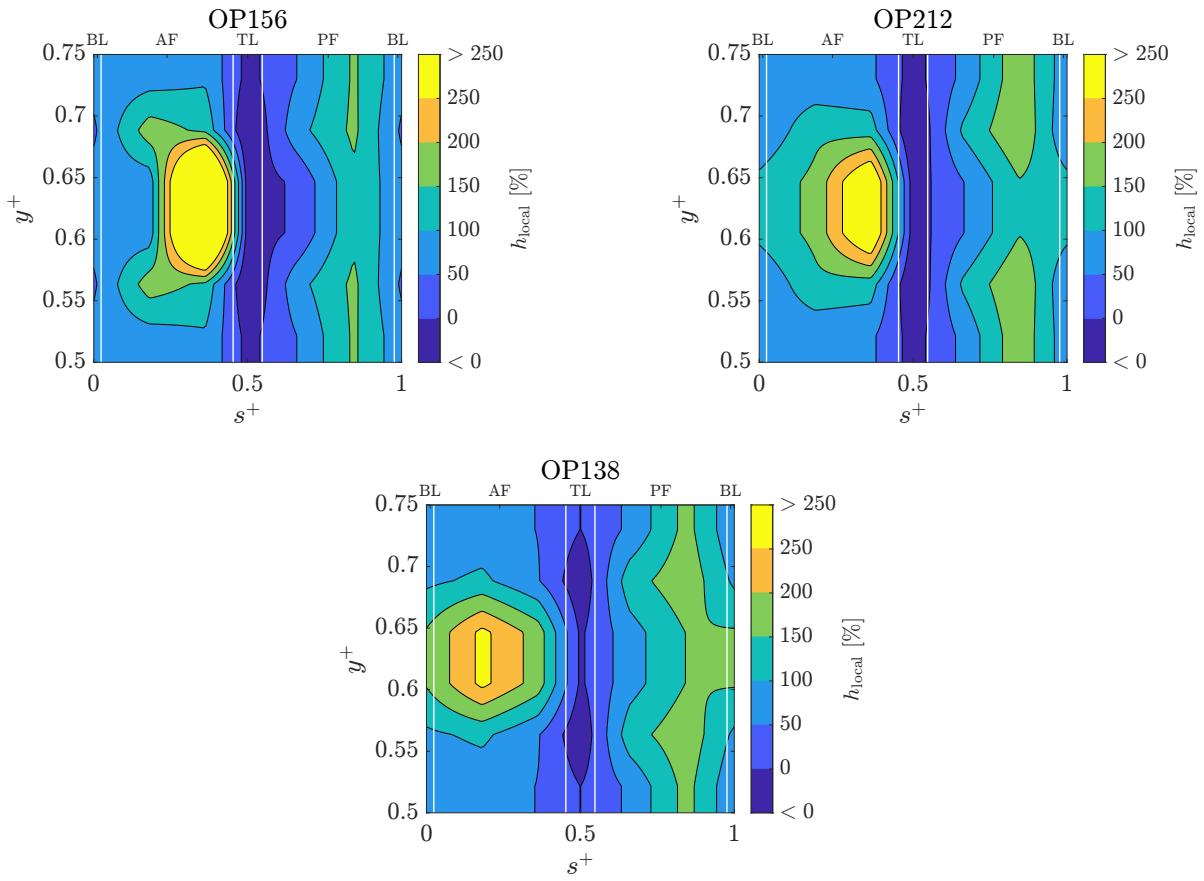

Figure 5.13: Heat transfer maps of OPs 156, 212 and 138.

Table 5.6: Selected OPs to investigate the influence of relative velocity ratio $0.86 \leq \Sigma_{\mathrm{rel}} \leq 1.30$.

	d_{jet} [mm]	ω [rad/s]	α [°]	u_{jet} [m/s]	$l^*_{\mathrm{im,sim}}$	Σ_{rel}	Ψ	$\overline{h^+}$
OP136	1.15	209.52	27	11.22	0.20	0.86	0.27	0.50
OP205	1.15	188.61	-7	11.22	0.19	1.16	0.27	0.57
OP134	1.15	159.94	-18	11.22	0.19	1.30	0.27	0.67

The heat transfer map of OP047 differs significantly from the others. The heat transfer intensity on the active flank, especially on the axial borders of the tooth quarter, is relatively low. Keller (2022) showed that some portion of the oil film detaches from the gear surface during its axial propagation and forms two ligaments moving axially and radially outwards. Increasing the relative velocity ratio could enhance the oil film detachment and lead to decreased wetting on the axial boundaries of the tooth quarter.

5.3.2 Model Definition

With the influence of individual significant parameters on the heat transfer identified, a suitable mathematical formulation should be found to define the empirical heat transfer model. The

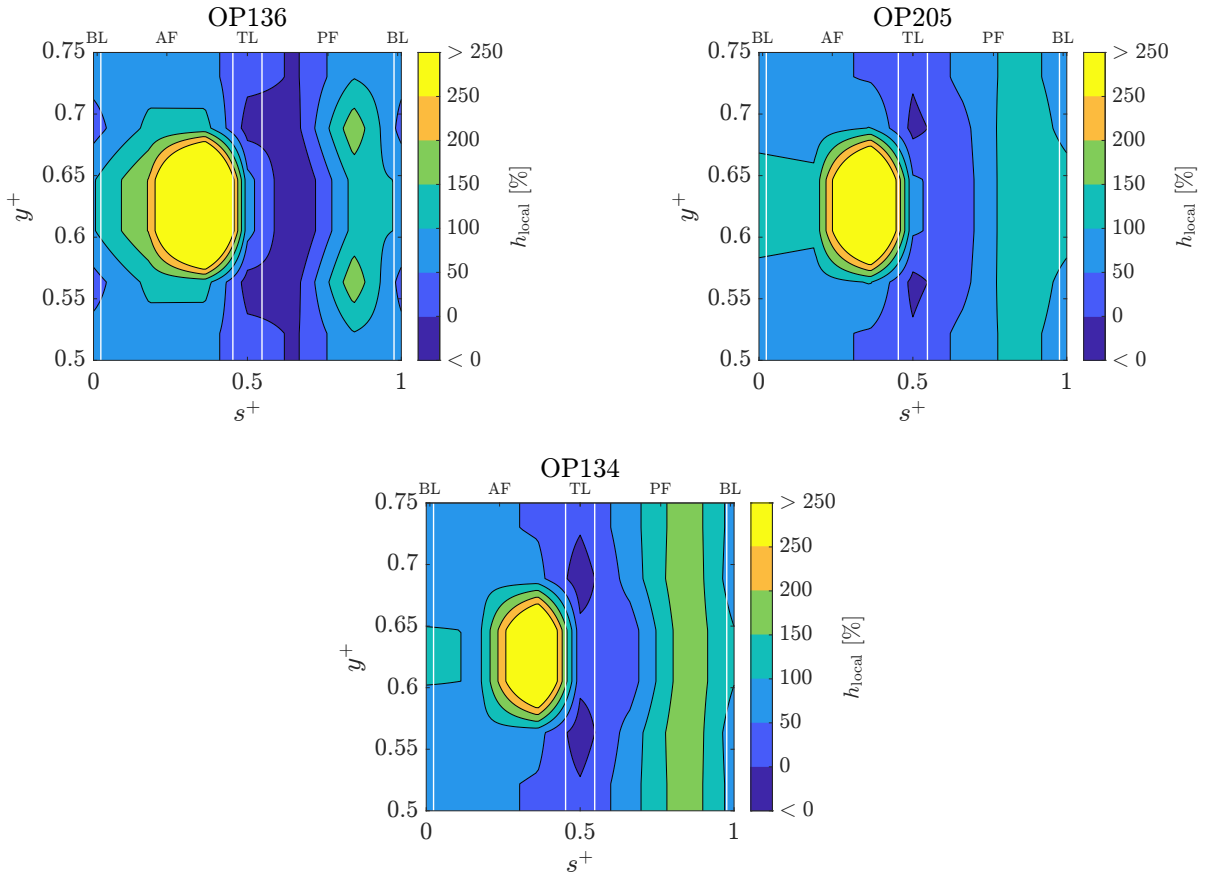

Figure 5.14: Heat transfer maps of OPs 136, 205 and 134.

Table 5.7: Selected OPs to investigate the influence of relative velocity ratio $1.03 \leq \Sigma_{\text{rel}} \leq 2.47$.

	d_{jet} [mm]	ω [rad/s]	α [°]	u_{jet} [m/s]	$l^*_{\text{im,sim}}$	Σ_{rel}	Ψ	$\overline{h^+}$
OP112	0.64	408.39	23	49.95	0.46	1.03	0.37	0.87
OP108	0.64	345.43	11	49.86	0.45	1.32	0.37	0.89
OP125	0.64	282.59	2	49.82	0.45	1.65	0.37	0.86
OP047	0.64	188.42	-12	49.79	0.44	2.47	0.37	0.81

influence of Ψ can be directly embedded into the model by using $\overline{h^+}$ as the target parameter, with C_{V} being a model parameter. The influence of Σ_{rel} will be implemented by modifying $l^*_{\text{im,sim}}$, similar to how the penetration depth differs from the impingement depth. The jet diameter has a similar effect as the relative velocity ratio. Both effects could be combined by using $\Sigma_{\text{rel}} d^*$ to represent the influence of inertial forces analogous to the numerator in Reynolds number with the normalised jet diameter

$$d^* = \frac{d_{\text{jet}}}{d_{\text{nozzle,J100}}}. \tag{5.19}$$

The effect of Σ_{rel} is shown to diminish for $\Sigma_{\text{rel}} > 1.3$. Therefore, Σ_{rel} will be capped at 1.3 in the model. For given values of Σ_{rel} and d^*, $\overline{h^+}$ increases quasi-linearly with $l^*_{\text{im,sim}}$, reaches a

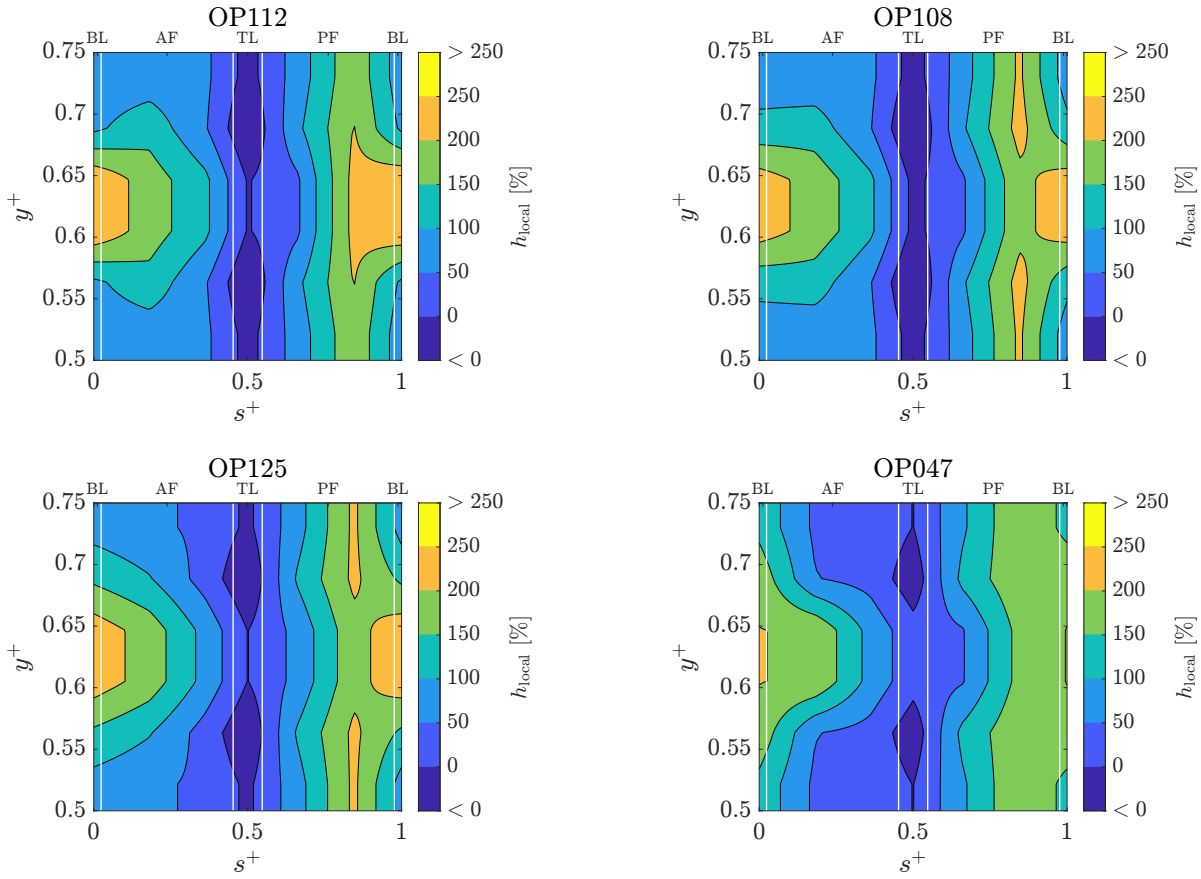

Figure 5.15: Heat transfer maps of OPs 112, 108, 125 and 047.

maximum value and starts to decline. A fitting function in the form of the probability density function of the log-normal distribution

$$f_{\mathrm{K}}(\kappa) = \frac{1}{\kappa\sigma_{\log}\sqrt{2\pi}}\exp\left(-\frac{(\ln(\kappa)-\mu_{\log})^2}{2\sigma_{\log}^2}\right), \tag{5.20}$$

can represent this trend. An increase of $l^*_{\mathrm{im,sim}}$ above a threshold does not significantly change the heat transfer. Therefore, all $l^*_{\mathrm{im,sim}}$ higher than 0.5515 can be set to $l^*_{\mathrm{im,sim}} = 0.5515$.

With all the conditions defined, the variable κ in Equation 5.20 can be substituted with the modified impingement length $l^*_{\mathrm{im,sim}}(\Sigma_{\mathrm{rel}}d^*)^{C_{\mathrm{Re}}}$, where C_{Re} is a model parameter. The parameters $\sigma_{\log}$ and $\mu_{\log}$ will also be renamed to C_σ and C_μ and be treated as model parameters. The integral of Equation 5.20 for $\kappa \in (0,\infty)$ will always be equal to 1 irrespective of the parameters σ and μ. This would not be true for the required fitting function. Therefore, the equation will be multiplied by another model parameter C_{m}. The surface-averaged heat transfer coefficient for $l^*_{\mathrm{im,sim}} \to 0$ would not necessarily be zero since a certain amount of wetting on the topland and its vicinity would be expected even if the impingement is very shallow. Therefore, an additional model parameter for the offset, C_{o}, is introduced. The finalised equation for the fitting function

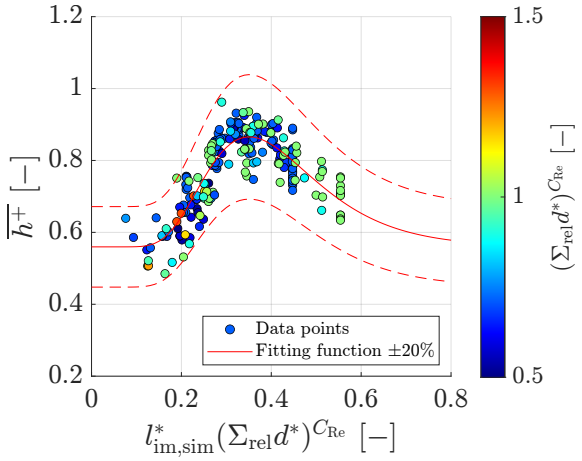

Figure 5.16: Fitting function for normalised heat transfer coefficient prediction.

is

$$\overline{h^+} = \frac{\overline{h}}{\overline{h}_{\max}\Psi^{C_{\mathrm{V}}}} = \left(\frac{1}{l^*_{\mathrm{im,sim}}(\Sigma_{\mathrm{rel}}d^*)^{C_{\mathrm{Re}}}C_\sigma\sqrt{2\pi}}\exp\left(-\frac{(\ln(l^*_{\mathrm{im,sim}}(\Sigma_{\mathrm{rel}}d^*)^{C_{\mathrm{Re}}}) - C_\mu)^2}{2C_\sigma^2}\right)\right)C_{\mathrm{m}} + C_{\mathrm{o}}. \tag{5.21}$$

The non-linear regression fitting is carried out using the *fitnlm* function of MATLAB (2021), which utilises the Levenberg-Marquardt non-linear least squares algorithm. The resulting model parameters are $C_{\mathrm{V}} = 0.8641$, $C_{\mathrm{Re}} = 0.6310$, $C_\sigma = 0.3484$, $C_\mu = -0.9260$, $C_{\mathrm{m}} = 0.0996$ and $C_{\mathrm{o}} = 0.5597$. The constant C_{V} is remarkably close to the previous calculation with a limited number of OPs. C_{Re} suggests that the inertial forces of the oil jet impingement augment the wetting by a factor of nearly $(\Sigma_{\mathrm{rel}}d^*)^{\frac{2}{3}}$. The fitting function and a range of ±20% are depicted in Figure 5.16. The model can accurately predict $\overline{h^+}$ of the optimal test matrix OPs within a ±20% margin. The coefficient of determination is $R^2 = 0.9556$, and the standard deviation of residuals is $\sigma_{\mathrm{res}} = 0.0432$. However, neither is a suitable benchmark for testing the model's performance since it is trained and tested on the same dataset. The initial test matrix also cannot be used to test the model since the calibration of thermocouples renders the results incomparable.

A 5-fold cross-validation scheme is undertaken to overcome this problem. The dataset is randomly separated into five groups. The model is trained with four groups and applied to the fifth group to generate predictions. The predicted values for this test group are compared to the measured ones to assess the model's performance. This procedure is repeated five times by changing the test group in each iteration. Coefficient of determination is used to score the model's performance in training and test datasets. The model parameters and coefficients of determination are listed in Table 5.8. Each fold results in similar scores for the training and test subsets, suggesting that the model would accurately predict the heat transfer coefficient within its parameter space. The predicted and measured heat transfer coefficients for each fold are depicted in Figure 5.17. The model parameters and, therefore, the predictions change only slightly in each fold. This also supports the claim that the model is not over-fitted to the available data points and has an outstanding prediction capability within the investigated parameter space.

Table 5.8: Model parameters and coefficient of determination (R^2) for the training and test groups.

	Model	Fold 1	Fold 2	Fold 3	Fold 4	Fold 5
R^2_{training}	0.9556	0.9610	0.9556	0.9523	0.9563	0.9542
R^2_{test}	-	0.9326	0.9522	0.9682	0.9493	0.9565
C_{V}	0.8641	0.8625	0.8659	0.8637	0.8530	0.8784
C_{Re}	0.6310	0.6096	0.6657	0.6435	0.6057	0.6297
C_{σ}	0.3484	0.3676	0.3319	0.3486	0.3647	0.3268
C_{μ}	–0.9260	–0.9074	–0.9463	–0.9287	–0.8988	–0.9489
C_{m}	0.0996	0.1142	0.0889	0.1026	0.1028	0.0895
C_{o}	0.5597	0.5371	0.5768	0.5503	0.5549	0.5835

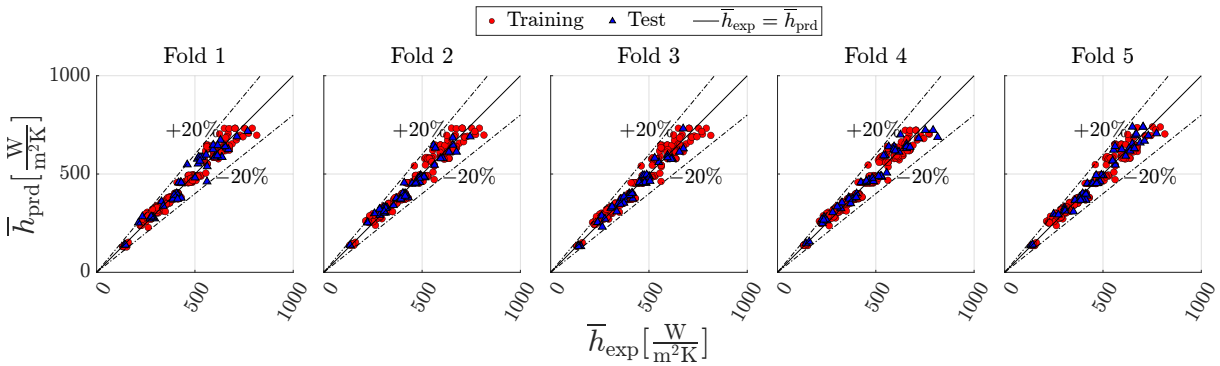

Figure 5.17: Predicted and measured heat transfer coefficients of training and test groups in each fold.

5.3.3 Wetted Area and Heat Transfer

The experimental investigation of the oil jet gear interaction is extremely challenging. With the current experimental setup, it is infeasible to quantitatively determine the maximum wetted area $A_{\text{F,max}}$, which could potentially be a deciding parameter to predict the heat transfer coefficient. The simulations of Keller (2022) deliver relevant insights into the flow phenomenology and determine $A_{\text{F,max}}$ for 21 OPs (Table 5.9), albeit without the heat transfer. None of the numerical OPs can be experimentally tested with the existing hardware since the jet diameters and velocities in attached and separated regimes do not match up or the rotational speeds would be too high. However, their $l^*_{\text{im,sim}}$ and $\Sigma_{\text{rel}} d^*$ values are still within the training parameter space of the heat transfer model. Fourteen of the Ψ values are higher than the maximum value of the optimal test matrix $\Psi_{\text{max}} = 0.5807$. Eleven of these are within +6% of Ψ_{max}, whereas $\Psi = 1.56\Psi_{\text{max}}$ for OPs C and K, and $\Psi = 2.07\Psi_{\text{max}}$ for F. Nevertheless, the newly developed heat transfer model is applied to these numerical OPs to predict the surface-averaged heat transfer coefficient and investigate how well it is correlated with wetting. OPs P and U with $\alpha_{\text{eff}} = \pm 90°$ result in $l^*_{\text{im,sim}} = 0$ and are, therefore, excluded from the analysis.

Table 5.9: OPs numerically investigated by Keller (2022).

	d_{jet} [mm]	ω [rad/s]	α [°]	u_{jet} [m/s]	$l^*_{\mathrm{im,sim}}$	Σ_{rel}	Ψ	$\overline{h^+}_{\mathrm{prd}}$	$A^*_{\mathrm{F,max}}$
A	1.00	510.51	0.00	16.59	0.12	1.03	0.30	0.56	0.20
B	1.00	510.51	0.00	33.18	0.22	1.12	0.61	0.67	0.36
C	1.00	510.51	0.00	49.77	0.29	1.25	0.91	0.85	0.65
D	1.41	510.51	0.00	16.59	0.12	1.03	0.60	0.57	0.21
E	0.82	510.51	0.00	33.18	0.22	1.12	0.41	0.62	0.29
F	1.41	510.51	0.00	33.18	0.22	1.12	1.20	0.78	0.51
G	0.82	510.51	0.00	49.77	0.29	1.25	0.61	0.80	0.49
H	1.00	255.25	0.00	16.59	0.22	1.12	0.30	0.67	0.32
I	1.41	255.25	0.00	16.59	0.22	1.12	0.60	0.78	0.51
J	0.82	765.76	0.00	49.77	0.22	1.12	0.61	0.62	0.30
K	1.00	765.76	0.00	49.77	0.22	1.12	0.91	0.67	0.40
L	1.00	510.51	–21.80	16.59	0.10	1.13	0.30	0.56	0.12
M	1.00	510.51	10.70	16.59	0.12	0.98	0.30	0.56	0.19
N	1.00	510.51	21.80	16.59	0.12	0.92	0.30	0.56	0.21
O	1.00	510.51	33.86	16.59	0.11	0.86	0.30	0.56	0.22
P	1.00	510.51	–68.21	33.18	0	1.52	0.61	-	0.16
Q	1.00	510.51	–21.80	33.18	0.17	1.29	0.61	0.62	0.32
R	1.00	510.51	10.70	33.18	0.23	1.02	0.61	0.67	0.36
S	1.00	510.51	21.80	33.18	0.24	0.91	0.61	0.66	0.36
T	1.00	510.51	33.86	33.18	0.24	0.79	0.61	0.62	0.39
U	1.00	510.51	68.21	33.18	0	0.44	0.61	-	0.23

The normalised wetted area

$$A^*_{\mathrm{F,max}} = \frac{A_{\mathrm{F,max}}}{A_{\mathrm{Fl}}}, \tag{5.22}$$

where A_{Fl} is a quarter of the total gear flank area, is plotted against the predicted normalised heat transfer coefficient $\overline{h^+}_{\mathrm{prd}}$ in Figure 5.18. The wetted area and $\overline{h^+}_{\mathrm{prd}}$ correlate very well with a coefficient of determination of $R^2 = 0.9615$, which suggests that the wetted area is indeed a key parameter to assess and potentially predict the heat transfer coefficient.

Applying the empirical heat transfer model to varying gear geometries, e.g. helical gears, would require adjustments to the model and, therefore, additional measurements with the new geometry. The experimental setup should be modified for these measurements, and a completely new instrumentation is necessary. These adjustments to the experimental setup and the conduction of new measurements would be very costly and time-consuming. However, if the wetted area is, in fact, a key metric for heat transfer, it could be in the interest of a cooling system designer to deploy a fast and accurate approach to determine wetted areas for differing geometries. In his Bachelor's thesis, Geißendörfer (2021) modified the numerical setup of Keller (2022) to decrease

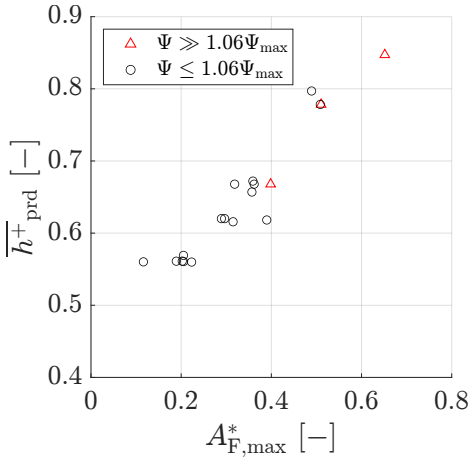

Figure 5.18: Predicted normalised heat transfer coefficients and the normalised wetted areas of OPs numerically investigated by Keller (2022).

the computational time required to simulate the oil jet gear interaction. The results showed very good agreement with those of Keller (2022), with the computation time being reduced on average to one-sixth. Nassef (2022) adjusted two analytical wetting models in his Master's thesis, the so-called momentum balance and droplet spread models, to predict the wetted area. The results of Keller (2022) were used to validate the models. Both methods showed potential, but neither was perfectly accurate across the parameter space. Further development of these approaches should be the focus of future research since they could enable an indirect application of the novel empirical heat transfer model to differing gear geometries by correlating the heat transfer coefficient with the wetted area.

5.3.4 Optimisation Scenarios

The model's prediction capability can be deployed in an optimisation study to find the best possible cooling solution within given boundaries. The optimisation algorithm should provide the operational parameters that result in optimal cooling. To do that, Equation 5.17 is to be parametrised with respect to the operational parameters, which is impossible with the oil jet tip simulation method. The vectorial model is in very good agreement with the simulation method for $l^*_{\mathrm{im,max}} < 0.5515$, as depicted in Figure 5.5a. The vectorial model can be applied instead of the simulation method since the maximum normalised impingement length is limited to $l^*_{\mathrm{im,max}} = 0.5515$. Once the optimal OP is found with $l^*_{\mathrm{im,vectorial}}$, the predicted heat transfer coefficient can be recalculated with $l^*_{\mathrm{im,sim}}$ for the respective OP.

Various optimisation scenarios will be discussed in the following. In her Master's thesis on thermal modelling of the sun gear, Bauer (2018) presents two exemplary OPs derived from realistic jet engine conditions at take-off. It will be assumed that both OPs belong to different flight phases of the same geared turbofan engine. The validity of the OPs for the actual geared turbofan application is irrelevant to the optimisation demonstration. The selected flight OPs, FP1 and FP2, are listed in Table 5.10.

Table 5.10: Selected flight operating points for optimisation discussion.

	T_{oil} [°C]	α [°]	$\dot{V}_{\text{oil}}$ [l/min]	ω [rad/s]
FP1	80	20	7.2	216.35
FP2	80	20	10.4	396.15

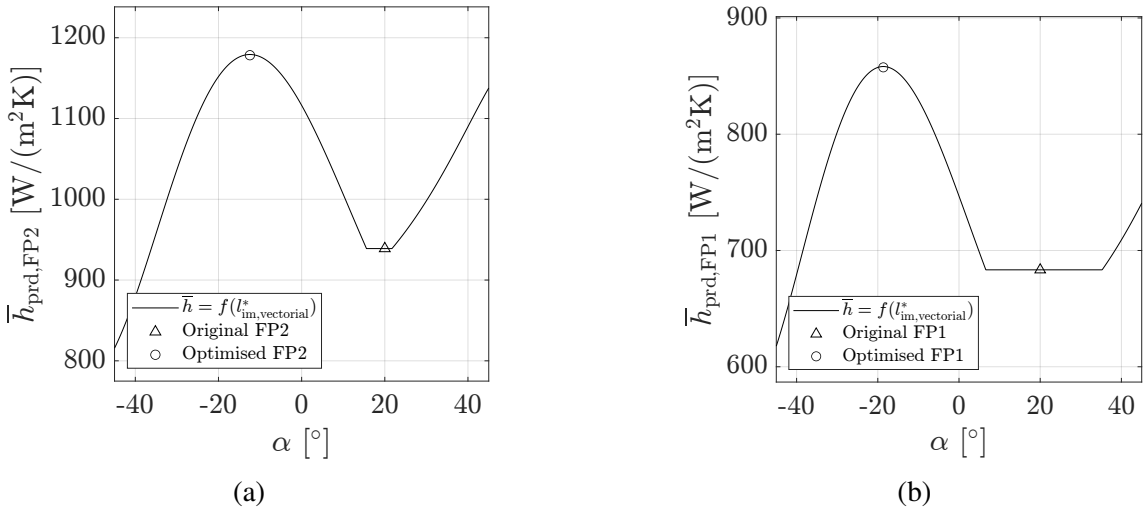

(a) (b)

Figure 5.19: Optimisation of the jet inclination angle to maximise heat transfer coefficients of only FP2 (a) and only FP1 (b).

In the first two scenarios, the oil jet is generated by the spraybar J100, as in the original case investigated by Bauer (2018). It is assumed that ω and $\dot{V}_{\text{oil}}$ are invariable constants set as boundary conditions. The main goal of the optimisation is to find the optimal design variable $\alpha \in [-45°, 45°]$, which cannot be changed during the flight.

The first scenario prioritises FP2 absolutely and tries to maximise its heat transfer without regard to FP1. The change of $\overline{h}_{\text{prd}}$, calculated with $l^*_{\text{im,vectorial}}$, in relation to α, is depicted in Figure 5.19a, together with the original and optimised FP2, for which $\overline{h}_{\text{prd}}$ are recalculated with $l^*_{\text{im,sim}}$. Changing α from 20° to −12.44° increases $\overline{h}_{\text{prd}}$ by 25.5%. The change of jet inclination benefits FP1 similarly and increases its $\overline{h}_{\text{prd}}$ by 22.24%. The second scenario is the opposite of the first one and only focuses on FP1. The maximum for $\overline{h}_{\text{prd}}$ is found at $\alpha = -18.65°$ (Figure 5.19b). The increase in $\overline{h}_{\text{prd}}$ is 25.49% and 24.38% for FP1 and FP2, respectively.

The third scenario assumes that the jet diameter d_{jet} is also a design variable while keeping the number of jets constant. The lower bound for d_{jet} is assumed to be 0.5 mm, whereas an upper bound of 2 mm is set. The optimisation aims to maximise $\overline{h}_{\text{prd}}$ of FP2, similar to the first scenario. $\overline{h}_{\text{prd}}$ is depicted as a contour plot in Figure 5.20a. A contour with a maximum heat transfer coefficient with interdependent d_{jet} and α is observed. Additional design criteria can be agreed upon to determine the desired combination of d_{jet} and α. For example, decreasing the size of the jet at a given volume flow ratio requires an increase in the oil pressure and velocity. This requires higher specifications of the oil system and increases the losses caused by the impinging oil jet. Depending on the selected jet diameter, the oil jet might be directed against the rotational

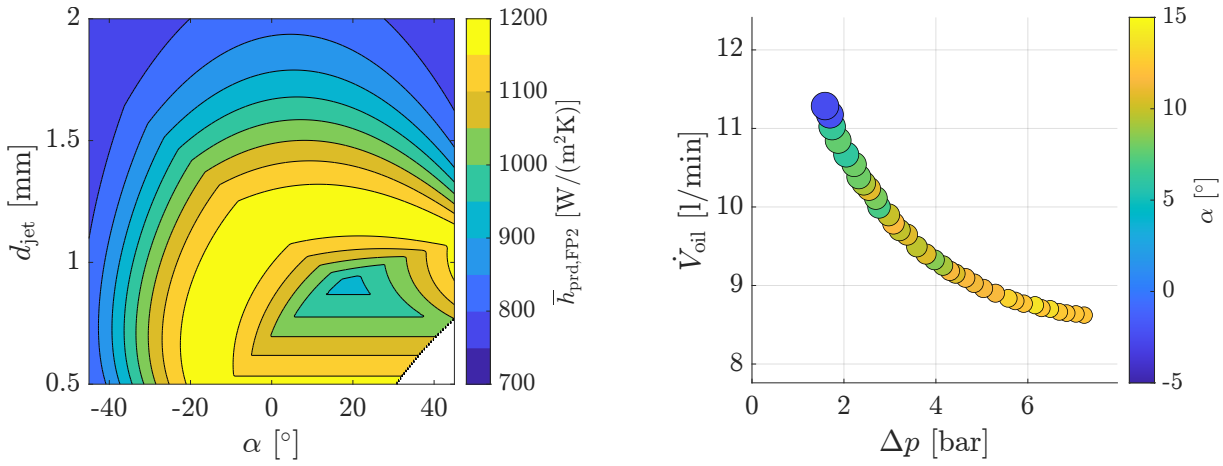

(a) (b)

Figure 5.20: Predicted heat transfer coefficient contours for FP2 with variable jet diameter and inclination angle (a) and Pareto front for oil volume flow rate and pressure difference while ensuring minimum heat transfer coefficients of 750 W/(m^{2}K) and 1000 W/(m^{2}K) for FP1 and FP2, respectively (b).

direction of the gear if the maximum possible heat transfer coefficient is desired. This, in turn, augments the losses even more. Therefore, the wiser design choice for FP2 would be to select a combination of relatively high d_{jet} and α values within the maximum heat transfer coefficient contour.

Last but not least, the fourth scenario will entirely focus on the efficiency of the oil system while keeping $\overline{h}_{prd}$ above arbitrary levels of 750 W/(m^{2}K) and 1000 W/(m^{2}K) for FP1 and FP2, respectively. $\dot{V}_{oil}$ is also a design parameter which does not vary between FP1 and FP2. The goals of the optimisation are to minimise the oil volume flow rate $\dot{V}_{oil}$ and the oil pressure Δp since they are the deciding factors for the dimensions of the oil system. Oil jet diameter and oil jet angle are the optimisation variables. The required oil pressure Δp is calculated via Equation 4.2, assuming $C_c = C_d = 0.6$ for all $\dot{V}_{nozzle}$ and d_{jet}. Figure 5.20b depicts the resulting Pareto front fulfilling the heat transfer coefficient requirement with α shown in the colour scale and d_{jet} shown qualitatively via the marker size. The required oil pressure can be lowered by utilising a relatively large nozzle, increasing the oil volume flow rate and decreasing the oil jet angle. The operational parameters at this end of the Pareto front are $\dot{V}_{oil} = 11.29$ l/min, $\Delta p = 1.59$ bar, $d_{jet} = 1.81$ mm and $\alpha = -2.48°$. The other end of the Pareto front has operational parameters of $\dot{V}_{oil} = 8.62$ l/min, $\Delta p = 7.23$ bar, $d_{jet} = 1.08$ mm and $\alpha = 12.19°$. The designer can decide on a pair of volume flow rate and oil pressure, taking additional factors such as oil deflection and oil trapping losses into consideration.

6 Summary and Outlook

High-speed high-load gearboxes are projected to play a pivotal role in the future of jet engines and the aviation industry. A crucial aspect that has not been extensively studied but holds significant importance is the oil jet cooling of the gears. Due to the scarcity of data to model the heat transfer, the design of the cooling systems has largely relied on educated estimates of experts and iterative improvements.

This work aimed to improve these circumstances by characterising the significant parameters that affect the heat transfer and by quantifying their influences. To this end, the heat transfer between the impinging oil jets and the rotating gear was experimentally investigated. The existing experimental setup and the iterative evaluation approach were improved and validated using numerical reference cases. A novel calibration scheme was employed to increase the temperature measurement accuracy of the test rig significantly.

The nozzle flow was investigated to explain the separation of oil flow from the nozzle walls. Comparing the novel experimental results to the available data in the literature revealed that the flow separation can be attributed to the so-called hydraulic flip. A numerical study was conducted to simulate a cavitating nozzle, complementing the experiments. The results were in excellent agreement with the experiments, supporting the hydraulic flip hypothesis.

An initial test matrix was employed to conduct measurements at varying operational parameters, including the oil volume flow rate, the rotational speed of the gear, the jet inclination angle, the number of nozzles and the nozzle diameter. These initial measurements were used to characterise significant parameters, combining distinct operational parameters' influence on the surface-averaged heat transfer coefficient. The significant parameters determined were the volume flow ratio, the impingement length and the relative velocity ratio. The volume flow ratio had a linear influence on the surface-averaged heat transfer coefficient. If all other operational parameters were kept constant, doubling the volume flow rate resulted in approximately double the original surface-averaged heat transfer coefficient. Therefore, the heat transfer coefficient was normalised with the volume flow ratio to investigate the remaining significant parameters. The normalised heat transfer coefficient initially increased with the impingement length but reached a maximum around the point where the bottomland started being impinged upon by the oil jet. The relative velocity ratio generally enhanced the heat transfer. However, the conclusions on the individual influences were only qualitative, especially for the last two significant parameters. An optimal test matrix was generated, which resolved the available parameter space spanned by the significant parameters in a more homogenous and generalisable way. The influence of the impingement length was captured more clearly. A consistent trend was apparent: an initial linear increase in the normalised heat transfer coefficient was observed for increasing impingement lengths. After reaching a maximum, the normalised heat transfer coefficient declined slightly. This trend was observed at different relative velocity ratios and for different jet diameters. However, changes in the relative velocity ratio or the jet diameter affected the normalised heat transfer coefficient variation over the impingement length. The maximum heat transfer coefficient was reached at a lower impingement length if either the relative velocity ratio or the jet diameter was increased. The effect of the relative velocity ratio diminished for values

higher than 1.3. Analogous to the difference between the penetration and impingement depths, a new parameter was defined, which included the impingement depth, the relative velocity ratio and the jet diameter. The probability density function of log-normal distribution was selected as a suitable function to fit the surface-averaged heat transfer coefficient as the target parameter. The prediction capabilities of the model were tested by employing a 5-fold cross-validation scheme. The prediction scores for training and test datasets were very high and comparable, suggesting that the model is generalisable and does not overfit the available dataset. Predicted heat transfer coefficients were calculated for simulated cases from the literature. The heat transfer coefficients correlated very well with the numerically determined wetted areas. The capabilities of the heat transfer model were showcased by employing various optimisation scenarios.

The introduction of this work included a quote from 1966, stating that many questions about the optimal oil jet cooling design were unanswered at that time. Most of these questions were either not addressed or only partially answered in the 59 years since then. This work aimed to give insights into each key parameter's influence, if not define it quantitatively. The novel empirical heat transfer model is a capable tool that can immensely support engineers in the preliminary gearbox design phases. However, there are still numerous aspects to improve and many questions to answer. The heat transfer coefficients in this work were mostly reported as dimensionless figures to prevent direct application of the numbers in a design process since the heat transfer coefficients were defined using the nozzle temperature as the reference temperature. A better, more generalisable way would be to employ the adiabatic wall temperature instead. However, modifying the experimental setup to capture the required data to characterise the adiabatic wall temperature was not feasible. Furthermore, the experimental setup can only simulate a simplified version of the gear cooling in the context of a geared turbofan. The most obvious challenge for the transferability of the results is the different types of gears. A high-speed high-load gearbox would not employ spur gears, as was the case in this work. A possible means of overcoming this challenge can be further research regarding wetted areas. The predicted heat transfer coefficients of the numerical cases by Keller (2022) showed that the wetted area could accurately predict the heat transfer coefficient. The need for cumbersome and expensive experiments specific to an individual geometry could be decreased if an inexpensive way to predict the wetting of the gear, analytically or numerically, was developed.

Bibliography

Abderrezzak, B. and Huang, Y. (2017). „Investigation of the Effect of Cavitation in Nozzles With Different Length to Diameter Ratios on Atomization of a Liquid Jet“. In: *Journal of Thermal Science and Engineering Applications*, Band 9, Heft 3, p. 031014. ISSN: 1948-5085. DOI: 10.1115/1.4036438.

Air Transport Action Group (2021). *Waypoint 2050*. Accessed on 02.03.2023. URL: https://aviationbenefits.org/media/167417/w2050_v2021_27sept_full.pdf.

Akin, L. S. and Mross, J. J. (1975). „Theory for the Effect of Windage on the Lubricant Flow in the Tooth Spaces of Spur Gears“. In: *Journal of Engineering for Industry*, Band 97, Heft 4, pp. 1266–1272. ISSN: 00220817. DOI: 10.1115/1.3438742.

Akin, L. S., Mross, J. J., and Townsend, D. P. (1975). „Study of Lubricant Jet Flow Phenomena in Spur Gears“. In: *Journal of Lubrication Technology*, Band 97, Heft 2, pp. 283–288. ISSN: 0022-2305. DOI: 10.1115/1.3452576.

Akin, L. S. and Townsend, D. P. (1983a). „Into Mesh Lubrication of Spur Gears With Arbitrary Offset Oil Jet. Part 1: For Jet Velocity Less Than or Equal to Gear Velocity“. In: *Journal of Mechanisms, Transmissions, and Automation in Design*, Band 105, Heft 4, pp. 713–718. ISSN: 0738-0666. DOI: 10.1115/1.3258541.

Akin, L. S. and Townsend, D. P. (1983b). „Into Mesh Lubrication of Spur Gears With Arbitrary Offset Oil Jet. Part 2: For Jet Velocities Equal to or Greater Than Gear Velocity“. In: *Journal of Mechanisms, Transmissions, and Automation in Design*, Band 105, Heft 4, pp. 719–724. ISSN: 0738-0666. DOI: 10.1115/1.3258542.

Akin, L. S. and Townsend, D. P. (1985). „Lubricant Jet Flow Phenomena in Spur and Helical Gears With Modified Center Distances and/or Addendums—For Out-of-Mesh Conditions“. In: *Journal of Mechanisms, Transmissions, and Automation in Design*, Band 107, Heft 1, p. 24. ISSN: 0738-0666. DOI: 10.1115/1.3258686.

Akin, L. S. and Townsend, D. P. (1989). „Lubricant Jet Flow Phenomena in Spur and Helical Gears with Modified Addendums - for Radially Directed Individual Jets“. In: *Fifth International Power Transmission and Gearing Conference, Chicago, IL, United States, April 25-28*.

ANSYS (2019). *Fluent Theory Guide 2019 R3*.

Ayan, E., Kromer, C., Schwitzke, C., and Bauer, H. J. (2022a). „Experimental investigation of the oil jet heat transfer on meshing spur gears“. In: *25th Conference of the International Society of Air Breathing Engines (ISABE 2022), Ottawa, Canada, September 25-30*. DOI: 10.5445/IR/1000151853.

Ayan, E., Kromer, C., Schwitzke, C., and Bauer, H. J. (2024). „Heat transfer on impingement cooled meshing spur gears: Experimental comparison of into-mesh, out-of-mesh and inclined impingement methods“. In: *Heat and Mass Transfer*. ISSN: 1432-1181. DOI: 10.1007/s00231-024-03464-1.

Ayan, E., von Plehwe, F. C., Keller, M. C., Kromer, C., Schwitzke, C., and Bauer, H. J. (2022b). „Experimental Determination of Heat Transfer Coefficient on Impingement Cooled Gear Flanks: Validation of the Evaluation Method“. In: *Journal of Turbomachinery*, Band 144, Heft 8, p. 229. ISSN: 0889-504X. DOI: 10.1115/1.4053694.

Bauer, F. (2018). *Thermalmodellierung des Sonnenrades eines Hochleistungsplanetengetriebes mit Öleinspritzkühlung*. Master's thesis. Supervisor: Prof. Hans-Jörg Bauer, Co-supervisors: Dipl.-Ing. Felix v. Plehwe.

El-Bayoumy, L. E., Akin, L. S., Townsend, D. P., and Choy, F. C. (1989). *The Role of Thermal and Lubricant Boundary Layers in the Transient Thermal Analysis of Spur Gears*. NASA Technical Memorandum ADA205574. Cleveland, Ohio: Lewis Research Center.

Beuerlein, P. (1954). *Kröners Taschenbuch der Maschinentechnik 1: Grundlagen - Grenzgebiete: Schmiertechnik*. Stuttgart: Alfred Kröner Verlag.

COMSOL AB (2019). *COMSOL Multiphysics® v. 5.5*. Stockholm, Sweden.

Cordes, L. (2021). „Über das Durchflussverhalten von Flüssigkeiten durch radiale Wellenbohrungen in einen Ringspalt". PhD thesis. Karlsruher Institut für Technologie (KIT). DOI: 10.5445/IR/1000139999.

DeWinter, A. and Blok, H. (1974). „Fling-Off Cooling of Gear Teeth". In: *Journal of Engineering for Industry*, Band 96, Heft 1, p. 60. ISSN: 00220817. DOI: 10.1115/1.3438331.

DIN e.V. (2014). *DIN EN 60584-1:2014-07: Thermoelemente – Teil 1: Thermospannungen und Grenzabweichungen*. Berlin.

Fernandes, C. M. C. G., Rocha, D. M. P., Martins, R. C., Magalhães, L., and Seabra, J. H. O. (2018). „Finite element method model to predict bulk and flash temperatures on polymer gears". In: *Tribology International*, Band 120, pp. 255–268. ISSN: 0301679X. DOI: 10.1016/j.triboint.2017.12.027.

Fondelli, T., Andreini, A., Da Soghe, R., Facchini, B., and Cipolla, L. (2015). „Numerical Simulation of Oil Jet Lubrication for High Speed Gears". In: *International Journal of Aerospace Engineering*, Band 2015, Heft 3, pp. 1–13. ISSN: 1687-5966. DOI: 10.1155/2015/752457.

Gan, L., Xiao, K., Wang, J., Pu, W., and Cao, W. (2019). „A numerical method to investigate the temperature behavior of spiral bevel gears under mixed lubrication condition". In: *Applied Thermal Engineering*, Band 147, pp. 866–875. ISSN: 13594311. DOI: 10.1016/j.applthermaleng.2018.10.125.

Geißendörfer, T. (2021). *Numerische Untersuchung des Strahlaufpralls auf eine Zahnflanke*. Bachelor's thesis. Supervisor: Prof. Hans-Jörg Bauer, Co-supervisor: Emre Ayan, M.Sc.

Glahn, A. (1995). „Zweiphasenströmung in Triebwerkslagerkammern - Charakterisierung der Ölfilmströmung und des Wärmeübergangs". PhD thesis. Karlsruhe: Universität Karlsruhe.

Handschuh, R. (1992). *Effect of lubricant jet location on spiral bevel gear operating temperatures*. NASA Technical Memorandum 105656. Cleveland, Ohio: Lewis Research Center.

Handschuh, R. (1995). *Thermal Behavior of Spiral Bevel Gears*. NASA Technical Memorandum 106518. Cleveland, Ohio: Lewis Research Center.

He, Z., Guo, G., Tao, X., Zhong, W., Leng, X., and Wang, Q. (2016). „Study of the effect of nozzle hole shape on internal flow and spray characteristics". In: *International Communications in Heat and Mass Transfer*, Band 71, pp. 1–8. ISSN: 07351933. DOI: 10.1016/j.icheatmasstransfer.2015.12.002.

He, Z., Shao, Z., Wang, Q., Zhong, W., and Tao, X. (2015). „Experimental study of cavitating flow inside vertical multi-hole nozzles with different length–diameter ratios using diesel and biodiesel". In: *Experimental Thermal and Fluid Science*, Band 60, pp. 252–262. ISSN: 08941777. DOI: 10.1016/j.expthermflusci.2014.09.015.

Hiroyasu, H., Arai, M., and Shimizu, M. (1991). „Break-up length of a liquid jet and internal flow in a nozzle“. In: *Proc. 5th. ICLASS*, pp. 275–282.

Hu, X., Chen, J., Wu, M., and Wang, J. (2021). „Thermal Analysis of Herringbone Gears Based on Thermal Elastohydrodynamic Lubrication Considering Surface Roughness“. In: *Energies*, Band 14, Heft 24, p. 8564. DOI: 10.3390/en14248564.

IATA (2021). *Resolution on the Industry's Commitment to Reach Net Zero Carbon Emissions by 2050*. Accessed on 02.03.2023. Boston. URL: https://www.iata.org/en/pressroom/pressroom-archive/2021-releases/2021-10-04-03/.

Keller, M. C. (2022). „Zur numerischen Simulation der Ölstrahl-Zahnrad-Interaktion in Flugtriebwerken: Eine Studie mit SPH und VOF“. PhD thesis. Karlsruher Institut für Technologie (KIT). ISBN: 978-3-8325-5582-5. DOI: 10.30819/5582.

Keller, M. C., Braun, S., Wieth, L., Chaussonnet, G., Dauch, T. F., Koch, R., Schwitzke, C., and Bauer, H. J. (2019). „Smoothed Particle Hydrodynamics Simulation of Oil-Jet Gear Interaction“. In: *Journal of Tribology*, Band 141, Heft 7, V02BT41A019. ISSN: 07424787. DOI: 10.1115/1.4043640.

Keller, M. C., Kromer, C., Cordes, L., Schwitzke, C., and Bauer, H. J. (2020). „CFD study of oil-jet gear interaction flow phenomena in spur gears“. In: *The Aeronautical Journal*, Band 124, Heft 1279, pp. 1301–1317. ISSN: 0001-9240. DOI: 10.1017/aer.2020.44.

Kromer, C., von Plehwe, F. C., Cordes, L., Schwitzke, C., and Bauer, H. J. (2020). „Analytical Model for the Heat Transfer in Impingement Cooled Spur Gears“. In: *Proceedings of the ASME Turbo Expo 2020: Turbomachinery Technical Conference and Exposition. Volume 1: Aircraft Engine; Fans and Blowers. Virtual, Online. September 21–25, 2020. V001T01A023. ASME.* DOI: 10.1115/GT2020-14760.

Leoni, P. (1991). „Hochleistungsgetriebe mit getrennter Schmierung und Kühlung“. PhD thesis. Stuttgart: Universität Stuttgart.

Li, W. and Tian, J. (2017). „Unsteady-state temperature field and sensitivity analysis of gear transmission“. In: *Tribology International*, Band 116, pp. 229–243. ISSN: 0301679X. DOI: 10.1016/j.triboint.2017.07.019.

Lienhard J. H. V; Lienhard, J. H. I. (1984). „Velocity Coefficients For Free Jets From Sharp-Edged Orifices“. In: *Journal of Fluids Engineering*, Band 106, Heft 1, pp. 13–17. ISSN: 00982202. DOI: 10.1115/1.3242391.

Long, H., Lord, A. A., Gethin, D. T., and Roylance, B. J. (2003). „Operating temperatures of oil-lubricated medium-speed gears: Numerical models and experimental results“. In: *Proceedings of the Institution of Mechanical Engineers, Part G: Journal of Aerospace Engineering*, Band 217, Heft 2, pp. 87–106. ISSN: 0954-4100. DOI: 10.1243/095441003765208745.

MATLAB (2021). *9.11.0.1769968 (R2021b)*. Natick, Massachusetts: The MathWorks Inc.

McCain, J. W. and Alsandor, E. (1966). „Analytical Aspects of Gear Lubrication on the Disengaging Side“. In: *A S L E Transactions*, Band 9, Heft 2, pp. 202–211. ISSN: 0569-8197. DOI: 10.1080/05698196608972136.

Nassef, A. (2022). *Development of a Wetting Model for the Cooling of High Performance Gearboxes in Aero Engines*. Master's thesis. Supervisor: Prof. Hans-Jörg Bauer, Co-supervisors: Emre Ayan, M.Sc., Christian Kromer, M.Sc.

Niemann, G. and Winter, H. (2003). *Maschinenelemente*. Berlin, Heidelberg: Springer Berlin Heidelberg. ISBN: 978-3-662-11874-0. DOI: 10.1007/978-3-662-11873-3.

Patir, N. and Cheng, H. S. (1979). „Prediction of the Bulk Temperature in Spur Gears Based on Finite Element Temperature Analysis“. In: *A S L E Transactions*, Band 22, Heft 1, pp. 25–36. ISSN: 0569-8197. DOI: 10.1080/05698197908982899.

Pratt & Whitney (2021). *PW1100G-JM Product Card*. Accessed on 02.03.2023. URL: https://pwgtf.com/-/media/project/pw/pw-internet/commercial-aircraft/gtf-engine/gtf-site/pdf/pw_gtf_pc_pw1100g-jm_2021_web.pdf?rev=cf141d9e2897422ab1f603c6369031ad&hash=EDBF8BFD338452AC47807041088F0C8D.

Radzevich, S. P. (2012). *Dudley's handbook of practical gear design and manufacture*. Second edition. Boca Raton et al.: CRC Press and EBSCO Industries. ISBN: 978-1-4398-6602-3.

Rolls Royce (2022). *UltraFan: The Ultimate TurboFan*. Accessed on 02.03.2023. URL: https://www.rolls-royce.com/~/media/Files/R/Rolls-Royce/documents/innovation/ultrafan-fact-sheet.pdf.

Schober, H. (1983). „Einspritzschmierung bei Zahnradgetrieben“. PhD thesis. Stuttgart: Universität Stuttgart.

Terauchi, Y., Nagamura, K., and Wu, C. (1989). „On Heat-Balance of Gear-Meshing Apparatus: Experimental and Analytical Heat Transfer Coefficient on Tooth Faces“. In: *JSME international journal. Ser. 3, Vibration, control engineering, engineering for industry*, Band 32, Heft 3, pp. 467–474. ISSN: 0914-8825. DOI: 10.1299/jsmec1988.32.467.

The Royal Society (2023). *Net zero aviation fuels: resource requirements and environmental impacts*. Accessed on 02.03.2023. URL: royalsociety.org/net-zero-aviation-fuels.

Townsend, D. P. (1985). *Lubrication and cooling for high speed gears*. NASA Technical Memorandum 19850026094. Cleveland, Ohio: Lewis Research Center.

Townsend, D. P. and Akin, L. S. (1978). „Study of lubricant jet flow phenomena in spur gears—out of mesh condition“. In: *Journal of Mechanical Design*, Band 100, Heft 1, pp. 61–68. ISSN: 0022-2305. DOI: 10.1115/1.3453894.

Townsend, D. P. and Akin, L. S. (1981). „Analytical and Experimental Spur Gear Tooth Temperature as Affected by Operating Variables“. In: *Journal of Mechanical Design*, Band 103, Heft 4, pp. 219–226. DOI: 10.1115/1.3254868.

Van Heijningen, G. J. J. and Blok, H. (1974). „Continuous as against intermittent fling-off cooling of gear teeth“. In: *Journal of Lubrication Technology*, Band 96, Heft 4, pp. 529–538. ISSN: 00222305. DOI: 10.1115/1.3452476.

Von Plehwe, F. C. (2022). „Untersuchung des Wärmeübergangs durch Einspritzkühlung für ein Höchstleistungsgetriebe“. PhD thesis. Karlsruher Institut für Technologie (KIT). ISBN: 978-3-8325-5436-1. DOI: 10.30819/5436.

Von Plehwe, F. C., Schwitzke, C., and Bauer, H. J. (2021). „Heat Transfer Coefficient Distribution on Oil Injection Cooled Gears: Experimental Method, Uncertainty, and Results“. In: *Journal of Tribology*, Band 143, Heft 9, p. 25. ISSN: 07424787. DOI: 10.1115/1.4049262.

Wang, Y., Tang, W., Chen, Y., Wang, T., Li, G., and Ball, A. D. (2017). „Investigation into the meshing friction heat generation and transient thermal characteristics of spiral bevel gears“. In: *Applied Thermal Engineering*, Band 119, Heft 11, pp. 245–253. ISSN: 13594311. DOI: 10.1016/j.applthermaleng.2017.03.071.

Yokota, M., Ito, Y., and Shinoke, T. (1988). „High speed photographic observations of cavitation arising in the high-speed oil-flow through a very small long orifice“. In: *9th International Symposium on Jet Cutting Technology, Sendai, Japan*, pp. 13–21.

Zhang, J., Liu, S., and Fang, T. (2017). „Determination of surface temperature rise with the coupled thermo-elasto-hydrodynamic analysis of spiral bevel gears“. In: *Applied Thermal Engineering*, Band 124, Heft 5, pp. 494–503. ISSN: 13594311. DOI: 10.1016/j.applthermaleng.2017.06.015.

Supervised Student Projects

Bolz, M. (2020). *Experimentelle Untersuchung des lokalen Wärmeübergangs bei der Einspritzkühlung von Zahnrädern*. Bachelor's thesis. Supervisor: Prof. Hans-Jörg Bauer, Co-supervisors: Emre Ayan, M.Sc., Christian Kromer, M.Sc.

Geißendörfer, T. (2021). *Numerische Untersuchung des Strahlaufpralls auf eine Zahnflanke*. Bachelor's thesis. Supervisor: Prof. Hans-Jörg Bauer, Co-supervisor: Emre Ayan, M.Sc.

Nassef, A. (2022). *Development of a Wetting Model for the Cooling of High Performance Gearboxes in Aero Engines*. Master's thesis. Supervisor: Prof. Hans-Jörg Bauer, Co-supervisors: Emre Ayan, M.Sc., Christian Kromer, M.Sc.

Previous Publications of the Author

Ayan, E., Kromer, C., Schwitzke, C., and Bauer, H. J. (2022a). „Experimental investigation of the oil jet heat transfer on meshing spur gears“. In: *25th Conference of the International Society of Air Breathing Engines (ISABE 2022), Ottawa, Canada, September 25-30*. DOI: 10.5445/IR/1000151853.

Ayan, E., Kromer, C., Schwitzke, C., and Bauer, H. J. (2024). „Heat transfer on impingement cooled meshing spur gears: Experimental comparison of into-mesh, out-of-mesh and inclined impingement methods“. In: *Heat and Mass Transfer*. ISSN: 1432-1181. DOI: 10.1007/s00231-024-03464-1.

Ayan, E., von Plehwe, F. C., Keller, M. C., Kromer, C., Schwitzke, C., and Bauer, H. J. (2021). „Experimental Determination of Heat Transfer Coefficient on Impingement Cooled Gear Flanks: Validation of the Evaluation Method“. In: vol. Volume 5B: Heat Transfer — General Interest; Internal Air Systems; Internal Cooling. Turbo Expo: Power for Land, Sea, and Air. DOI: 10.1115/GT2021-58838.

Ayan, E., von Plehwe, F. C., Keller, M. C., Kromer, C., Schwitzke, C., and Bauer, H. J. (2022b). „Experimental Determination of Heat Transfer Coefficient on Impingement Cooled Gear Flanks: Validation of the Evaluation Method“. In: *Journal of Turbomachinery*, Band 144, Heft 8, p. 229. ISSN: 0889-504X. DOI: 10.1115/1.4053694.

Kromer, C., Ayan, E., Schwitzke, C., and Bauer, H. J. (2022). „Experimental Investigation of the Oil Jet Heat Transfer for an Aero Engine Gearbox“. In: *25th Conference of the International Society of Air Breathing Engines (ISABE 2022), Ottawa, Canada, September 25-30*. DOI: 10.5445/IR/1000152758.